11-1994

Groundwater Flow and Elastoplastic Stress-Strain Model for Cohesive Soils with Application to Channel Bank Stability

Digital Object Identifier: https://doi.org/10.13023/kwrri.rr.191

Richard A. Rohlf
University of Kentucky

Billy J. Barfield
University of Kentucky

Gary K. Felton
University of Kentucky

Research Report No. 191

GROUNDWATER FLOW AND ELASTOPLASTIC STRESS-STRAIN MODEL FOR COHESIVE SOILS WITH APPLICATION TO CHANNEL BANK STABILITY

By

Richard A. Rohlf
Principal Investigator

Billy J. Barfield
Gary K. Felton

Agreement Number: DAAL03-87-D0074
Period of Project: March, 1991 to October, 1993

Water Resources Research Institute
University of Kentucky
Lexington, KY

The work upon which this report is based was supported in part by funds provided by the United States Army Corps of Engineers, Research Triangle, North Carolina.

November, 1994

DISCLAIMER

Contents of this report do not necessarily reflect the views and policies of the U.S. Department of the Interior, Washington, D.C., nor does mention of trade names or commercial products constitute their endorsement or recommendation for use by the U.S. Government.

ABSTRACT

A saturated-unsaturated groundwater flow and elastoplastic stress-strain finite element model was developed for simulating the mechanical behavior of rill and gully sized channel banks. The model coupled the two-dimensional saturated-unsaturated groundwater flow equation with a plane strain formulation of the virtual work equation. The constitutive relationship used the modified Cam clay yield function. The model included the effects of seepage force and variation in soil cohesive strength due to changes in water content and void ratio. A staggered solution procedure was used in which the groundwater equation was solved first to determine seepage force and soil cohesive force, and then the stress-strain equation was solved. Upon reaching the failure point, the elastoplastic constitutive relationship was replaced with a weak elastic relationship.

The model was verified by comparing predictions with (1) one-dimensional analytic solutions for unsaturated flow, saturated flow, and elastic strain; (2) other numerical solutions using the modified Cam clay yield function; (3) triaxial tests; and (4) laboratory experiments. The laboratory experiments employed a specially designed cyclic soil compactor and plexiglass flume to form and compact channel banks. The channel banks were subjected to a rising and falling hydrograph.

Model simulation included groundwater movement into the channel bank, strain in the x-direction, and the location of finite elements which reached ultimate strength. Failure surfaces were delineated by zones of high x-strain in conjunction with finite elements which reached ultimate strength. The model provided good insight into the failure mechanism for popout failure and a reasonable prediction of plane failure.

TABLE OF CONTENTS

LIST OF FIGURES

PAGE

LIST OF TABLES

PAGE

CHAPTER I

REVIEW OF CHANNEL BANK FAILURE MECHANISMS

INTRODUCTION

The removal of material from channel banks is controlled by the two interrelated processes of erosion and mechanical failure (Thorne, 1982). Erosion is characterized by the removal of individual soil particles along the channel wetted perimeter by hydraulic forces, while mechanical failure is characterized by the removal of individual particles and blocks of material by gravity.

Erosional processes can produce near vertical to overhanging channel banks which facilitates mechanical failure. Processes which increase body forces within the channel bank, such as an increase in soil density or an increase in seepage force, contribute to mechanical failure. Processes which affect soil strength, such as (1) an increase or decrease in moisture content, (2) root penetration and root density, and (3) freeze-thaw cycles, also contribute to mechanical failure.

The objective of this research was to define and mathematically model those processes which contribute to the mechanical failure of channel banks created by the formation of rills and gullies. Erosional processes, which primarily determine the geometry of channel banks, were not directly addressed under this project.

Those processes which affect the mechanical failure of channel banks including (1) groundwater movement into and out of the channel bank during passage of a hydrograph; (2) seepage forces; (3) soil strength including the effects of anisotropic consolidation and strain hardening; (4) the formation of tension cracks; (5) soil density; and (6) soil water content, were considered and, if possible and appropriate, were incorporated into a mathematical model. The mathematical model was verified with laboratory experiments in which pre-formed vertical channel banks approximately 20 cm high were subjected to a range of water level fluctuations.

The remaining portion of this chapter will discuss field and laboratory observations of channel bank failure and traditional methods of analyzing channel bank stability. Chapter II will present the model formulation for saturated and unsaturated groundwater flow and soil stress-strain, and will discuss the development of a soil cohesive pressure relationship; Chapter III will describe laboratory testing and model results; and Chapter IV contains a summary and conclusions.

MECHANISMS OF CHANNEL BANK FAILURE

Mechanisms of channel bank failure depend on (1) geometry of the channel bank; (2) groundwater conditions within the channel bank; (3) soil properties; and (4) hydraulic conditions in the channel. Failure mechanisms can initially be separated into those which are applicable to non-cohesive and cohesive soils.

Non-Cohesive Channel Banks

Failure of channel banks composed of non-cohesive material was investigated by Thorne (1982, 1978), and Thorne and Lewin (1979). Sections of closely packed and imbricated sandy gravel were spray-painted to monitor the movement of grains. Those portions of the bank which were not affected by channel flow retreated at a rate of 20-200 mm/year due to precipitation induced surface erosion and a reduction in effective strength resulting from increased pore pressure. Detached grains accumulated as a wedge of loosely packed gravel at the base of the bank. Failure by plane slip was observed to occur on the upper portions of the bank as a result of oversteepening due to the detachment and transport of material from the base of the bank during intermediate channel flow.

Cohesive Channel Banks

Three mechanisms of channel bank failure in cohesive material have been identified: (1) circular arc failure with both deep seated and shallow circles; (2) slab or plane failure; and (3) creation of overhanging banks through the removal of material at the toe of the bank by formation of a 'popout' or by excess shear forces, and failure of the remaining cantilever. (Bradford and Piest, 1980; Thorne, 1982; Little, Thorne, and Murphey, 1982).

Circular Arc Failure (Deep Seated)

Deep seated circular arc failures may intersect the ground surface at the slope, toe, or channel bottom (Fig. I-1). These failures have been observed on high cohesive banks and bluffs in the Mississippi River delta region. Seasonal scouring of pools at concave bends resulted in oversteepening of the bank and circular arc failure. In some cases, increased scour resulted from a reduction in upstream sediment supply due to the installation of revetments (Turnbull, Krinitizsky and Weaver, 1966).

Frydman and Beasley (1976) constructed a physical model of a channel bank on the River Ouse in the East Sussex region of England. The physical model was used to study a circular arc

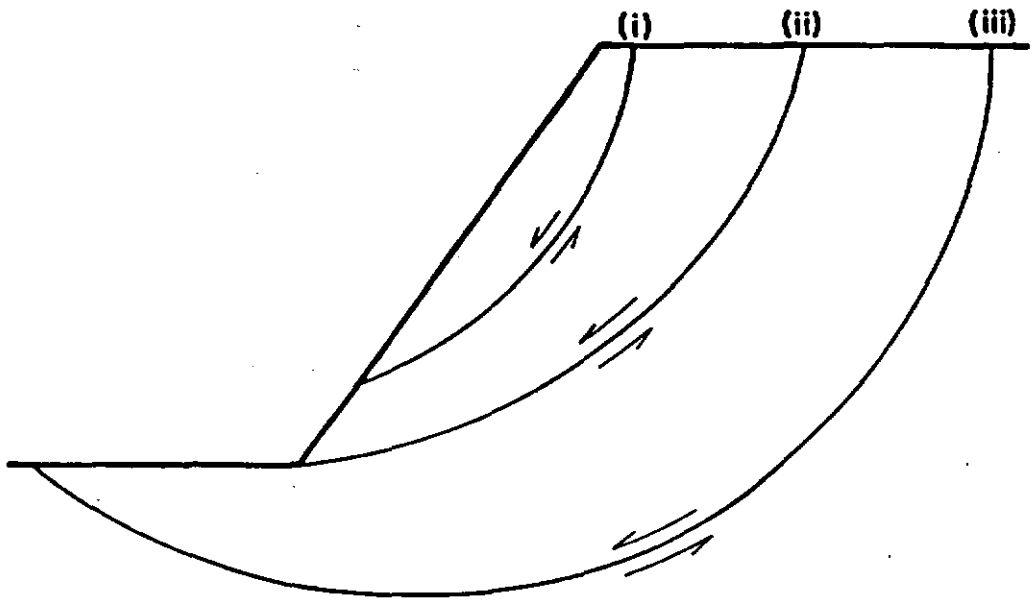

Figure I-1. Rotational slip in a cohesive bank, (i) slope failure, (ii) toe failure, (iii) base failure (Thorne, 1982).

failure that occurred in 1969 as a result of a channel deepening project to increase flood flow capacity of the river. To achieve dimensional similarity between the model and prototype, it was necessary to scale accelerations inversely with linear dimensions. The resulting model had a height of 15 cm and was loaded in a centrifuge at an acceleration of 46.5 g. A cross-section of the model showing the initial channel geometry after dredging is illustrated in Fig. I-2. The model was constructed with both kaolin (shear strength of 10-20 kPa) and natural bank materials. Water

levels in the model were raised and lowered to simulate flooding. Markers were placed in a triangular grid to enable measurement of displacement and strain.

Results of the model operation using kaolin are illustrated in Figs. I-3 and I-4, for the dredged and undredged condition, respectively. Fig. I-3 shows the strain pattern of the dredged model immediately after drawdown. Just prior to failure, the 20% strain contour behind and below the wall joined and extended to the surface, indicating formation of a slip plane. The undredged model developed very small strains and showed no sign of failure (Fig. I-4).

Operation of the model using natural bank material gave results similar to the kaolin model. Fig. I-5 illustrates strain levels in relation to the slip surface.

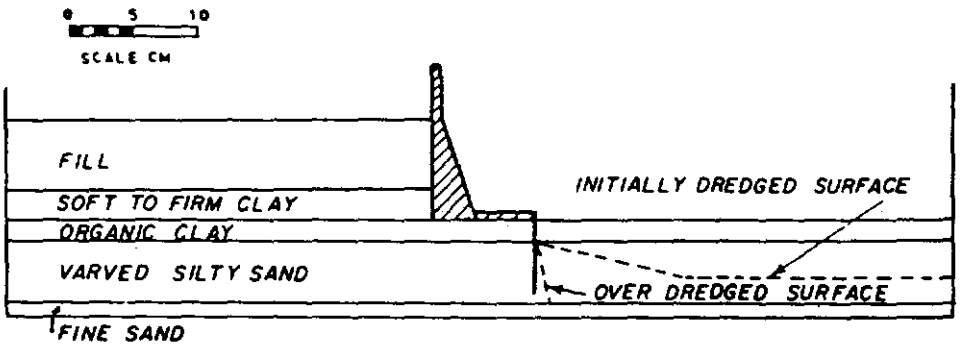

Figure I-2. Cross-section of model (Frydman and Beasley, 1976).

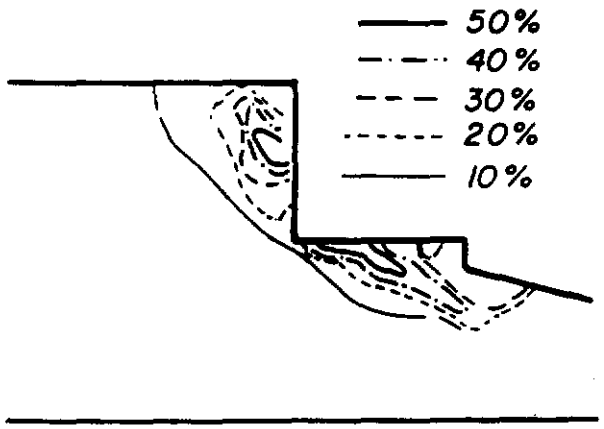

Figure I-3. Shear strain after drawdown in kaolin dredged model (Frydman and Beasley, 1976).

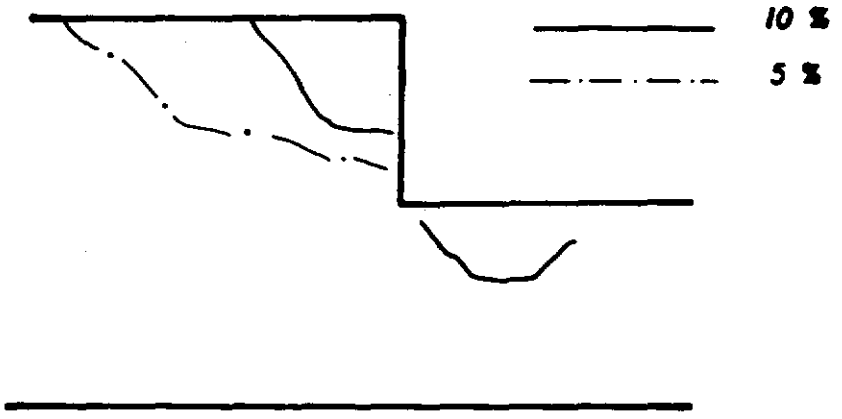

Figure I-4. Shear strain after drawdown in kaolin undredged model (Frydman and Beasley, 1976).

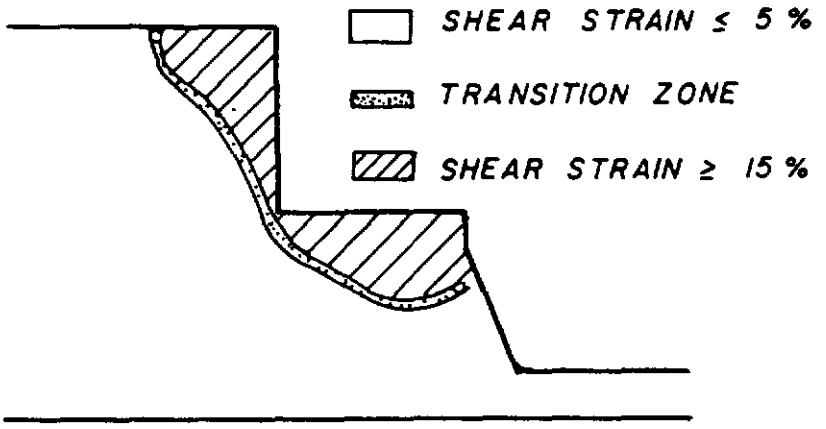

Figure I-5. Shear strain after drawdown in natural material overdredged model (Frydman and Beasley, 1976).

Circular Arc Failure (Shallow Circle)

Shallow slips have been widely observed in weakly cohesive banks and stiff fissured soils. These are usually attributed to the expansion of cracks and weathering processes. Shallow circular arc failures are similar to slab failures and the two processes are not easily distinguished in the field (Thorne, 1982).

Slab (Plane) Failure and Cantilever Failure

Plane failure, in which blocks or columns of soil slide or topple forwards into the channel, occur primarily in low cohesive banks. Little, Thorne, and Murphy (1982) reported slab failure as a primary failure mechanism on stream banks on the Yazoo Basin in northwestern Mississippi. Stream banks ranged from 3 to 10 m high with slope angles from 50° to 90° with the horizontal. In this type of failure, a tension crack developed vertically downward from the ground surface. Failure occurred along a slip surface which intersected the bottom of the tension crack and the toe of the channel slope (Little, Thorne, and Murphy, 1982; Lohnes and Handy, 1968; Thorne, Little, and Murphy, 1981).

Bradford and Piest (1977, 1980) identified a 'popout' or alcove failure near the toe of a vertical wall as a precursor to slab or plane failure of gully banks formed in loess derived alluvium. After formation of a popout, plane failure of the channel bank occurred in two successive stages as illustrated in Fig. I-6. Application of conventional limit equilibrium slope stability methods can not adequately predict the incremental failure shown in Fig. I-6.

Explanations for the formation of a popout included (1) collapse of the soil structure due to wetting; (2) migration of soil particles from areas adjacent to the wall due to groundwater flow out of the gully wall; (3) a reduction in soil tensile strength due to stress relief at the base of the gully wall; and (4) a reduction in soil cohesion due to increased water content. Slope stability analysis indicated that seepage forces were not directly responsible for failure of the gully wall.

Piest, Bradford, and Wyatt (1975) investigated erosion and sediment transport from gullies formed in loess in western Iowa. They observed that failure of a vertical bank began by chipping and flaking of soil from near the toe, until considerable undercutting occurred. Many of the flakes and chips were of appreciable size and appeared to have been dislodged by seepage flowing through macropores. After sufficient undercutting, the cantilever portion of the bank failed.

ANALYSIS OF CHANNEL BANK STABILITY

Procedures which have been applied to the analysis of channel bank stability can also be separated into those which are applicable to non-cohesive and cohesive soils. The analysis of channel bank stability has been summarized by Thorne (1982).

Non-Cohesive Channel Banks

The shear strength of non-cohesive material can be described by the Mohr-Coulomb equation with zero cohesion

$$s = (\sigma - u)\mathrm{Tan}\phi' \qquad \text{(I-1)}$$

where s is shear, σ is normal stress, u is pore pressure, and ϕ' is the effective or drained friction angle. Under drained conditions, u = 0 and stability is a function of the bank angle and angle of internal friction (Taylor, 1948)

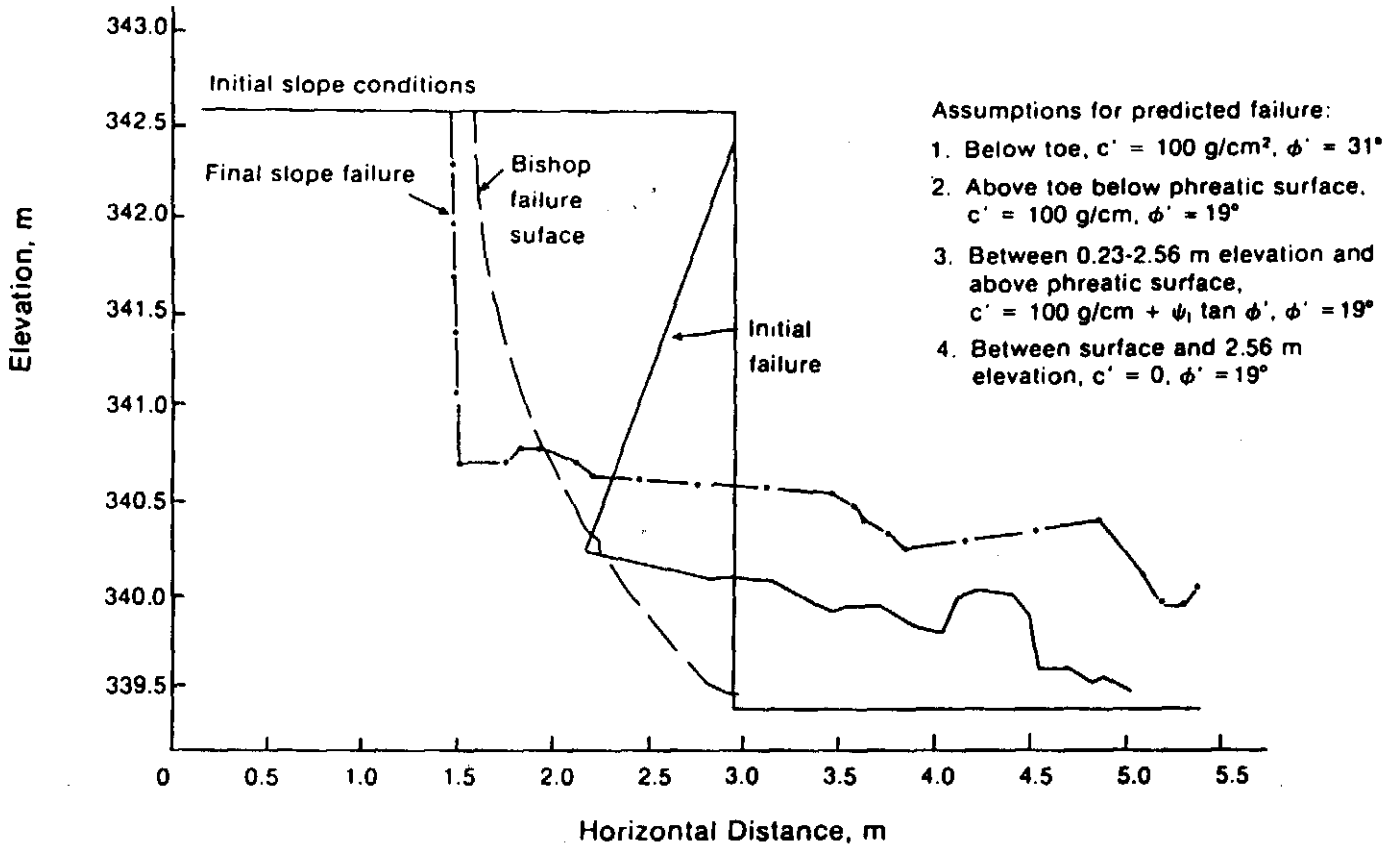

Figure I-6. Observed failure surface sequence and simplified Bishop predicted failure surface (Bradford and Piest, 1977).

$$F_s = \frac{\text{Tan}\theta}{\text{Tan}\phi} \qquad \text{(I-2)}$$

where F_s is the factor of safety and θ is the bank angle with the horizontal. For the limiting case in which $F_s = 1$, $\theta = \phi$.

Failure in non-cohesive material generally occurs as a shallow slip along a plane or slightly curved surface. Deep seated failures are unlikely in non-Cohesive material because shear strength usually increases more rapidly with depth than does shear stress (Taylor, 1948).

For undrained conditions, pore pressure can be significant and the limiting slope is given by (Carson and Kirkby, 1972)

$$\text{Tan}\ \alpha = \frac{(\gamma z_p \text{Cos}^2\theta - u)\ \text{Tan}\ \phi'}{\gamma\ z_p\ \text{Cos}^2\theta} \qquad \text{(I-3)}$$

where α is the limiting slope angle, γ is the unit weight of soil, and z_p is the vertical depth to the failure plane. If pore pressure is positive, the limiting slope angle is smaller than the friction angle. If the bank material is unsaturated, pore pressure can be negative. Negative pore pressure gives non-cohesive material an apparent cohesion and allows the bank angle to exceed the friction angle. Determination of pore pressure for saturated and unsaturated conditions requires a saturated-unsaturated ground-water flow model.

Cohesive Channel Banks

The shear strength of cohesive material is described by Eq. (I-1) with cohesion included

$$s = c' + (\sigma - u)\text{Tan}\phi' \qquad \text{(I-4)}$$

where c' is effective cohesion. The stability of channel banks can be determined by the method of limiting equilibrium in which soil is assumed to behave as a rigid plastic material (no strain occurs until failure is reached), and a factor of safety is calculated by the ratio of restraining forces to driving forces along a predetermined slip surface. Limiting equilibrium procedures are separated on the basis of the shape of the slip surface: (1) circular arc (log spiral), or (2) plane.

Circular arc slip surface

The method of limiting equilibrium can be applied to circular arc slip surfaces by dividing the material above the slip surface into a number of slices and analyzing the moments about the point of rotation for each slice (Fig. I-7). To obtain a determinant solution, it is necessary to make an assumption regarding the interslice forces. One common assumption, which is the basis of the simplified Bishop method, is that the forces on the sides of each slice are horizontal ($x_1 = x_2 = 0$ in Fig. I-7). The factor of safety for the simplified Bishop method is given by (Bishop, 1955)

$$F_s = \sum_{B}^{A} \left(\frac{[c'b + (w - ub)\tan\phi']\mathrm{Sec}\theta_F}{[1 + (\tan\theta_F \tan\phi')]} \, w \, \mathrm{Sin}\theta_F \right) \qquad \text{(I-5)}$$

where b is width of the slice, w is weight of the slice, and θ_F is the angle of the base of the slice with the horizontal. Since F_s appears on both sides of Eq. (I-5), an iterative solution is required to determine F_s. Also, there is no simple method for determining the critical slip surface for general cases, and a number of trial surfaces must be analyzed to determine the surface with the lowest factor of safety.

To facilitate application of Eq. (I-5) for simplified cases, stability charts have been developed. Morgenstern (1963) developed solutions for undrained channel banks (banks subjected to rapid drawdown so that undrained conditions can be assumed). Ponce (1978) developed solutions for drained conditions by assuming homogeneous soil conditions and that the critical circle passes through the toe and top of the bank.

A Simplified Bishop stability analysis of the previously discussed Ouse River channel bank was conducted using the slip surface and soil properties given in Fig. I-8. The calculated factor of safety varied from 1.2 to 1.4 depending on the amount of passive pressure attributed to the sheet pile, thus indicating that the bank should not have failed. Differences between the model behavior and the simplified Bishop stability analysis were explained by the phenomenon of progressive failure. Progressive failure has been discussed by several investigators including Skempton (1964), Bishop (1967), and Schofield and Wroth (1968). The problem has also been addressed through the numerical simulation of shear band formation in soils during triaxial testing (Shuttle and Smith, 1988).

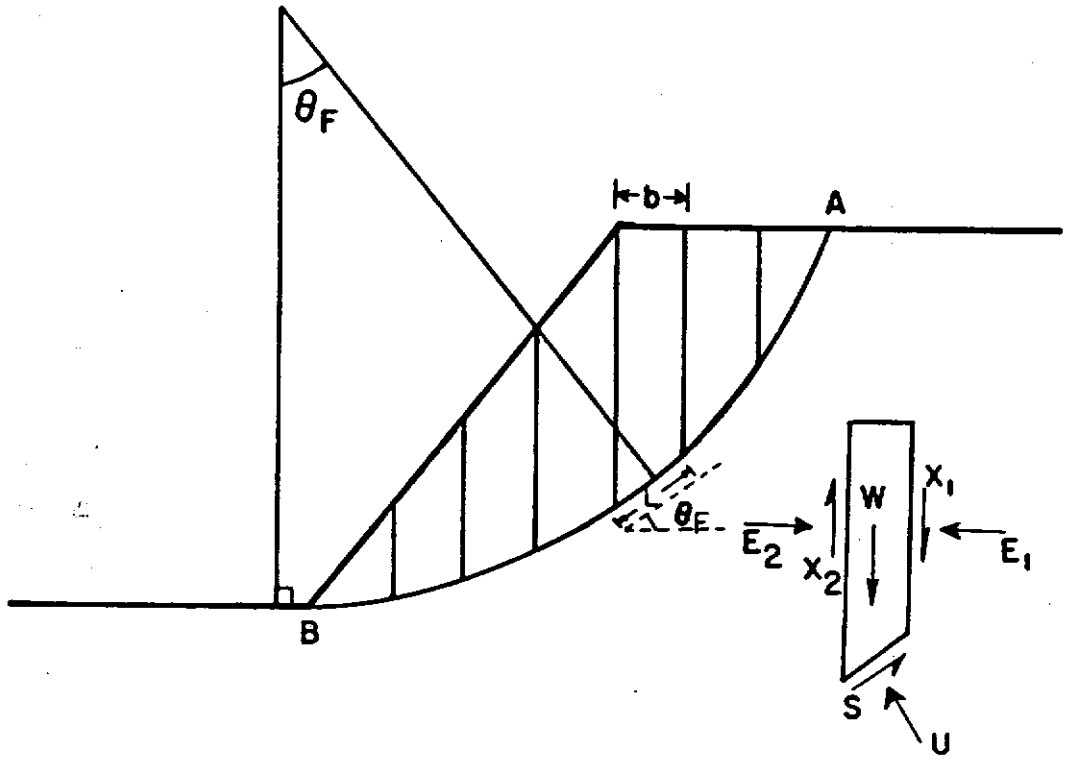

Figure I-7. Stability analysis of a circular slip surface by the method of slices (Thorne, 1982).

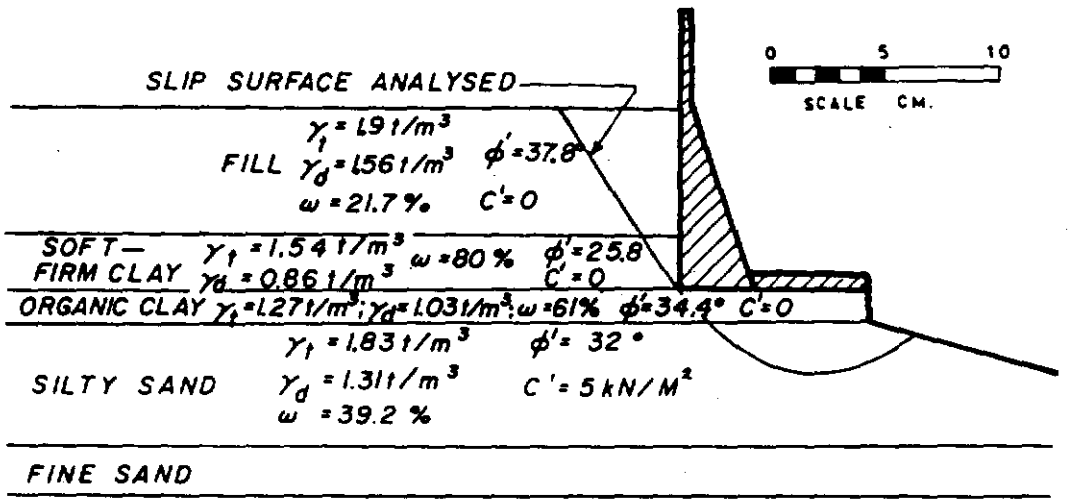

Figure I-8. Slip surface analyzed by simplified Bishop method (Frydman and Beasley, 1976).

As clay is strained, shear strength initially increases to a maximum value and then decreases asymptotically to a residual value. At the residual value, the cohesion is near zero and the Mohr-Coulomb friction angle can decrease from 1° to 10°. During shearing, overconsolidated clays tend to expand rapidly after the maximum strength is reached. Thus, part of the observed decrease in strength is due to an increase in void ratio and water content. In addition, during straining clay particles become partially oriented in the direction of shear, forming thin bands. These bands of clay particles become almost totally oriented at large strains (Skempton, 1964).

If an element of clay in a soil mass is subjected to stress beyond the peak strength, the resistance to strain will decrease at that point. This decrease in strength will require that the stress at a nearby point increase, again resulting in stress beyond the peak strength. In this manner, a progressive failure can develop in which the strength along the entire slip surface will be reduced to the residual value (Skempton, 1964).

Reanalysis of the Ouse channel bank failure using a cohesion of zero and a decreased friction angle (32° to 30° for the silty sand) produced a factor of safety of 0.9 (Frydman and Beasley, 1976).

Bradford, Farrell, and Larson (1973) performed a Simplified Bishop stability analysis for a typical gully wall formed in loessial soils of the midwest (Fig. I-9). Initial assumptions made in the analysis included (1) a water table exists at the toe of the slope; (2) the apparent soil cohesion at a given height above the water table can be determined from $c = \psi_i \text{ Tan } \phi'$, where ψ_i is soil water suction which is a linear function of height above the water table ($\psi_i = 0$ at the base of the cut and $\psi_i = \psi_H$ at the top of the cut of height H); (3) $c = 0$ at the base of the bank; (4) the circular failure surface does not cut below the toe of the wall; and (5) the failure surface is normal to the soil surface at the top of the vertical bank.

Results of the analysis for selected bank heights and soil densities are given in Table I-1. The values in Table I-1 indicate that the factor of safety is essentially independent of bank height, decreases with an increase in soil density, and is less than 1.0 for $\phi' \leq 35°$.

A second analysis was done to determine the effect of raising or lowering the water table on the factor of safety. In this case, the soil bulk density was assumed to increase linearly with depth from 1.65 at the surface to 1.95 at the base of the bank, and the friction angle was constant at 25°. Results of this analysis, which are presented in Table I-2, show that if the water table

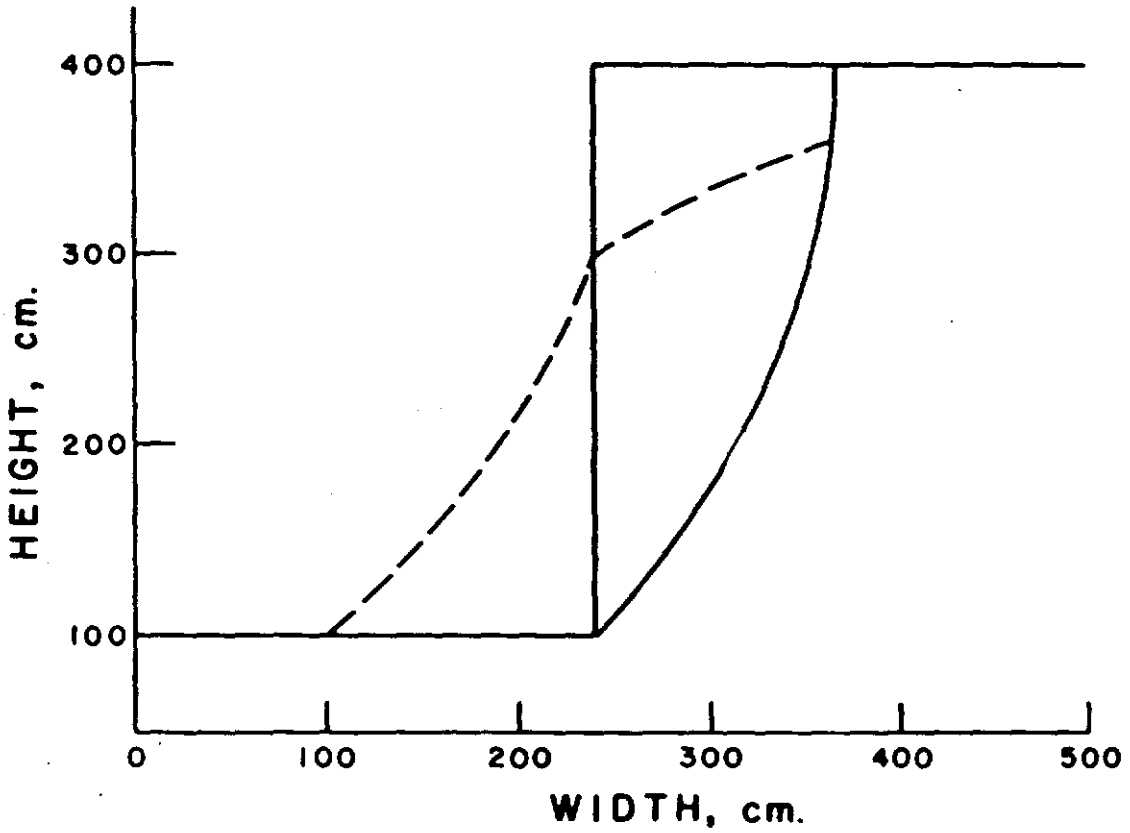

Figure I-9. Failure surface for gully wall (Bradford, Farrell and Larson, 1973).

reaches 110 cm below the surface (ψ_H = 410 for a 300 cm bank height), the bank will fail. Since the water level for gullies in loessial areas is generally above the toe of the wall, it was concluded that the assumption of zero cohesion at the elevation of the water table was not valid. Thus, in analyzing the effects of a fluctuating water table on bank stability, measurement of soil cohesion at zero suction is essential (Bradford, Farrell, and Larson, 1973).

Plane slip failure

A plane slip surface or Culman failure surface has the form illustrated in Fig. I-10. Equating forces along the failure plane provides an expression for the critical height of the bank.

$$H_c = \frac{4c \, Sin\theta \, Cos\phi}{\gamma[1 - Cos\,(\theta - \phi)]} \qquad (I\text{-}6)$$

where H_c is the critical bank height. Eq. (I-6) is expressed in terms of total stress and does not consider pore pressure. For a vertical bank, Eq. (I-6) simplifies to

$$H_\sigma = \frac{4c}{\gamma} Tan\left(45 + \frac{\phi}{2}\right) \qquad (I\text{-}7)$$

where H_σ is the critical height of a vertical bank.

Eq. (I-7) was modified by Terzaghi (1943) to include the effects of tension cracks. Horizontal tensile stress occurs in a soil mass when a vertical cut alters the stress distribution created by consolidation during the soil formation process (K_o consolidation) (Fig. I-11). The depth of the tension zone can be calculated using a Mohr circle as (Taylor, 1948)

$$z_o = \frac{2c}{\gamma} Tan\left(45 + \frac{\phi}{2}\right) \qquad (I\text{-}8)$$

where z_o is the depth of tensile stress.

In high banks, z_o is relatively small and a tension crack does not significantly affect the geometry of the failure surface. Therefore, the effect of tension cracks can be taken into account by reducing the length of the failure surface by the portion which lies within the tensile zone.

Table I-1
Effective stress analysis of vertical slopes for various soil parameters (Bradford, Farrell and Larson, 1973)

Slope height cm	Wet density gm/cm^3	Angle of friction degrees	Calculated factor of safety
20	1.70	25	0.58
		30	0.79
		35	0.95
		40	1.14
300	1.70	25	0.62
		30	0.76
		35	0.96
		40	1.11
300	1.80	25	0.59
		30	0.74
		35	0.89
		40	1.07
300	1.90	25	0.57
		30	0.71
		35	0.86
		40	1.03

Table I-2
Computed factors of safety as affected by change in water table for a slope height of 300 cm (Bradford, Farrell and Larson, 1973)

Wet density gm/cm^3		Angle of friction degrees	Suction at soil surface cm water	Calculated factor of safety
surface	toe			
1.65	1.95	25	300	0.60
1.65	1.95	25	330	0.72
1.65	1.95	25	360	0.83
1.65	1.95	25	410	1.00
1.65	1.95	25	450	1.

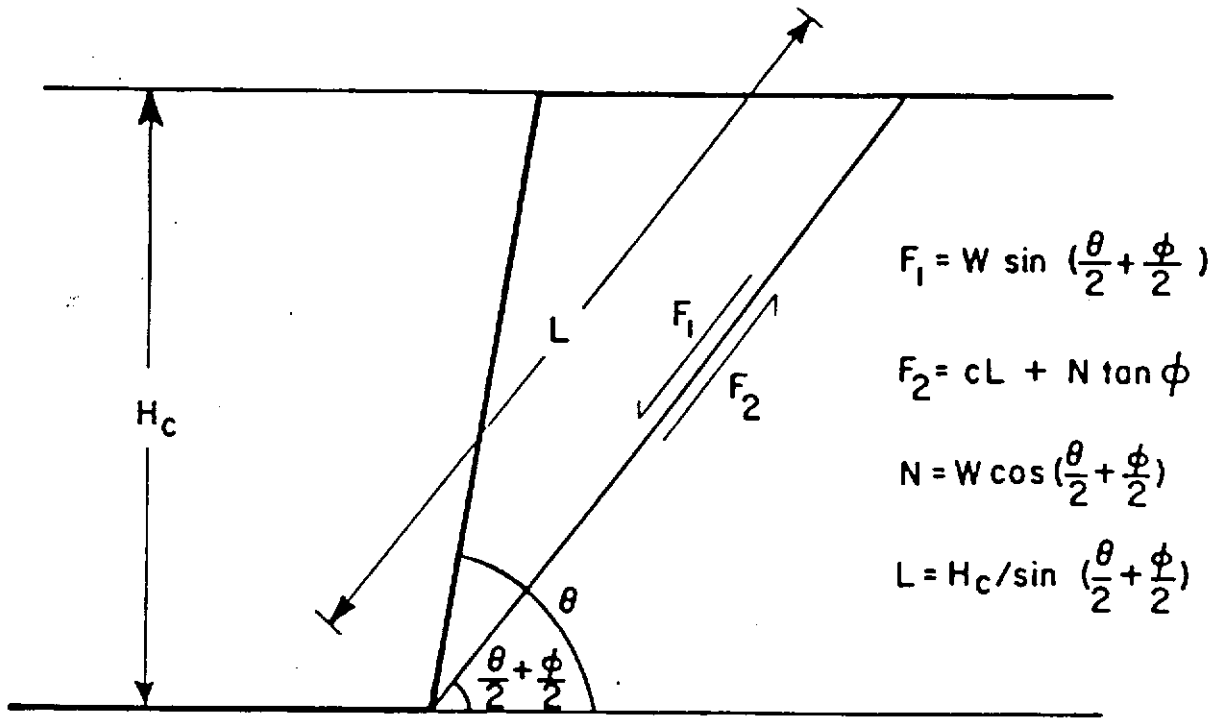

Figure I-10. Schematic for plane slip failure (Thorne, 1982).

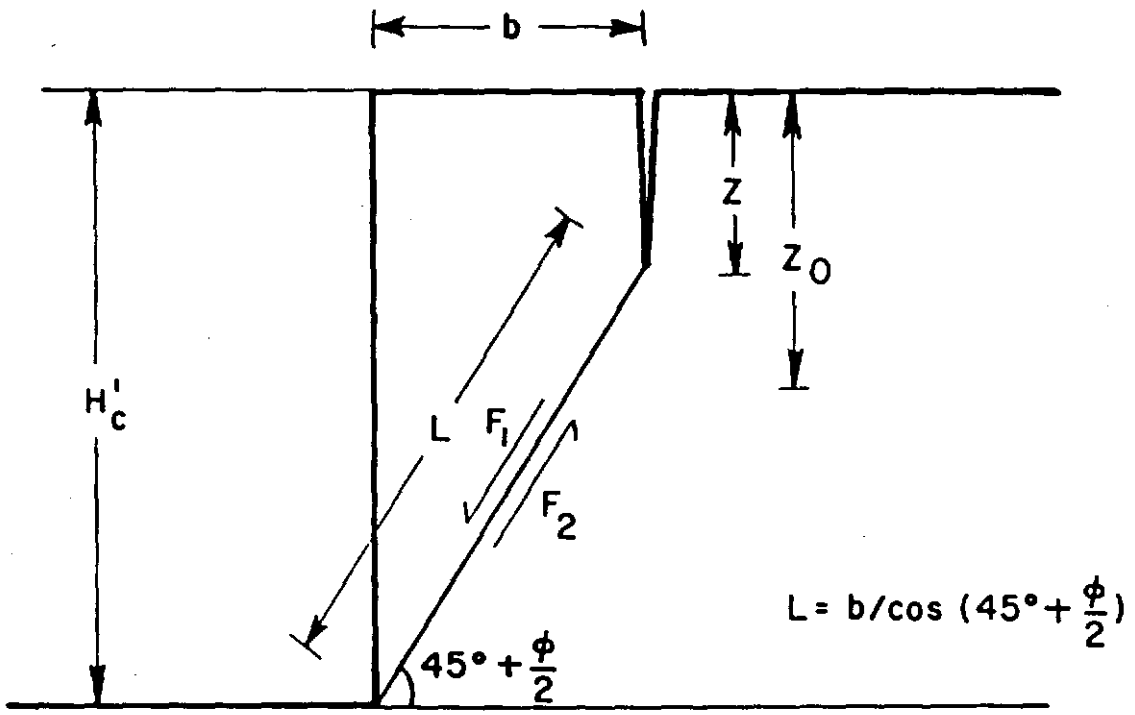

Figure I-11. Schematic for plane slip failure with a tension crack (Thorne, 1982).

For low vertical banks, where a tension crack may form a significant portion of the failure surface, Eqs. (I-7) and (I-8) can be combined by assuming that tension cracks develop to the depth of tensile stress ($z = z_0$, Fig I-11) to give the critical height for a vertical bank with a tension crack.

$$H'_{cr} = H_{cr} - z_o = \frac{2c}{\gamma} \text{Tan}\left(45 + \frac{\phi}{2}\right) \tag{I-9}$$

where H'_{cr} is the critical height for a vertical bank with a tension crack. If it is assumed that tensile stress is a maximum at the surface and decreases linearly with depth to zero at z_0, the depth of tension cracking for a soil with a tensile strength of σ_{TC} is given by (Lohnes and Handy, 1968)

$$y = z_o \left(1 - \frac{\sigma_{TC}}{\sigma_T}\right) \tag{I-10}$$

where y is the depth of the tension crack, σ_{TC} is tensile strength of the soil, and σ_T is tensile stress at the surface. The tensile stress at the surface is given by

$$\sigma_T = 2c \text{ Tan}\left(45 - \frac{\phi}{2}\right) \tag{I-11}$$

which allows the width of the failure slab to be determined from geometry (Fig. I-11).

$$b = \frac{(H'_{cr} - y)}{\text{Tan}\left(45 + \frac{\phi}{2}\right)} \tag{I-12}$$

where b is width of the failure slab.

Cantilever failure

Thorne (1982) and Thorne and Tovey (1981) applied beam theory to analyze an overhang or cantilever which is created by the formation of popouts or through the erosion of underlying bank material (Fig. I-12). A cantilever remains in place until a state of limiting equilibrium is reached due to increased width resulting from continued undercutting, or weakening by wetting or tension cracking. Depending on the geometry, a cantilever can fail by shear, beam, or tensile failure. Dimensionless stability charts were constructed to estimate the factor of safety and mechanics of failure (Fig. I-13).

SUMMARY

The mechanical failure of channel banks is characterized by the removal of individual particles and blocks of material by gravity. The objective of this research was to define and mathematically model those processes which contribute to the mechanical failure of channel banks created by the formation of rills and gullies.

Mechanisms of channel bank failure in cohesive material include (1) circular arc failure with both deep seated and shallow circles; (2) slab or plane failure; and (3) creation of overhanging banks and failure of the remaining cantilever.

The analysis of channel bank failure for cohesive material has primarily been confined to limit equilibrium methods such as the simplified Bishop method of slices for circular arc failure, the Culman method of equating forces along the failure plane for plane failure, and the application of beam theory to analyze overhanging channel banks.

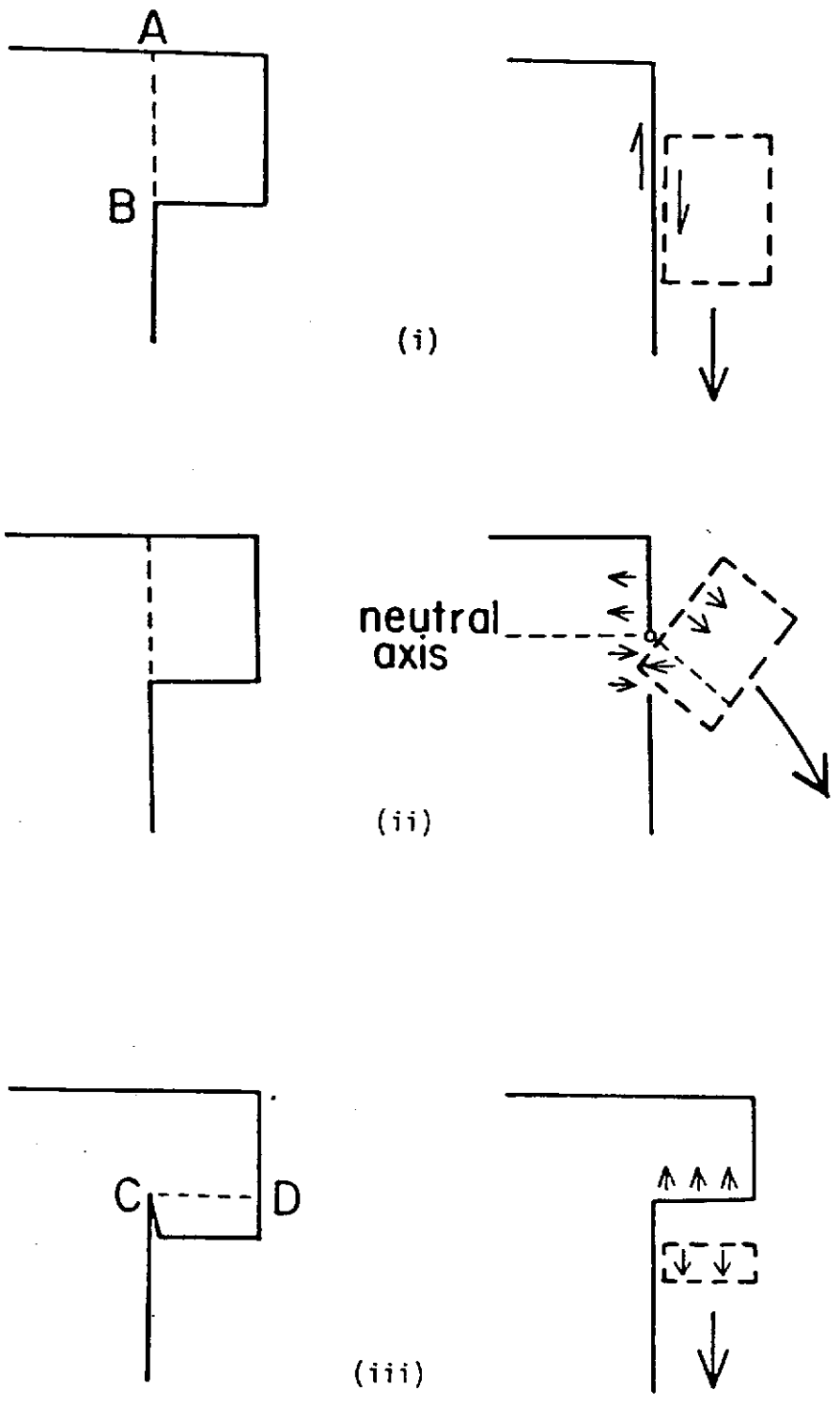

Figure I-12. Mechanics of failure (i) shear failure, (ii) beam failure, (iii) tensile failure (Thorne, 1982).

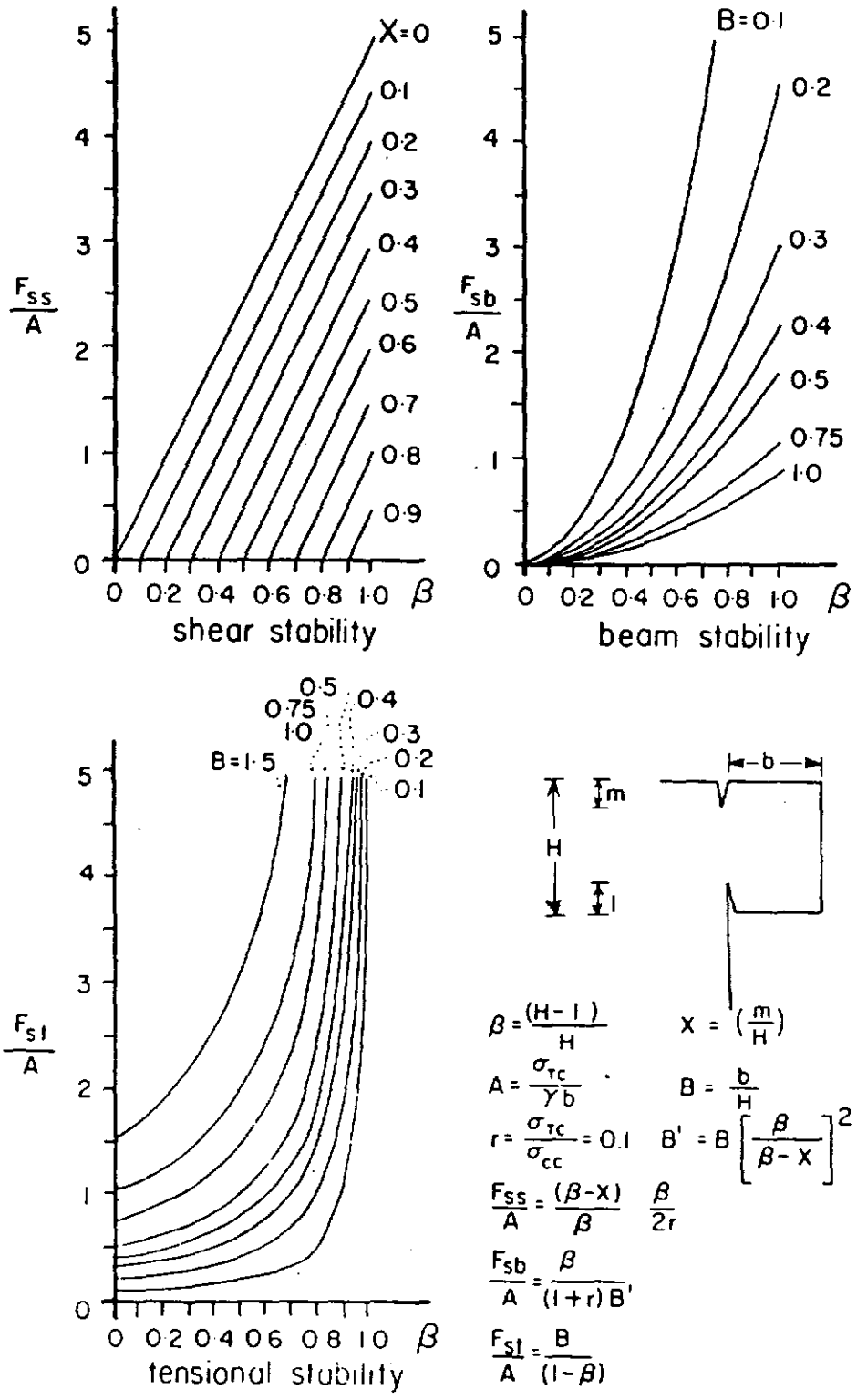

Figure I-13. Dimensionless charts and equations for cantilever stability (Thorne, 1982).

CHAPTER II

FINITE ELEMENT FORMULATION

INTRODUCTION

To meet the objectives of addressing (1) changes in soil strength due to variation in soil water content, (2) seepage force resulting from groundwater movement into and out of a channel bank, and (3) variation in effective stress and soil unit weight caused by saturated and unsaturated conditions, a combined saturated-unsaturated groundwater flow and soil stress-strain model was developed.

The basic equations describing the dynamic interaction of soil-fluid systems were developed by Biot (Zienkiewicz and Shiomi, 1984). Under the assumptions of saturated flow, linear elastic stress-strain behavior, and a periodic loading function, Zienkiewicz, Chang, and Bettess (1980) solved the Biot equations in terms of dimensionless parameters. The dimensionless parameters can be used to estimate if the full Biot equations must be used or if the fluid phase or fluid and solid phase accelerations can be neglected in a dynamic soil-groundwater problem.

Application of this procedure to a gully sized channel bank (30 cm bank height) subjected to a rising and falling hydrograph with a period of five minutes shows that this problem falls into the quasi-static or consolidation category in which the fluid and solid phase accelerations can be neglected.

Given the quasi-static nature of the problem, a staggered solution process using the finite element method was adopted (Zienkiewicz and Taylor, 1991). Under this procedure the saturated-unsaturated groundwater flow and soil stress-strain equations were formulated and solved separately.

SATURATED-UNSATURATED GROUNDWATER FLOW MODELING

Governing Equation and Finite Element Formulation

For incompressible saturated fluid flow through a vertically deforming porous medium the governing equation is given by

$$\nabla\cdot(K_s\nabla h) - Q = C_s\frac{\partial h}{\partial t} \quad \text{on } \Omega_1 \tag{II-1}$$

subject to

$$h(t) = \bar{h}(t) \quad \text{on } \Gamma_h \tag{II-2}$$

$$K_{sn}\frac{\partial h}{\partial n} = \bar{f}(t) \quad \text{on } \Gamma_f \tag{II-3}$$

$$h(0) = \bar{h} \quad \text{on } \Omega_t \tag{II-4}$$

where h is hydraulic head ($h = p/\gamma_f + z = \psi + z$, where p is water pressure, ψ is pressure head, z is elevation head, and γ_f is fluid unit weight); K_s is saturated hydraulic conductivity; Q is a point source or withdrawal; C_s is a saturated storage coefficient; Ω_t is the saturated domain; $\bar{h}(t)$ is prescribed head as a function of time; $\bar{f}(t)$ is prescribed infiltration or exfiltration as a function of time; K_{sn} is saturated hydraulic conductivity normal to the boundary; Γ_h and Γ_f are the prescribed head and prescribed flux boundaries, respectively; and n is the direction normal to Γ. Equation (II-1) is also applied to the unsaturated zone by replacing K_s and C_s with $K(\psi)$ and $C(\psi)$, respectively, where $K(\psi)$ and $C(\psi)$ are functions of the water pressure head, ψ (Desai and Li, 1983; Bear, 1972).

Application of the Galerkin finite element method to a two-dimensional formulation of Eq. (II-1) and assembling the element equations yields

$$[C(\psi)]\{\dot{h}\} + [K(\psi)]\{h\} = \{q\} \tag{II-5}$$

where $[C(\psi)]$ is the capacitance or storage matrix, $[K(\psi)]$ is the stiffness or conductivity matrix, $\{h\}$ is a vector of unknown heads, $\{\dot{h}\}$ is a vector of unknown head temporal derivatives, and $\{q\}$ is a vector containing infiltration, exfiltration, source, and withdrawal.

Application of a finite difference scheme to Eq. (II-5) gives

$$\begin{aligned}([C(\psi)] + \theta[K(\psi)]\Delta t)\{h_{i+1}\} = ([C(\psi)] - (1-\theta)[K(\psi)]\Delta t)\{h_i\} + \\ ((1-\theta)\{q_i\} + \theta\{q_{i+1}\})\Delta t\end{aligned} \tag{II-6}$$

where Δt is the time increment, θ is a weighting factor, and i and i+1 indicate the current and advanced time step, respectively. In this application, the Galerkin weighting factor of $\theta = 2/3$ was used. This is more accurate than the backward difference scheme ($\theta = 1$) and more stable than the central difference scheme ($\theta = 1/2$) (Stasa, 1985). Also, a lumped capacitance matrix was used to minimize oscillation of the solution.

Separating the hydraulic conductivity and storage terms into a constant or saturated term and a residual pressure dependent term yields

$$K(\psi) = K_s - r(\psi) \tag{II-7}$$

$$C(\psi) = C_s + s(\psi) \tag{II-8}$$

where $K(\psi)$ and $C(\psi)$ are the pressure dependent hydraulic conductivity and storage coefficient, respectively; K_s is the saturated hydraulic conductivity; C_s is the saturated storage coefficient; and $r(\psi)$ and $s(\psi)$ are functions of the pressure head (Desai and Li, 1983).

Substituting Eqs. (II-7) and (II-8) into Eq. (II-6) yields

$$\begin{aligned}([C_s] + \theta[K_s]\Delta t)\{h_{i+1}^{j+1}\} = {} & [r(\psi)_i^j]\Delta t(\theta\{h_{i+1}^{j+1}\} + (1 - \theta)\{h_i^j\}) \\ & + ([C_s] - (1 - \theta)[K_s]\Delta t)\{h_i\} \\ & + [s(\psi)_i^j](\{h_i^j\} - \{h_{i+1}^{j+1}\}) \\ & + ((1 - \theta)\{q_i\} + \theta\{q_{i+1}\})\Delta t\end{aligned} \tag{II-9}$$

where j and j+1 indicate the current and advanced unsaturated iteration, respectively.

The solution of Eq. II-9 requires that h_i^j be substituted for terms involving h_{i+1}^{j+1} on the right hand side (RHS). Since the left hand side (LHS) contains only constant terms ($[K_s]$ and $[C_s]$), this substitution allows Eq. II-9 to be solved by factoring the LHS once and then using back substitution to solve for a varying RHS. However in this application, this solution procedure proved

unstable due to high water content gradients and it was necessary to set $C_s = C(\psi)$ and $s(\psi) = 0$, and to factor the LHS at each time step and unsaturated iteration.

Iterative solution of Eq. II-9 was continued until differences in successive head values reached an acceptable tolerance. The number of iterations required was heavily dependent on the time step used.

For a two-dimensional formulation, the individual element terms in Eq. II-9 are given by

$$[K_S^e] = \int_{A^e} K_{sx}\left[\frac{\partial N}{\partial x}\right]^T\left[\frac{\partial N}{\partial x}\right]dxdz + \int_{A^e} K_{sz}\left[\frac{\partial N}{\partial z}\right]^T\left[\frac{\partial N}{\partial z}\right]dxdz \qquad \text{(II-10)}$$

$$[C_S^e] = \int_{A_e} C_s[N]^T[N]dxdz \qquad \text{(II-11)}$$

$$\{q\} = \{q_Q^e\} - \{q_f^e\} \qquad \text{(II-12)}$$

$$\{q_Q^e\} = \int_{A^e}[N]^T Q dxdz \qquad \text{(II-13)}$$

$$\{q_f^e\} = \int_C [N]^T\{f\}dC \qquad \text{(II-14)}$$

$$[r(\psi)^e] = \int_{A_e} r(\psi)_x\left[\frac{\partial N}{\partial x}\right]^T\left[\frac{\partial N}{\partial x}\right]dxdz + \int_{A_e} r(\psi)_z\left[\frac{\partial N}{\partial z}\right]^T\left[\frac{\partial N}{\partial z}\right]dxdz \qquad \text{(II-15)}$$

$$[s(\psi)^e] = \int_{A_e} s(\psi)[N]^T[N]dxdz \qquad \text{(II-16)}$$

where $r(\psi)_x$ and $r(\psi)_z$ represent unsaturated residual hydraulic conductivity in the x and z directions, respectively, and the superscript e denotes element values prior to assembly. The required integration of the element terms in Eqs. II-10 through II-16 was performed using Gauss-Legendre quadrature.

Soil Moisture-Pressure Relationship

Two soil water retention and unsaturated hydraulic conductivity relationships were incorporated in the model. The first relationship is a simple linear function and was used primarily to verify numerical solutions. The second relationship was used in simulating laboratory tests. The linear relationship is illustrated in Fig. II-1 and is given by

$$\theta = \left(\frac{\theta_s - \theta_r}{\psi_d - \psi_r}\right)(\psi - \psi_d) + \theta_s \quad \text{for } \psi_r < \psi < \psi_d \tag{II-17}$$

$$\theta = \theta_s \quad \text{for } \psi > \psi_d \tag{II-18}$$

$$\theta = \theta_r \quad \text{for } \psi < \psi_r \tag{II-19}$$

$$K(\psi) = \left(\frac{K_s - K_r}{\psi_d - \psi_r}\right)(\psi - \psi_c) + K_s \quad \text{for } \psi_r < \psi < \psi_d \tag{II-20}$$

$$K = K_s \quad \text{for } \psi > \psi_d \tag{II-21}$$

$$K = K_r \quad \text{for } \psi < \psi_r \tag{II-22}$$

where θ is volumetric water content, θ_s is saturated water content, θ_r is residual water content, ψ_d is pressure head at the top of the capillary fringe, and ψ_r is the residual pressure head at θ_r.

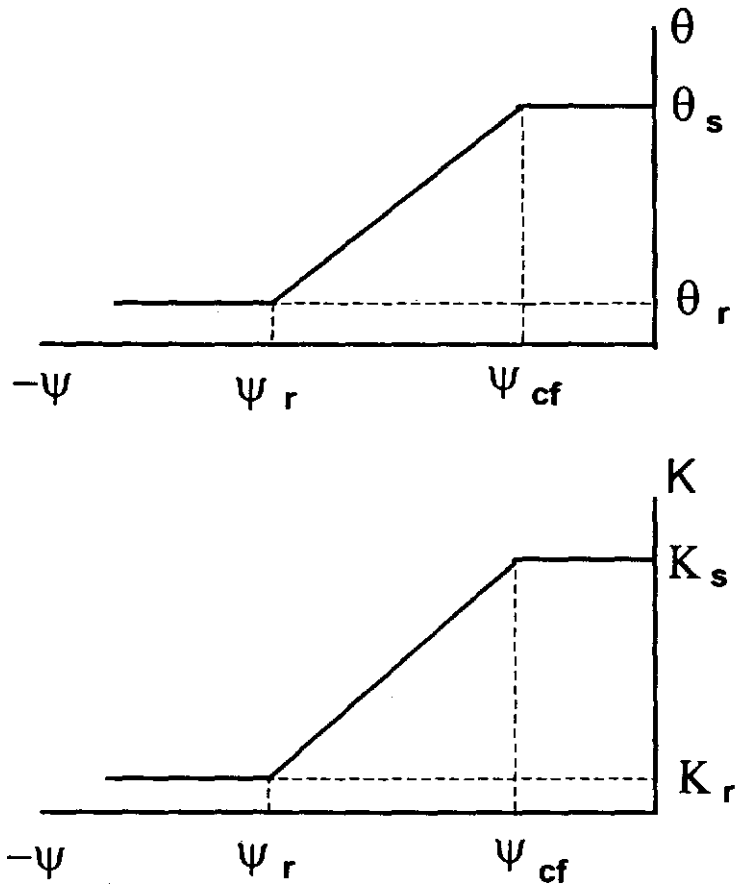

Figure II-1. Schematic of soil moisture - pressure head and hydraulic conductivity - pressure head relationships.

A second set of relationships incorporated in the model are those developed by van Genuchten (1980) and Mualem (1976) (Jury, Gardner, and Gardner, 1991). These relationships are given by

$$\tilde{\theta}(\psi) = [1 + \alpha(-\psi)^N]^{-M} \qquad \text{(II-23)}$$

$$K(\theta) = K_s \tilde{\theta}^{1/2}[1 - (1 - \tilde{\theta}^{1/M})^M]^2 \qquad \text{(II-24)}$$

with

$$\tilde{\theta} = (\theta - \theta_r) / (\theta_s - \theta_r); \quad M = 1 - 1/N \qquad \text{(II-25)}$$

where $\tilde{\theta}$ is a dimensionless volumetric water content, and α, N, and M are coefficients.

Boundary Conditions

Boundary conditions applicable to Eq. II-1 include prescribed flux or prescribed head. Prescribed flux boundary conditions are automatically incorporated into the Galerkin formulation. Prescribed head boundary conditions are imposed after assembly of the element equations. Initial conditions are imposed by prescribing head values throughout the solution domain at the initiation of computation.

A seepage face boundary condition contains both prescribed head and flux conditions and presents certain difficulties in a saturated-unsaturated groundwater flow model. One approach is to maintain a zero flux boundary condition above the exit point of the seepage face and a prescribed head boundary condition below the exit point. Under this method, the calculated outflow and pressure head at each boundary node are checked against the assumed boundary condition. If the prescribed head/flux boundary does not agree with the assumed boundary condition, the position of the prescribed head/flux boundary is adjusted and another iteration is performed (Neuman, 1973).

Unless an adaptive finite element approach is used, this method results in a discontinuous boundary condition in which the head/flux boundary can only be set on an element basis (at finite

element nodes). In an adaptive approach, boundary elements would be sized to accommodate the locus of the phreatic surface exit at the seepage face.

Another approach is to use a prescribed head boundary condition for both the saturated and unsaturated flow portion of the seepage face. A prescribed head boundary condition can be continuously varied, thus eliminating a discontinuous boundary between a head/flux boundary condition and the need to employ an adaptive finite element approach.

Investigation of evaporation from a bare soil surface shows that once the surface relative humidity falls below about 99%, the rate of evaporation is limited by the unsaturated hydraulic conductivity (Phillip, 1957; Eagleson, 1970). Thus at the soil surface, the moisture content and consequently the head would be a function of the surface relative humidity.

Immediately above the exit point of the phreatic surface on the seepage face and within the capillary fringe, pressure head values will decrease linearly. Above the capillary fringe, pressure head would be expected to decrease gradually to a final value controlled by the soil surface relative humidity (Fig. II-2). Based on these assumptions, the seepage face prescribed head boundary conditions above the phreatic surface exit point can be represented by

$$\psi = -(z - z_{sf}) \quad \text{for } z_{sf} < z < z_{cf} \tag{II-26}$$

$$\psi = (\psi_e - \psi_{cf} + \Delta z_e)\left(\frac{\Delta z_{cf}^2}{\Delta z_e^2}\right) - \Delta z_{cf} + \psi_{cf} \quad \text{for } z_{cf} < z < z_e \tag{II-27}$$

$$\psi = \psi_e \quad \text{for } z \geq z_e \tag{II-28}$$

with

$$\Delta z_e = z_e - z_{cf} \tag{II-29}$$

$$\Delta z_{cf} = z - z_{cf} \tag{II-30}$$

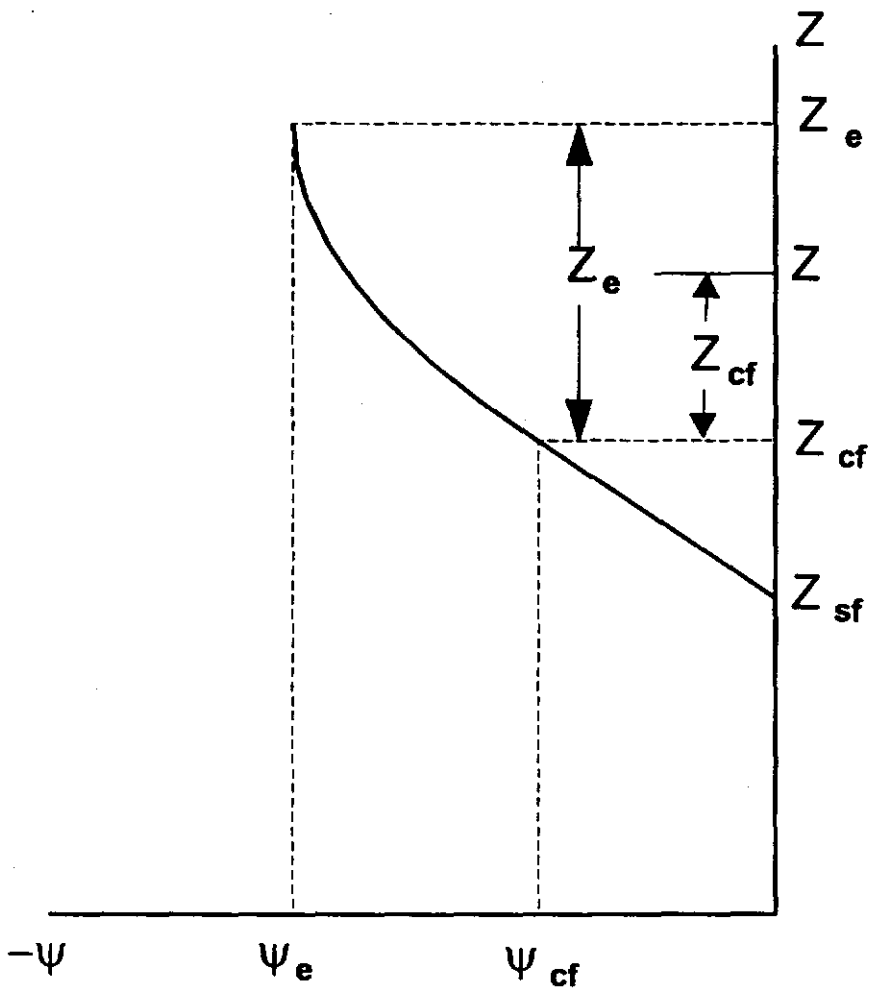

Figure II-2. Schematic of seepage face boundary condition.

where z_{sf} is the elevation of the exit of the phreatic surface at the seepage face; z_{cf} is the elevation at the top of the capillary fringe; z_e is the elevation corresponding to the maximum evaporation pressure head reduction, ψ_e; and ψ_{cf} is the pressure head at the top of the capillary fringe (Fig. II-2).

The location of the seepage face exit point, z_{sf}, was determined for each iteration by assuming that the entire seepage face was saturated and determining the flow direction (inflow or outflow) for each node. Nodes located above the seepage face exit point were inflow nodes while those below the exit point were outflow nodes. The location of the exit point was determined by using linear interpolation to locate the point of zero outflow between the two nodes which exhibited a change in flow direction.

SOIL STRESS-STRAIN MODELING

Introduction

Stress-strain problems can be simplified from three to two dimensions when (1) a thin plate is loaded uniformly across its thickness in a direction parallel to the lateral surfaces of the plate, or (2) where the normal strain for one surface and shear strain directed toward that surface, are zero. The first case is known as a plane stress analysis and requires that $\sigma_{zz} = \sigma_{xz} = \sigma_{yz} = 0$. The second case is known as a plane strain analysis and requires that $\varepsilon_{zz} = \varepsilon_{xz} = \varepsilon_{yz} = 0$.

A two-dimensional analysis of channel bank failure falls clearly into the plane strain case. To maintain compatibility with axis conventions used the ground water model, the plane strain analysis was formulated in the x-z plain. The plane strain assumptions require that $\varepsilon_{xy} = \varepsilon_{yz} = \varepsilon_{yy} = 0$.

Governing Equation and Finite Element Formulation

The mechanical behavior of soil is governed by the equations of static equilibrium, the small strain-displacement equations, and an accompanying constitutive relationship. Although a finite element formulation can be developed from the equations of static equilibrium, it is more convenient to adopt an energy approach which leads directly to the finite element formulation.

The principle of virtual displacements is a special case of the more general principle of virtual work and requires that the work done by the external forces on a structural system be equal to the increase in internal strain energy of the system for any set of admissible virtual displacements. The principle of virtual work serves both as a basic energy relationship and a weak form of the

equilibrium equations which can be used directly to develop the nonlinear elastoplastic finite element formulation for soil stress-strain modeling. (Stasa, 1985; Zienkiewicz and Taylor, 1989).

The principle of virtual work can be expressed as

$$\underset{\text{Internal Energy}}{\int_{v^e}\{\delta\varepsilon\}^T\{\sigma\}dv} = \underset{\text{Body Forces}}{\int_{v^e}\{\delta u\}^T\{b\}dv} + \underset{\text{Pressure and Shear}}{\int_{s^e}\{\delta u\}^T\{s\}ds} + \underset{\text{Point Loads}}{\sum\{\delta u\}^T\{f_p\}} \qquad \text{(II-31)}$$

where $\delta\varepsilon$ is virtual strain, δu is virtual displacement, σ is stress, b is body force, s is surface traction, f_p is a point load, and v^e and s^e indicate volume and surface integrals over the finite element, respectively (Stasa, 1985).

Using the Lagrangian small strain relationships, virtual strain can be expressed as

$$\{\delta\varepsilon\} = [L]\{\delta u\} = [L][N]\{\delta a^e\} = [B]\{\delta a^e\} \qquad \text{(II-32)}$$

where [L] is a linear operator matrix given by

$$L = \begin{vmatrix} \frac{\partial}{\partial x} & 0 \\ 0 & \frac{\partial}{\partial z} \\ \frac{\partial}{\partial z} & \frac{\partial}{\partial x} \end{vmatrix} \qquad \text{(II-33)}$$

δu is virtual displacement given by

$$\delta u = [N]\{\delta a^e\} \qquad \text{(II-34)}$$

[N] is the shape function matrix, δa^e is element nodal virtual displacement, and [B] is the strain nodal displacement matrix.

Substituting Eqs. II-32 and II-34 into Eq. II-31 yields

$$\{\delta a^e\}^T\left(\int_{v^e}[B]^T\{\sigma\}dv - \int_{v^e}[N]^T\{b\}dv - \int_{s^e}[N]^T\{s\}ds - \sum[N]^T\{f_p\}\right) = 0 \tag{II-35}$$

Since δa_e is not necessarily zero, the term in parentheses must be zero. After substitution of a constitutive relationship

$$\{\sigma\} = [D]\{\varepsilon\} + \sigma_0 \tag{II-36}$$

where [D] is a linear constitutive matrix, ε is strain, and σ_0 is initial stress, and by noting that $\{\varepsilon\} = [B]\{a^e\}$, where the virtual displacement δa^e has been replaced with the nodal displacement, a^e, Eq. II-35 can be written

$$\int_{v^e}([B]^T[D][B]dv)a^e - \int_{v^e}[N]^T\{b\}dv + \int_{v^e}[B]^T\{\sigma_o\}dv - \int_{s^e}[N]^T\{s\}ds - \sum[N]^T\{f_p\} = 0 \tag{II-37}$$

In this application, the initial stress, σ_o, consisted of the initial K_o overburden pressure and soil cohesive pressure. For nonlinear elastoplastic constitutive relationships, Eq. II-37 must be solved using iterative or incremental techniques.

An incremental elastoplastic constitutive relationship which follows the normal or associative rule (incremental strain is orthogonal to yield surface) can be written (Desai and Siriwardane, 1984)

$$\{d\sigma\} = \left([D] - \frac{[D][A][A]^T[D]}{[A]^T[D][A] - H_p}\right)\{d\varepsilon\} \tag{II-38}$$

where [D] is an elastic constitutive relationship, [A] is the gradient of the yield function, and H_p is the plastic modulus. The plastic modulus is

$$H_p = \frac{\partial F}{\partial \varepsilon_v^p} A_i \tag{II-39}$$

where F is a yield function, ε^p_v is plastic volumetric strain, and A_i is the trace of the gradient matrix. For a two-dimensional plain strain formulation, the gradient of the yield function is given by

$$\{A\}^T = \frac{\partial F}{\partial \sigma_i} = \left(\frac{\partial F}{\partial \sigma_{xx}}, \frac{\partial F}{\partial \sigma_{zz}}, \frac{\partial F}{\partial \sigma_{xz}}, \frac{\partial F}{\partial \sigma_{yy}} \right) \tag{II-40}$$

The modified Cam clay yield function was used in this formulation

$$F = M^2 J_1^2 - M^2 J_1 J_{01} + 27 J_{2D} = 0 \tag{II-41}$$

where M is the slope of the critical state line in triaxial stress space, J_1 is the first invariant of the stress tensor, J_{2D} is the second invariant of the deviatoric stress tensor, and J_{01} is a hardening parameter.

The critical state line is given by

$$\sqrt{J_{2D}} = \frac{M}{3\sqrt{3}} J_1 \tag{II-42}$$

For the modified Cam clay model, the plastic modulus, H_p, is

$$H_p = - \frac{M^2 J_1 J_{01} (1 + e_o)}{\lambda - \kappa} A_i \tag{II-43}$$

where e_o is the initial void ratio, λ is the slope of the normal consolidation line, κ is the slope of the unloading or recompression line, and

$$A_{xx} = 27\sigma_{xx} + (2M^2 - 9)J_1 - M^2J_{01} \quad \text{(II-44)}$$

$$A_{zz} = 27\sigma_{zz} + (2M^2 - 9)J_1 - M^2J_{01} \quad \text{(II-45)}$$

$$A_{yy} = 27\sigma_{yy} + (2M^2 - 9)J_1 - M^2J_{01} \quad \text{(II-46)}$$

The modified Cam clay yield function is illustrated in Fig. II-3. For stress points which lie inside the yield function ($F < 0$), strain is elastic and an elastic constitutive relationship is applicable. For stress points which lie on or outside the yield surface ($F \geq 0$), elastoplastic strain occurs and the yield surface moves outward as strain hardening occurs. Failure occurs when the stress path reaches the critical state line.

Forces

Following a derivation provided by Bear (1972), five forces were used to describe the mechanical behavior of channel banks: (1) weight of the soil matrix; (2) fluid pressure gradient; (3) fluid drag force; (4) weight of soil moisture in the unsaturated zone; and (5) soil cohesive force. Soil weight is a body force given by

$$F_s = \gamma_m(1 - n) \quad \text{(II-47)}$$

where F_s is the soil weight per unit volume, γ_m is the soil mineral unit weight, and n is porosity.

For saturated conditions, the fluid pressure is

$$F_p^s = -(1 - n)\nabla p \quad \text{(II-48)}$$

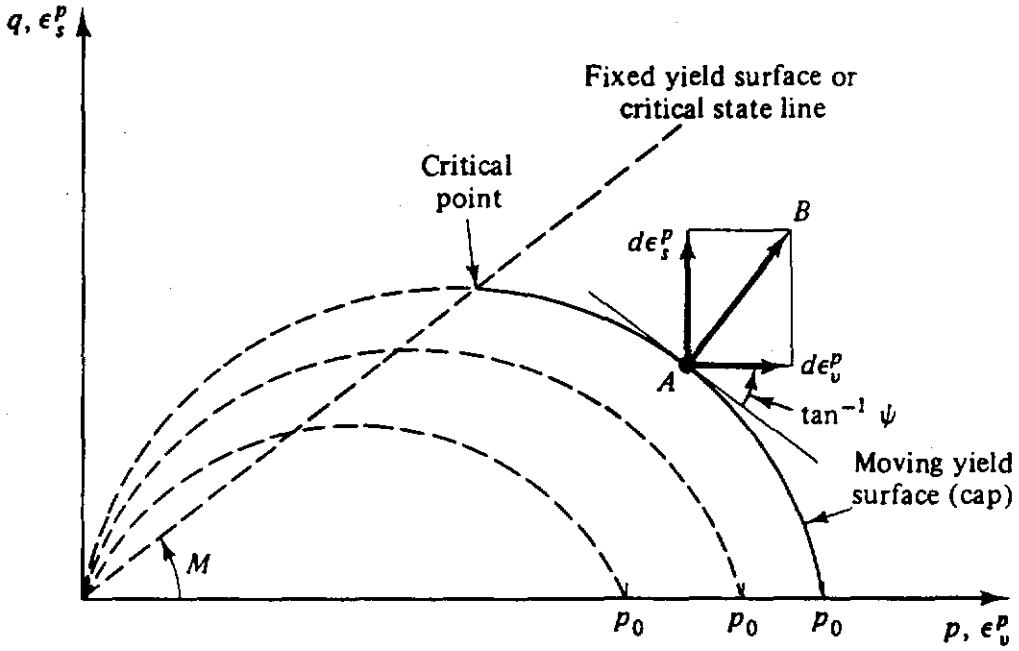

Figure II-3. Schematic of modified Cam clay yield function in triaxial stress space (Roscoe and Burland, 1968; Desai and Siriwardane, 1984).

where F_p^s is the fluid pressure force per unit volume and p is pressure.

For unsaturated conditions, soil cohesive forces including matric suction and electrochemical forces between soil particles produce a stress distribution in the unsaturated soil matrix. Based on a derivation presented in a subsequent section of this Chapter, the cohesive pressure can be expressed as

$$u_c = \frac{p(M - M_u) - q_c}{M} \tag{II-49}$$

where u_c is the cohesive pressure, p is total mean pressure, q_c is the intercept of the failure line with the deviatoric stress axis, M_u is the slope of the failure line for an unsaturated soil, and M is the slope of the failure line for a normally consolidated saturated soil. The cohesive pressure produces a compressive stress distribution which varies with initial void ratio, water content, and applied loading.

The drag force resulting from head loss is given by

$$F_d^s = -n\gamma_f \nabla h \tag{II-50}$$

for saturated conditions and

$$F_d^{us} = -\theta_v \gamma_f \nabla h \tag{II-51}$$

for unsaturated conditions where F_d^s and F_d^{us} are the drag forces per unit volume for saturated and unsaturated conditions, respectively; θ_v is volumetric water content, and γ_f is the fluid unit weight.

Weight of the soil moisture in the unsaturated zone is given by

$$F_m^{us} = -\theta\gamma_f \tag{II-52}$$

where F_m^{us} is the weight of soil moisture per unit volume in the unsaturated zone.

Solution of Elastoplastic Stress-Strain Equation

General solution

Basic methods for solving nonlinear stress-strain relationships include direct iteration, Newton-Raphson, tangent stiffness, and initial stiffness methods (Owen and Hinton, 1980). A method presented by Siriwardane and Desai (1983) which combines incremental and iterative techniques was employed in this model. The method is given by the incremental linear equation

$$[K(u)]^{i}\{\Delta u\}^{i+1} - (\{g\}^{i+1} - \{g\}^{i}) = \{R_f\} \tag{II-53}$$

where g is the force vector and R_f is a residual force vector which is a measure of solution convergence. Successive iterations were performed until R_f was reduced to a suitable tolerance.

Solution at ultimate strength

At each incremental increase in load, the stress must be checked at each Gauss integration point to determine if the yield function was exceeded ($F > 0$). If the yield function was exceeded, the stress at the Gauss integration point is in the failure zone and an iterative procedure based on the work of Siriwardane and Desai (1983) was used to determine a new stress distribution which did not exceed the yield function.

A hypothetical incremental increase in stress which exceeds the yield function is schematically illustrated in Fig. II-4. The intersection of the ultimate strength line and the line segment (A - B) in Fig. II-4 gives the coordinates in J_1 - J_{2D} space of the stress point on the yield function.

The total differential of J_1 can be expressed as

$$dJ_1 = \{\frac{\partial J_1}{\partial \sigma_{ij}}\}^T \{d\sigma_{ij}\} \tag{II-54}$$

Multiplying both sides by

$$\{\partial J_1/\partial \sigma_{ij}\} \tag{II-55}$$

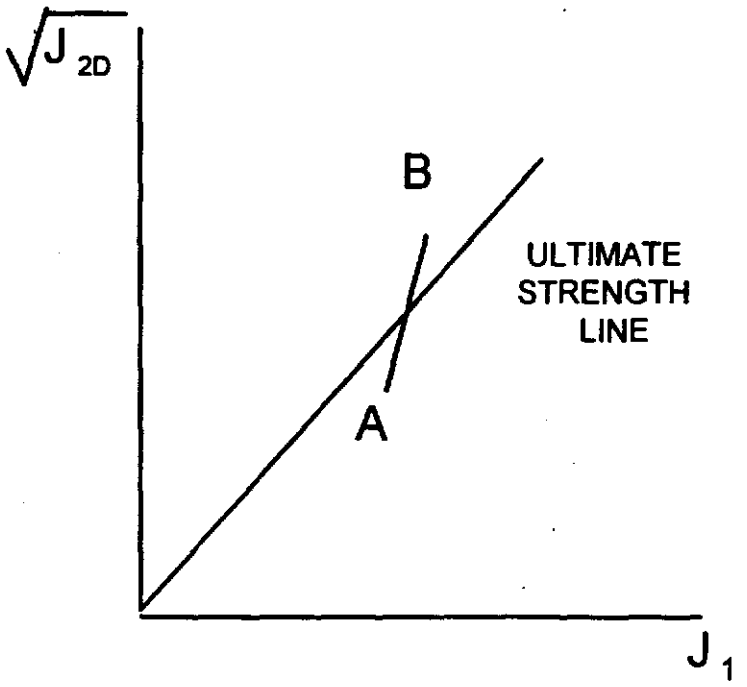

Figure II-4. Schematic of incremental stress exceeding ultimate strength.

and solving for $d\sigma_{ij}$ gives

$$\{d\sigma_{ij}\} = \frac{dJ_1\{\frac{\partial J_1}{\partial \sigma_{ij}}\}}{\{\frac{\partial J_1}{\partial \sigma_{ij}}\}^T\{\frac{\partial J_1}{\partial \sigma_{ij}}\}} \qquad \text{(II-56)}$$

A similar expression for $d\sigma_{ij}$ in terms of dJ_{2D} can also be developed

$$\{d\sigma_{ij}\} = \frac{dJ_{2d}\{\frac{\partial J_{2D}}{\partial \sigma_{ij}}\}}{\{\frac{\partial J_{2D}}{\partial \sigma_{ij}}\}^T\{\frac{\partial J_{2D}}{\partial \sigma_{ij}}\}} \qquad \text{(II-57)}$$

Incremental stresses determined by Eqs. II-56 and II-57 can be added to give $d\sigma_{xx}$, $d\sigma_{zz}$, $d\sigma_{xy}$, and $d\sigma_{yy}$ necessary to return J_1 and J_{2D} to the ultimate strength line.

If the above described iterative scheme was unable to reduce the stress to the ultimate strength line, the elastoplastic constitutive relationship for the Gauss integration point was replaced with a weak elastic constitutive relationship.

GENERAL SOLUTION ALGORITHM

The previously described model requires the solution of two sets of simultaneous equations: one for groundwater flow and another for stress-strain. Boundary conditions required for solution include a specified flux, or either a steady state or dynamic prescribed head boundary condition for the groundwater model, and a prescribed displacement boundary condition for the stress-strain model. Initial conditions include either a total head or pressure head distribution throughout the porous medium.

Solution was accomplished by using a staggered process in which the groundwater flow equation was solved first to determine seepage force and soil cohesive force, and then the stress-strain equation was solved. For high hydraulic gradients and resulting large seepage forces, it was necessary to incrementally increase the gradient to maintain numerical stability. When an element reached the failure point, the elastoplastic constitutive relationship was replaced with a weak elastic relationship. The soil moisture and stress-strain equations were solved using the active zone equation solver to perform LU decomposition (Stasa, 1985).

DEVELOPMENT OF A SOIL COHESIVE RELATIONSHIP

Ultimate Strength Cohesive Pressure Formulation

As illustrated in Fig. II-5, cohesive pressure can be defined as the difference in mean pressure between the failure line for an unsaturated soil and the failure line for a normally consolidated saturated soil. Adopting a total stress approach in p - q stress space, the failure line for an unsaturated soil (upper line in Fig. II-5) can be represented by

$$q_f = M_u p + q_c \tag{II-58}$$

where M_u is the slope of the failure line for an unsaturated soil, p is mean pressure, and q_c is the q-axis intercept of the failure line.

The failure line for a normally consolidated saturated soil (lower line in Fig. II-5) can be represented by

$$q_f = M(p - u_c) \tag{II-59}$$

where M is the slope of the failure line for a normally consolidated saturated soil and u_c is the cohesive pressure, which is negative. Equating deviatoric stresses in Eqs. II-58 and II-59 yields an expression for the cohesive pressure

$$u_c = \frac{p(M - M_u) - q_c}{M} \tag{II-60}$$

As indicated by Eq. II-60, the cohesive pressure varies with the mean pressure, p, and is thus a function of the applied forces including overburden pressure. Eq. II-60 contains three quantities (M, M_u, and q_c) which must be determined. Further, one might expect that M, M_u and q_c would be a function of other soil parameters such as water content, degree of saturation, and void ratio.

Definition of Parameters

Drained compression triaxial soil testing was conducted on unsaturated samples of Maury silt loam (Unified Classification CL; LL = 34, PI = 10) to develop a database for determining the parameters M , M_u and q_c in Eq. II-60 (Rohlf 1993).

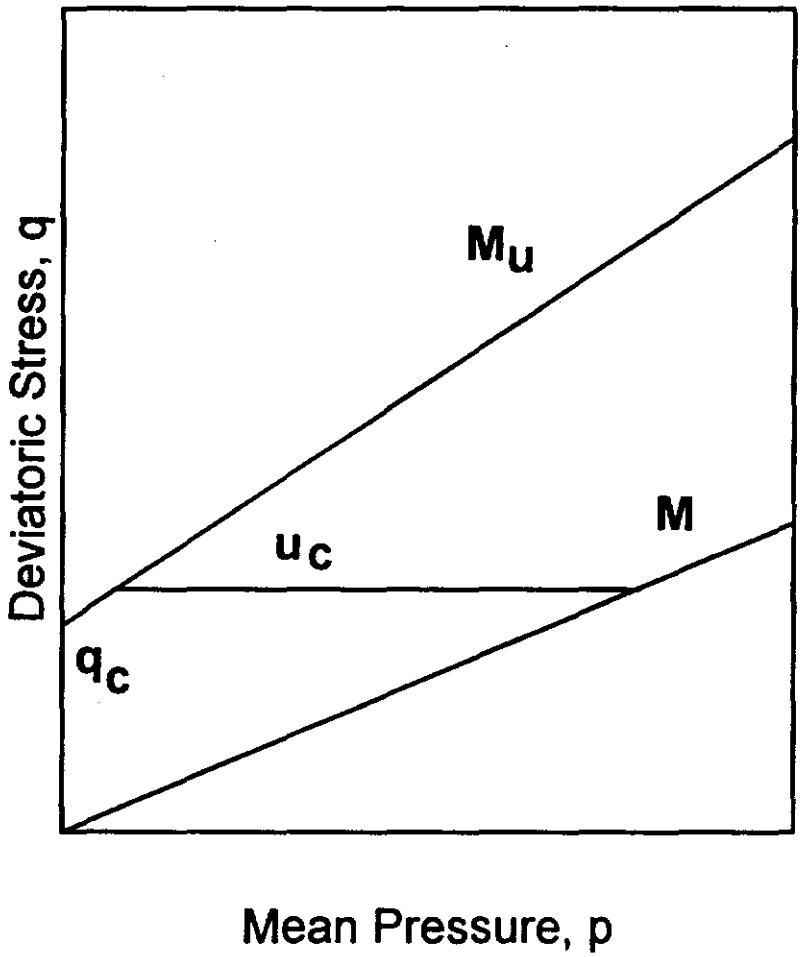

Figure II-5. Cohesive pressure schematic.

Samples for triaxial testing were prepared in plexiglass molds in sets of five. Each mold had two sections (lower and upper) creating a total of ten samples for each sample set (Fig. II-6). Sample sets were designated as s1 - s6 for sample sets 1 through 6 and FT1 - FT4 for samples prepared in conjunction with channel bank flume tests 1 through 4. Sample sets s1 through s3 were used to develop the triaxial testing methodology, and the remaining sample sets (s4 - s6 and FT1 - FT4) were used to develop failure curves. A more complete description of the testing methodology is provided by Rohlf (1993).

Sample sets s4 through s6 and FT-1 through FT-4 were separated by mold section (lower, upper) and used to develop failure lines. All failure lines produced a q-axis intercept greater than zero. The q-axis intercept and slope of the failure line along with the void ratio, gravimetric water content, and degree of saturation are presented in Table II-1 for each sample set and mold section.

Graphs of q_c versus e_o (initial void ratio) and q_c versus θ_g (gravimetric water content) are presented in Figs. II-7 and II-8, respectively. Examination of Fig. II-7 shows that a good relationship exists between q_c and e_o. Fig. II-8 shows q_c increasing with an increase in θ_g which is a questionable trend. A multiple regression analysis using an equation of the form

$$q_c = ae_o^b\theta_g^c \qquad \text{(II-61)}$$

where a, b, and c are regression constants, also indicated that no significant additional variance was accounted for by the addition of θ_g. However, a closer examination of Fig. II-8 for points having relatively constant void ratios indicate that q_c may be decreasing with an increase in θ_g (Fig. II-9).

The overall trend displayed in Figs. II-8 and II-9 which shows q_c increasing with θ_g is likely the result of an underlying correlation between void ratio and water content resulting from the cyclic compaction technique used to prepare the samples. Fig. II-10 contains a graph of e_o versus θ_g and shows e_o generally decreasing with increasing water content. The cyclic soil compaction technique produced greater compaction (lower void ratio) as water content increased. Thus, the relationship between q_c and θ_g contained in Fig. II-8 is actually a

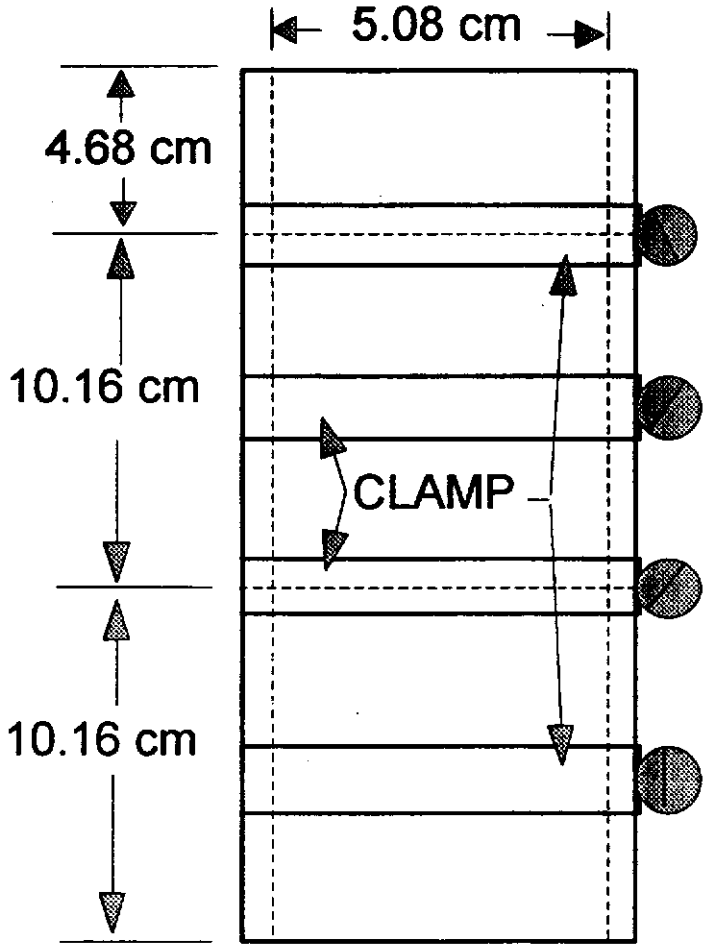

Figure II-6. Sample Mold.

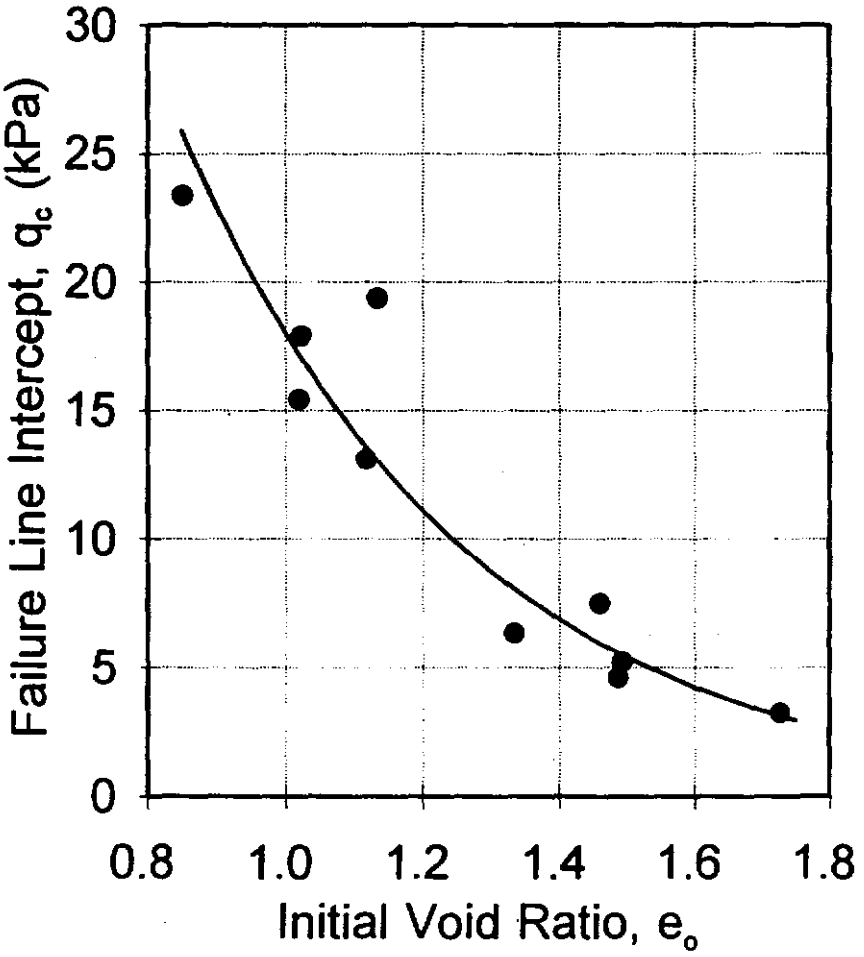

Figure II-7. Failure line intercept versus void ratio.

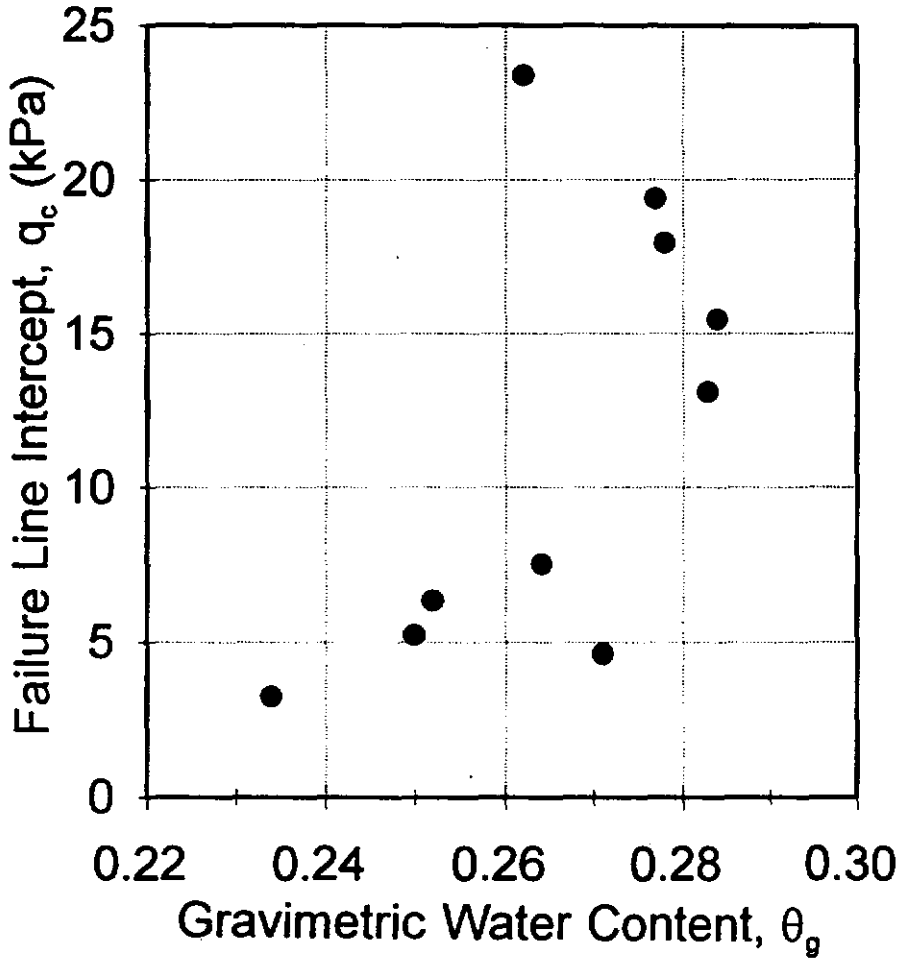

Figure II-8. Failure line intercept versus gravimetric water content.

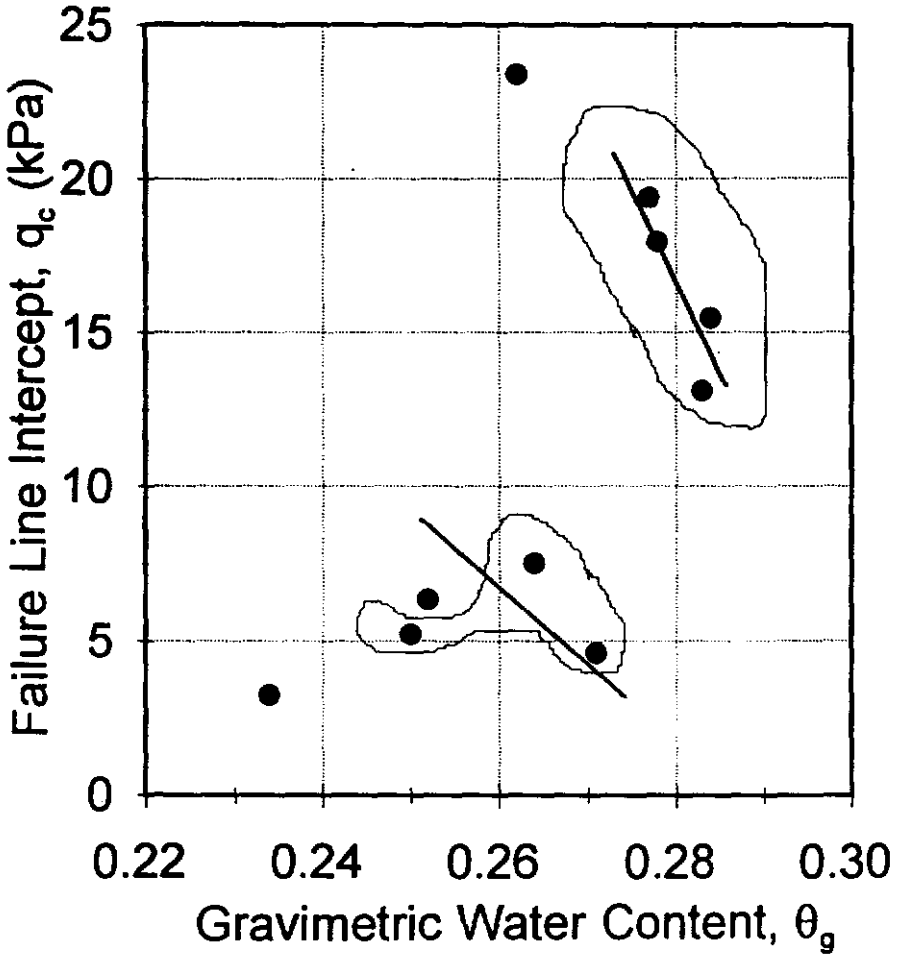

Figure II-9. Decrease in q_c with increasing water content for points having relatively constant void ratio.

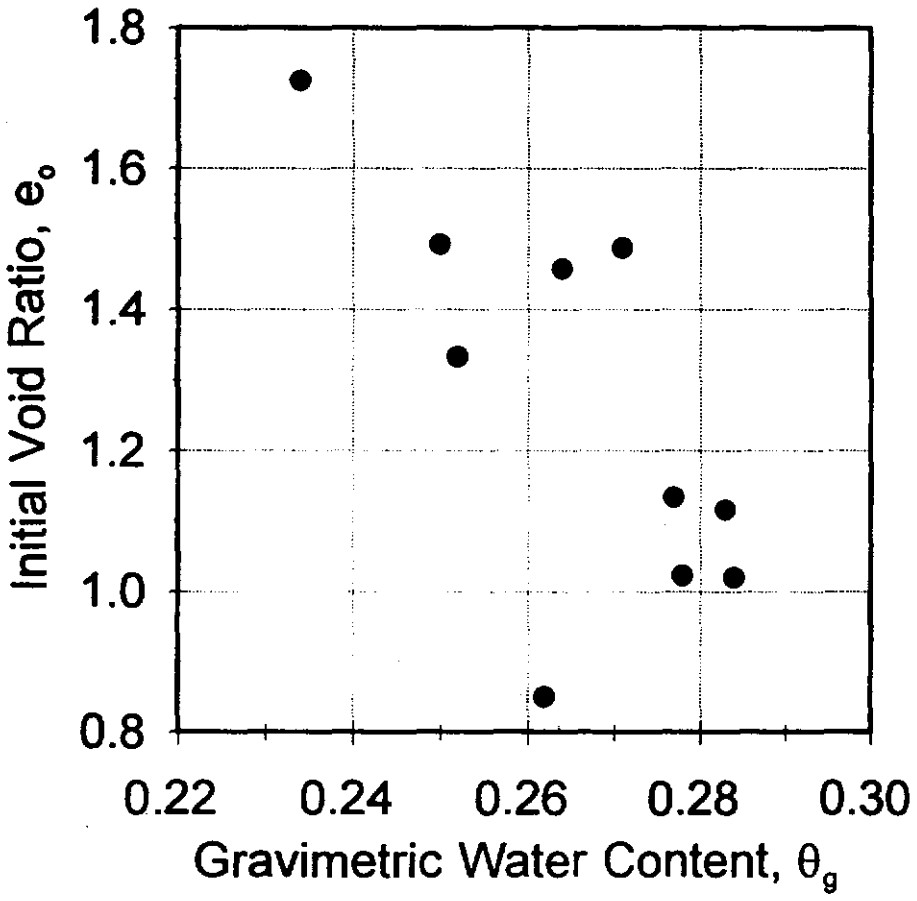

Figure II-10. Void ratio versus gravimetric water content.

Table II-1
Failure Line Intercept and Slope

Set	q_c (kPa)	M_u	e_o	θ_g	S_r
S4	23.4	1.25	.851	.262	.825
S5	7.5	1.10	1.459	.264	.485
S6	4.6	1.33	1.488	.271	.488
FT1 - L	15.4	.87	1.021	.284	.746
FT1 - U	17.9	1.16	1.023	.278	.728
FT2 - L	13.1	.98	1.117	.283	.679
FT2 - U	19.4	.92	1.134	.277	.655
FT3 - U	3.2	1.62	1.726	.234	.363
FT4 - L	6.3	1.38	1.334	.252	.506
FT4 - U	5.2	1.52	1.439	.250	.449

reformulation of the q_c - e_o relationship expressed through the high correlation between e_o and θ_g.

Performing a regression analysis on the data displayed in Fig. II-7 and also assuming an exponential reduction in q_c with degree of saturation yields an expression for the cohesive intercept as a function of initial void ratio and degree of saturation

$$q_c = a \exp[b_1 e_o + b_2 (S_r^o - S_r)] \qquad \text{(II-62)}$$

where S_r is degree of saturation, S_r^o is the initial degree of saturation, a and b_1 are constants determined by regression, and b_2 is a calibration coefficient. The first term in Eq. II-62 is similar to a relationship discussed by Schofield and Wroth (1968) who found, after examining Hvorslev's data, that cohesion in the Coulomb equation could be expressed as an exponential function of water content for overconsolidated saturated soils (Hvorslev, 1937). Eq. II-62

allows q_c to vary with both void ratio and water content. The calibration constant, b_2, was determined by the desired reduction in q_c at saturation.

Graphs of M_u versus e_o and M_u versus θ_g are presented in Figs. II-11 and II-12, respectively. The relationship between M_u and e_o has considerable scatter and seems to indicate that M_u is increasing as void ratio increases. Since one would expect that M_u would decrease with increasing void ratio, it is likely that the increasing relationship between M_u and e_o is caused by the previously discussed underlying correlation between void ratio and water content. Fig. II-12 shows that a reasonable relationship exists between M_u and θ_g.

Noting that water content can be expressed as

$$\theta_g = \frac{e_o S_r}{G_s} \tag{II-63}$$

where G_s is specific gravity of the soil solids, allows θ_g to be replaced by $e_o S_r/G_s$ in Fig. II-12. The relationship in Fig. II-12 can be represented with the equation

$$M_u = -\beta \, \mathrm{Tan}^{-1}[(\frac{e_o S_r}{G_s} - d)/c] + M_o \tag{II-64}$$

where

$$\beta = \frac{M_o - M}{\pi/2} \tag{II-65}$$

c and d are regression constants, and M_o is a reference failure line slope. The compatible linear regression equation for Eq. II-64 is

$$\theta_g = c\mathrm{Tan}(\frac{M_o - M_u}{\beta}) + d \tag{II-66}$$

The relatively small amount of scatter in the M_u - θ_g relationship (R^2 = .85) is remarkable considering that most of the failure lines were determined with only two points. Eq. II-62 and II-64 allow the cohesive intercept and slope of the failure line to be determined by the initial void ratio, gravimetric water content, and degree of saturation and specific gravity of the soil solids. Substituting Eq. II-62 and II-64 into Eq. II-60 yields an expression for the cohesive pressure.

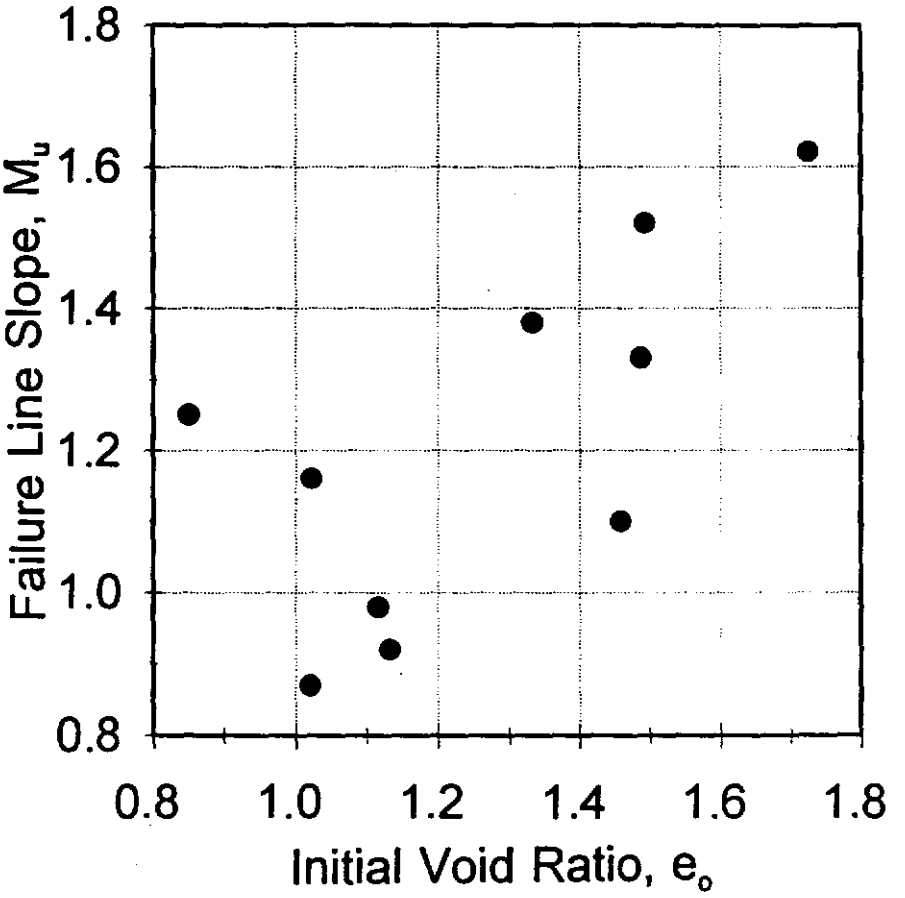

Figure II-11. Failure line slope versus void ratio.

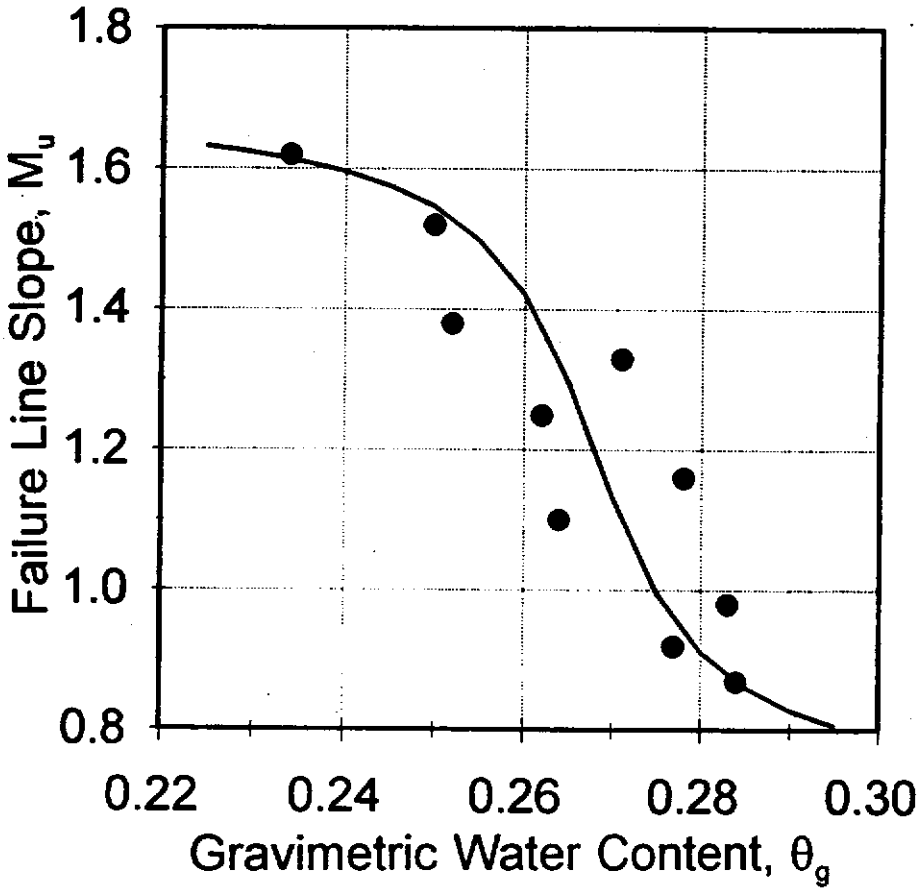

Figure II-12. Failure line slope versus gravimetric water content.

$$u_c = \frac{p'M - \beta \mathrm{Tan}^{-1}\left(\frac{\theta_g - d}{c}\right) + M_u) - a\exp(b_1 e_o + b_2(S_r^o - S_r))}{M} \qquad \text{(II-67)}$$

At saturation

$$u_c = \frac{-a\exp(b_1 e_o + b_2 (S_r^o - 1))}{M} \qquad \text{(II-68)}$$

The slope of the failure line for a saturated soil, M, was determined from a plot of M_u verses S_r (Fig. II-13). The relationship in Fig. II-13 shows considerable scatter, however, the upper and lower limits were linearly extended to $S_r = 1$ to determine M for a saturated soil. The relationship between M_u and θ_g (Fig. II-12) removes much of the scatter seen in Fig. II-13, but this relationship is difficult to project to saturation.

Although the cohesive pressure relationship given by Eq. II-67 was determined at failure, it was assumed to apply at all stress levels (Rohlf, 1993). This must be treated as a simplifying assumption subject to further evaluation since constant water content triaxial tests conducted by Satija (1978) (Fredlund and Rahardjo, 1993) indicate that the matric suction component of cohesion may change significantly during shearing.

DETERMINATION OF λ AND κ

Hydrostatic compression tests were conducted on five samples with varying initial void ratios (Rohlf ,1993). The effective mean pressure ($p' = p - u_c$) was plotted against void ratio in log(p') - e space. The resulting values of λ and κ (slope of the recompression and compression lines, respectively) and e_o are presented in Table II-2. Plots of λ and κ versus e_o are also presented in Fig. II-14. The curves in Fig. II-14 were fitted with the equations

$$\lambda = \exp(f + ge_o + he_o^2) \qquad \text{(II-69)}$$

and

$$\kappa = \exp(r + se_o) \qquad \text{(II-70)}$$

where f, g, h, r, and s are regression coefficients.

Coefficients for the above equations are contained in Table II-3.

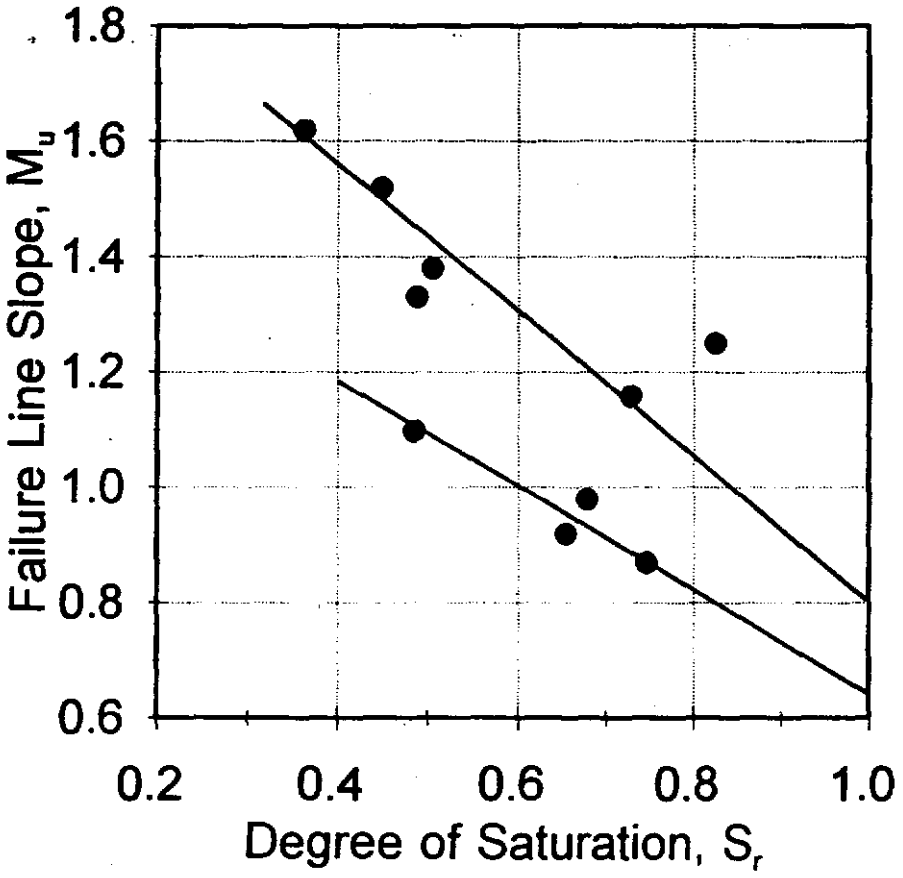

Figure II-13. Failure line slope versus degree of saturation.

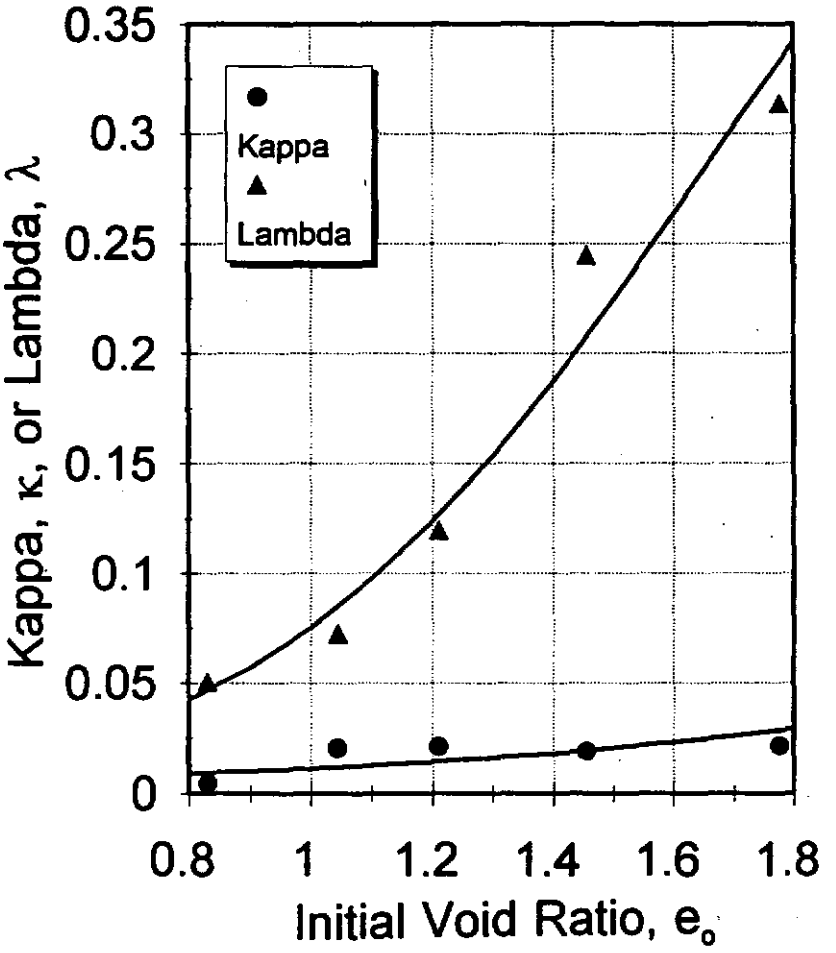

Figure II-14. Lambda and Kappa versus void ratio.

Table II-2
Hydrostatic Compression Test Results

Test	κ	λ	e_o
T117	.005	0.051	.831
T126	.019	0.245	1.456
T131	.021	0.073	1.043
T136	.021	0.120	1.211
T140	.022	0.314	1.777

Table II-3
Coefficient Values

Coefficient	Units	Value	R^2
a	kPa	201.	.92
b_1	(1)	-2.41	.92
b_2	(1)	(3)	(2)
c	(1)	.0108	.85
d	(1)	.267	.85
M_o	(1)	1.21	.85
M	(1)	.70	(2)
f	(1)	-6.22	.97
g	(1)	4.60	.97
h		-.968	.97
r	(1)	-5.67	.44
s	(1)	1.18	.44

(1) Dimensionless coefficient.
(2) Regression not performed to determine parameter value.
(3) b_2 varied depending on desired decrease in q_c at saturation.

SUMMARY

A saturated-unsaturated groundwater flow and elastoplastic stress-strain finite element formulation was developed for simulating the mechanical behavior of channel banks. The model coupled the two-dimensional saturated-unsaturated groundwater flow equation with a plane strain formulation of the virtual work equation. The constitutive relationship used the modified Cam clay yield function. The model included the effects of seepage force and variation in soil cohesive strength due to changes in water content and void ratio. The groundwater equation was solved first to determine seepage force and soil cohesive force, and then the stress-strain equation was solved. Upon reaching the failure point, the elastoplastic constitutive relationship was replaced with a weak elastic relationship.

The cohesive pressure relationship was defined as the difference in mean pressure between the saturated and unsaturated failure lines in triaxial stress space. The cohesive pressure varies with mean pressure and was found to be a function of initial void ratio and soil water content.

Expressions for the slope of the normal consolidation line, λ, and unloading-reloading line, κ, were also developed. Both of these parameters were a function of initial void ratio.

CHAPTER III

MODEL VERIFICATION AND LABORATORY EXPERIMENTS

The saturated-unsaturated groundwater flow and stress-strain finite element model described in Chapter II was verified by comparison with one-dimensional analytic solutions, other numerical solutions, triaxial tests, and laboratory experiments. The following sections provide a description of model verification using other numerical solutions, triaxial tests, and selected laboratory results. A more complete description of model verification is provided by Rohlf (1993).

COMPARISON WITH NUMERICAL SOLUTIONS FOR THE MODIFIED CAM CLAY YIELD FUNCTION

The elastoplastic solution algorithm with the modified Cam clay yield function was compared with the numerical solutions of Desai, Zienkiewicz, and Roscoe-Burland. The Desai and Zienkiewicz solutions were obtained from graphs (Siriwardane and Desai, 1983). The Roscoe-Burland solution is applicable only to triaxial stress space (Roscoe and Burland, 1968). Results of the numerical solutions are presented in Fig. III-1. Agreement between all solutions is very good except near ultimate strength. At ultimate strength, the load increment and other differences in the numerical solutions are magnified.

COMPARISON WITH TRIAXIAL TESTS

The model was used to simulate one of the triaxial tests used in developing the cohesive pressure relationship (T127). This simulation provides an indication of the ability of the cohesive pressure relationship and modified Cam clay yield function to reproduce triaxial tests. The lateral confining pressure provided by the rubber membrane was modeled with a hoop stress equation

$$\sigma_m = - \frac{2\, t_o E(\varepsilon_3 + 2\nu\varepsilon_3^2)}{d_o(1 - \varepsilon_3)(1 - \varepsilon_1)} \qquad \text{(III-1)}$$

where σ_m is the membrane confining pressure, t_o is the thickness of the membrane, E is the elastic modulus of the membrane, d_o is the membrane diameter, ε_3 is the lateral stress, and ε_1 is the axial stress (t_o=0.04 cm, E=12,500 kdyne/cm^2, d_o=5.00 cm, ν=.5) (Rohlf, 1993). Results of the simulation comparing deviatoric stress, axial strain, and volumetric strain are presented in Figs. III-2 through III-4. Figs. III-2 and III-3 indicate that the model does a good job of

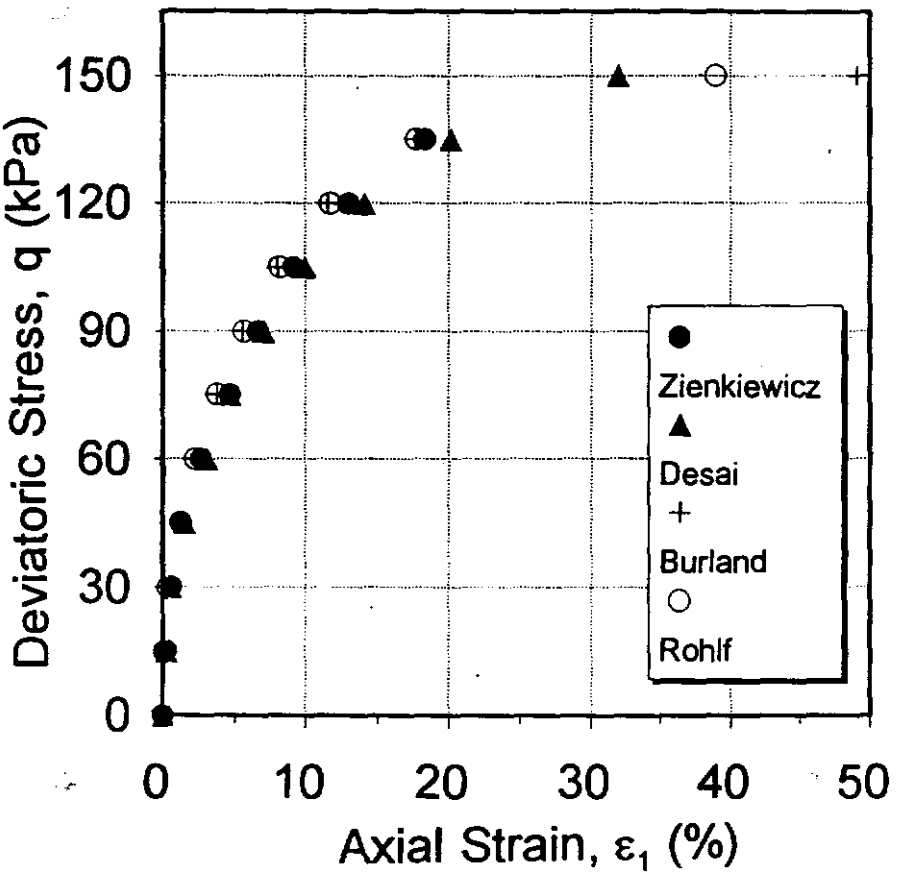

Figure III-1. Comparison of numerical solutions for the modified Cam clay constitutive relationship.

reproducing the p - q relationship and a reasonable job of simulating axial and lateral strain. However as demonstrated by Fig. III-4, volumetric strain predicted by the model is considerably greater than the actual strain. The over prediction is due to the inability of the modified Cam clay relationship to model volumetric expansion at failure. Although the modified Cam clay constitutive relationship over predicts volumetric strain, it may still provide insight into channel bank failure mechanisms for saturated and unsaturated soils.

LABORATORY EXPERIMENTS

Channel banks were formed using a plexiglas flume 90 cm long x 25 cm high x 15.24 cm wide which was divided into a soil compartment (60 cm) and a water compartment (30 cm). A removable plexiglas retaining wall divided the soil and water compartments. A longitudinal cross section of the flume is given in Fig. III-5.

To reduce layering and the resulting differential permeability which can occur with impact compaction, a cyclic soil compactor was designed for this project. Soils which are subjected to cyclic loading, either inside or outside the yield function, incur plastic strain. A load platform actuated by a cam mechanism was constructed to allow cyclic loading of the entire flume. Soil sample molds for forming samples for triaxial testing were mounted on the load platform along with the flume. Thus except for possible differences in sidewall effects, soil in the sample molds was subjected to the same compactive energy as soil in the flume. The desired degree of compaction was controlled by regulating the rotational speed of the cam and number of cycles. A cross section of the cyclic compactor is presented in Fig. III-6. Design details for the flume and cyclic soil compactor are provided by Rohlf (1993).

Compaction in the flume and sample molds was achieved by placing soil in layers approximately 5 cm thick and subjecting the flume and sample molds to 20 loading cycles for each layer. Styrofoam beads approximately 2 mm in diameter were placed in a grid pattern along one wall of the flume to measure displacement. The walls of the flume were lubricated with Pam (corn oil based lubricant) to reduce friction.

The laboratory experiments consisted of (1) soil preparation, (2) soil compaction in the flume, and (3) generating a hydrograph on the exposed channel bank face. Soil (air dry Maury silt loam; Unified Classification CL; LL = 34, PI = 10, G_s = 2.68) was prepared by

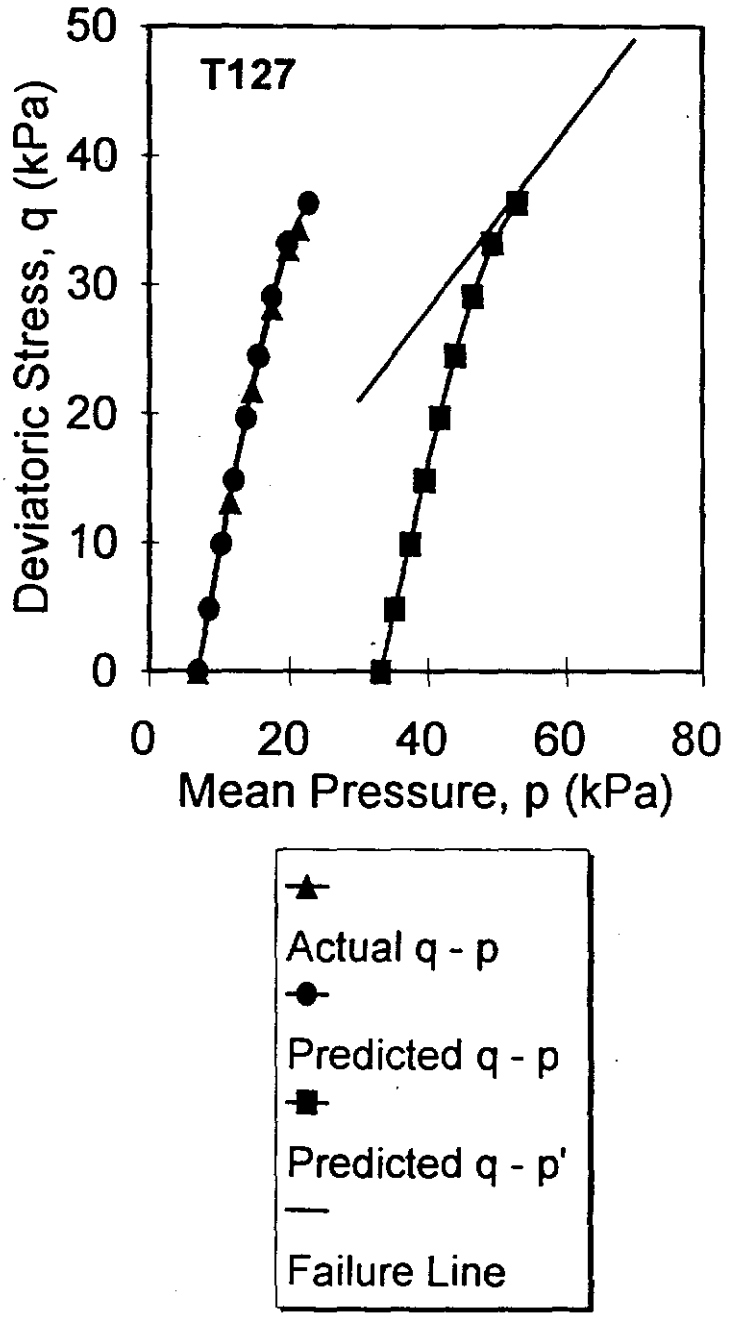

Figure III-2. Actual and predicted stress paths for triaxial test T127.

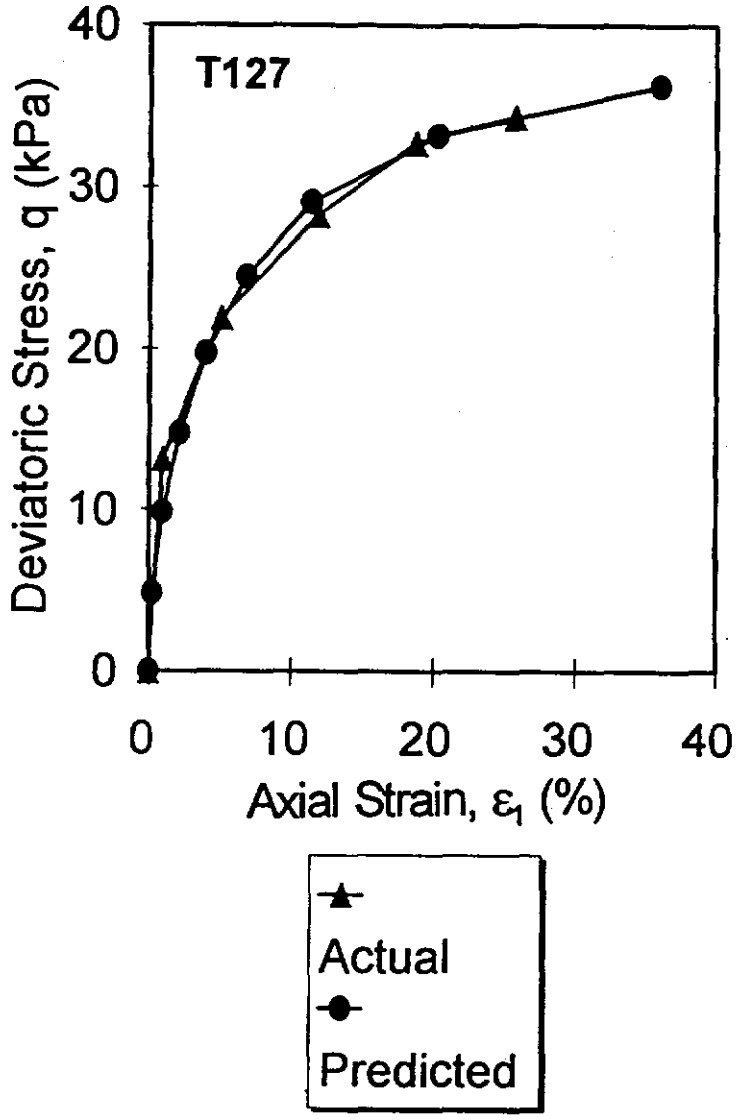

Figure III-3. Actual and predicted deviatoric stress versus axial strain for triaxial test T127.

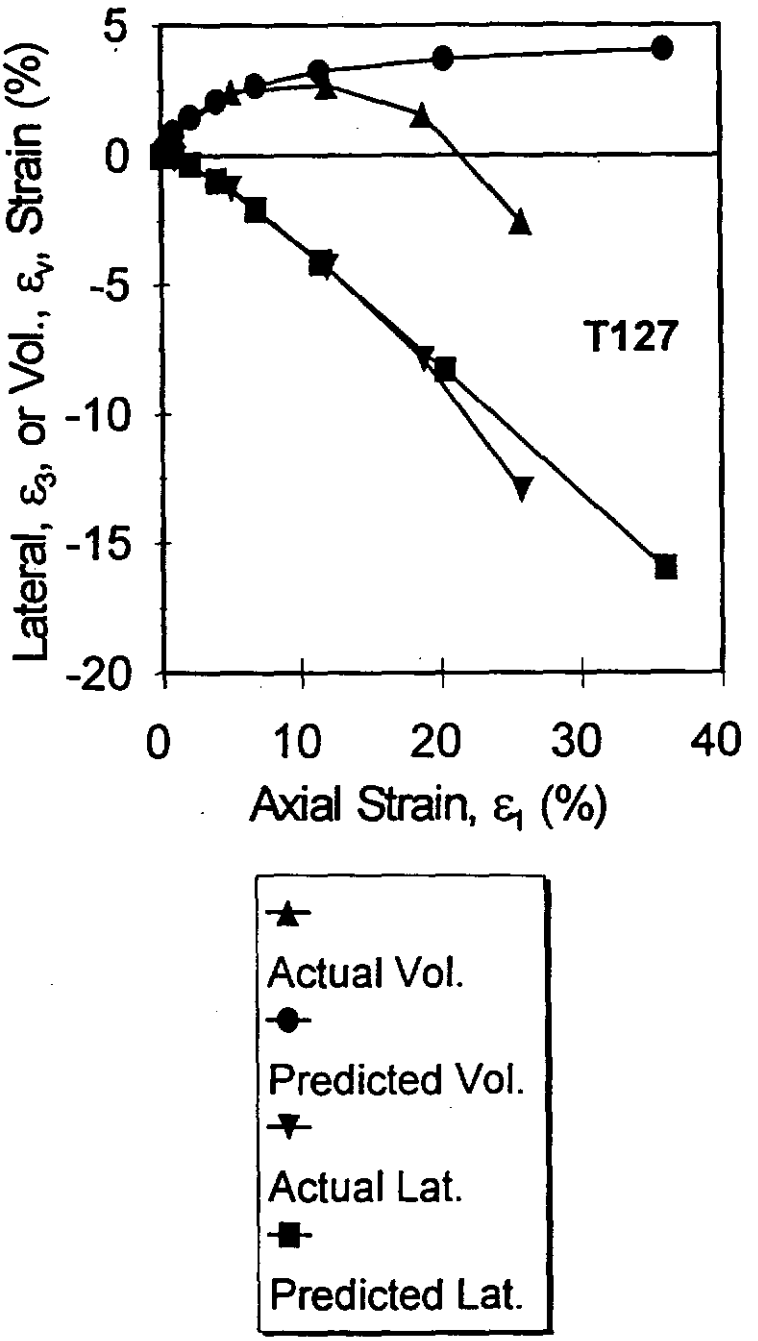

Figure III-4. Actual and predicted lateral and volumetric strain versus axial strain for triaxial test T127.

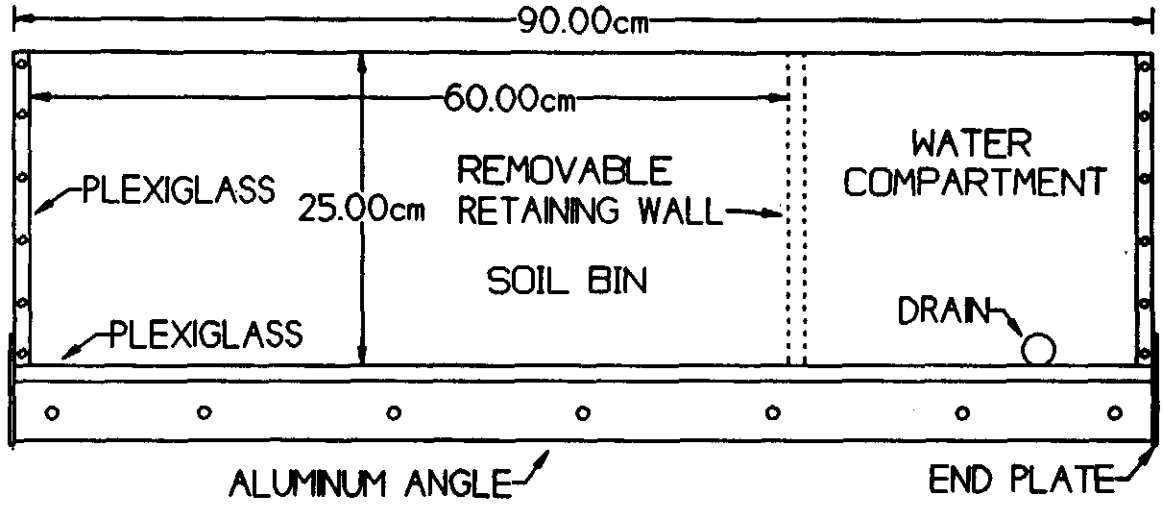

Figure III-5. Soil flume.

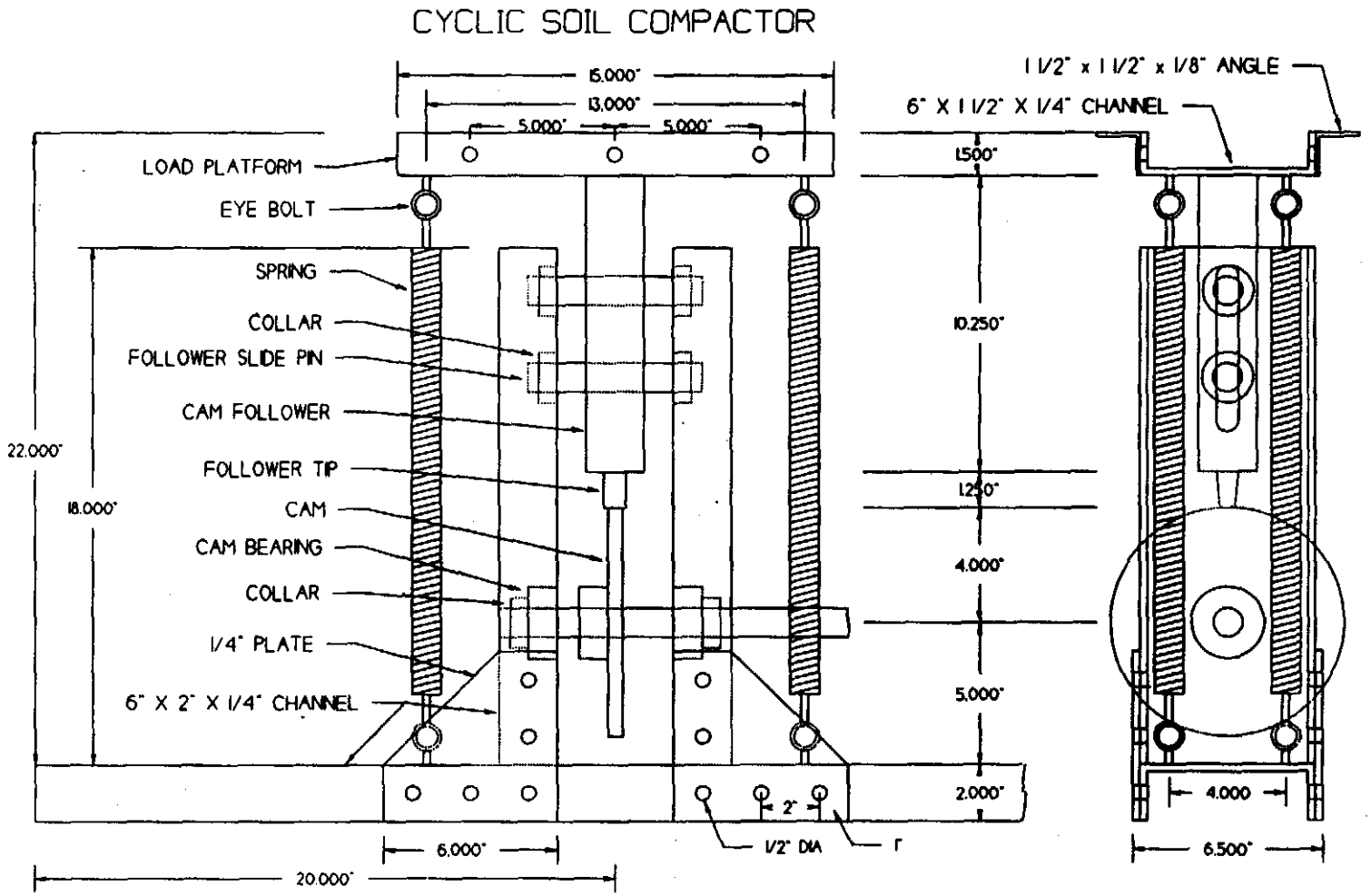

Figure III-6. Cyclic soil compactor.

adding a sufficient amount of tap water to achieve the desired water content. The soil was placed in the flume in layers and compacted as described above. After compaction, the flume was allowed to set overnight. A test run consisted of removing the retaining wall, raising the water level in the water compartment to the desired level, and taking both 35mm and video camera photographs for measurement of displacement and to record the type of failure. If possible, samples for determining soil water content were collected after the channel bank either failed or reached a stable condition.

A total of four flume tests were conducted. These tests were designated as FT-1 ... FT-4 for flume tests 1 through 4.

MODEL PREDICTIONS AND COMPARISON WITH LABORATORY EXPERIMENTS

Development of Model Input Parameters

Model input parameters were obtained (1) directly from soil samples prepared coincident with soil in the flume, (2) through relationships developed from soil testing, or (3) from literature. Average initial bulk density, porosity, volumetric water content, and degree of saturation for each flume test (FT-1 through FT-4) were obtained directly from soil sample tests. The slopes of the normal consolidation and recompression lines were obtained from Eqs. II-69 and II-70. Since the model is insensitive to Young's modulus and Poisson's ratio (Rohlf, 1993), these parameters were obtained from Das (1983).

The saturated hydraulic conductivities for FT-3 and FT-4 were determined by calibrating the model using the advancing wetting front which was visible during these two tests. Parameters for the van Genuchten (1980) water retention relationship (Eqs. II-23 through II-25) used in the hydraulic conductivity calibration were obtained as described below. Results of the calibration comparing the actual wetting front with the model calculated phreatic surface are displayed in Figs. III-7 and III-8 for FT-4 and FT-3, respectively.

Saturated hydraulic conductivities for FT-1 and FT-2 were determined from a relationship with void ratio (Fig. III-9) (Rohlf, 1993).

A summary of soil water retention relationships for FT-1 through FT-4 is presented in Fig. III-10. Note that there is very little difference between the average water retention curves for all four tests. A more detailed presentation of hydraulic conductivity and soil water retention testing is provided by Rohlf (1993).

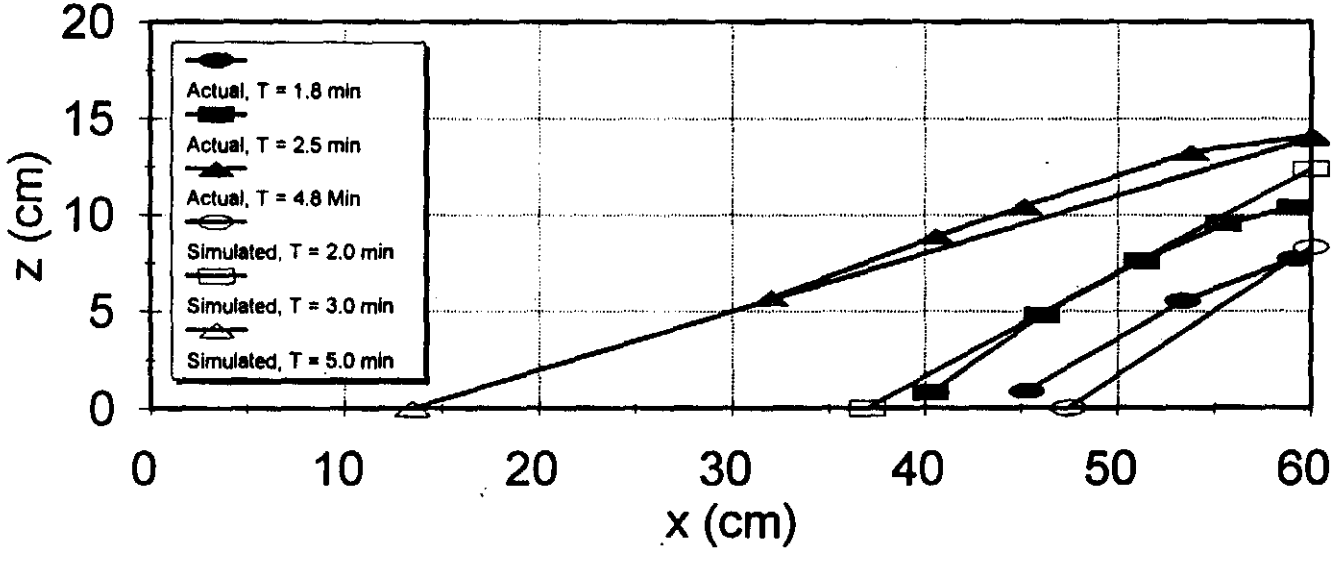

Figure III-7. FT-4 actual and simulated wetting front advance.

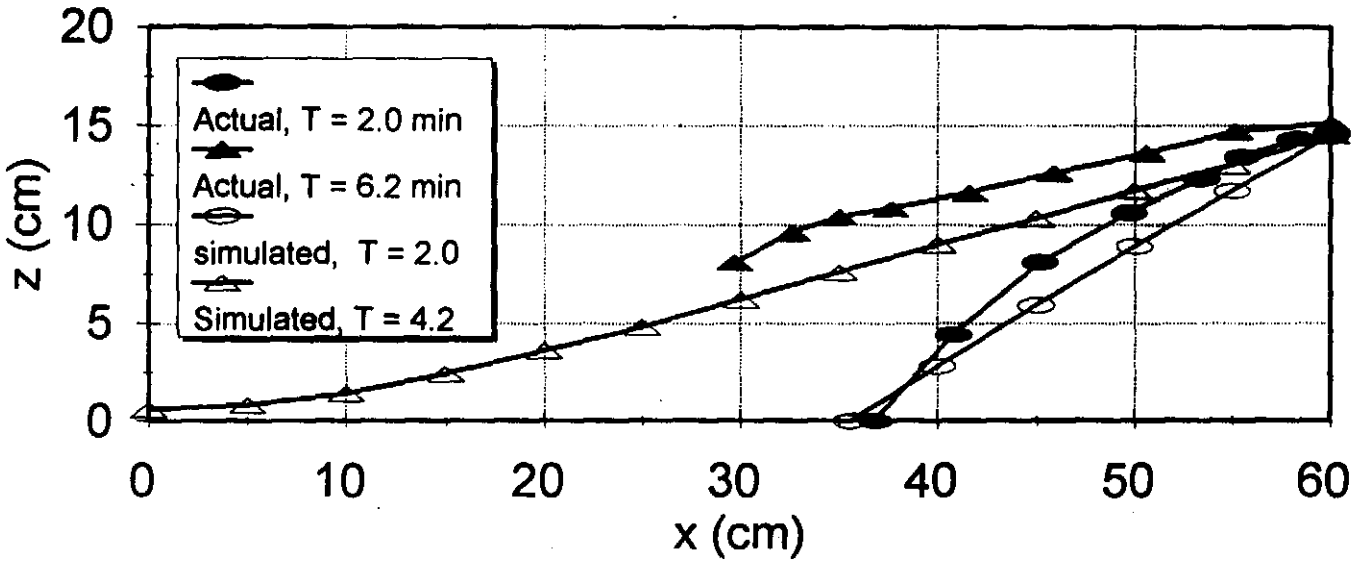

Figure III-8. FT-3 actual and simulated wetting front advance.

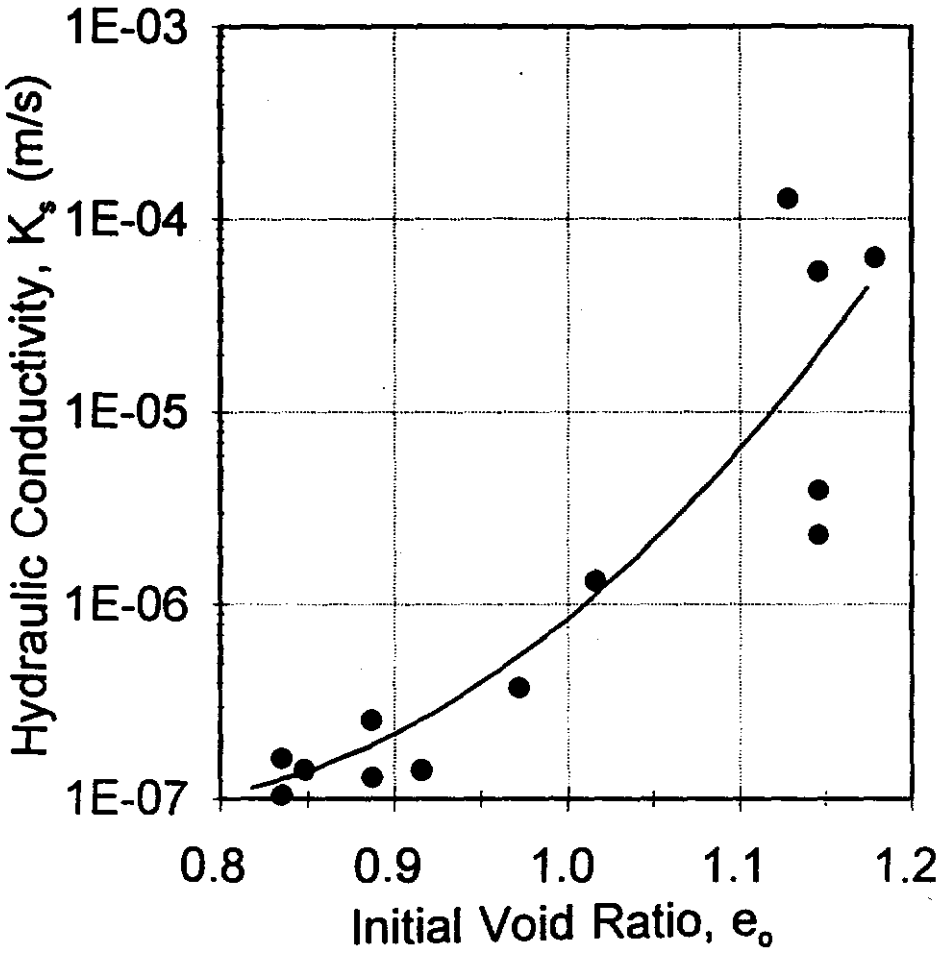

Figure III-9. Saturated hydraulic conductivity versus void ratio.

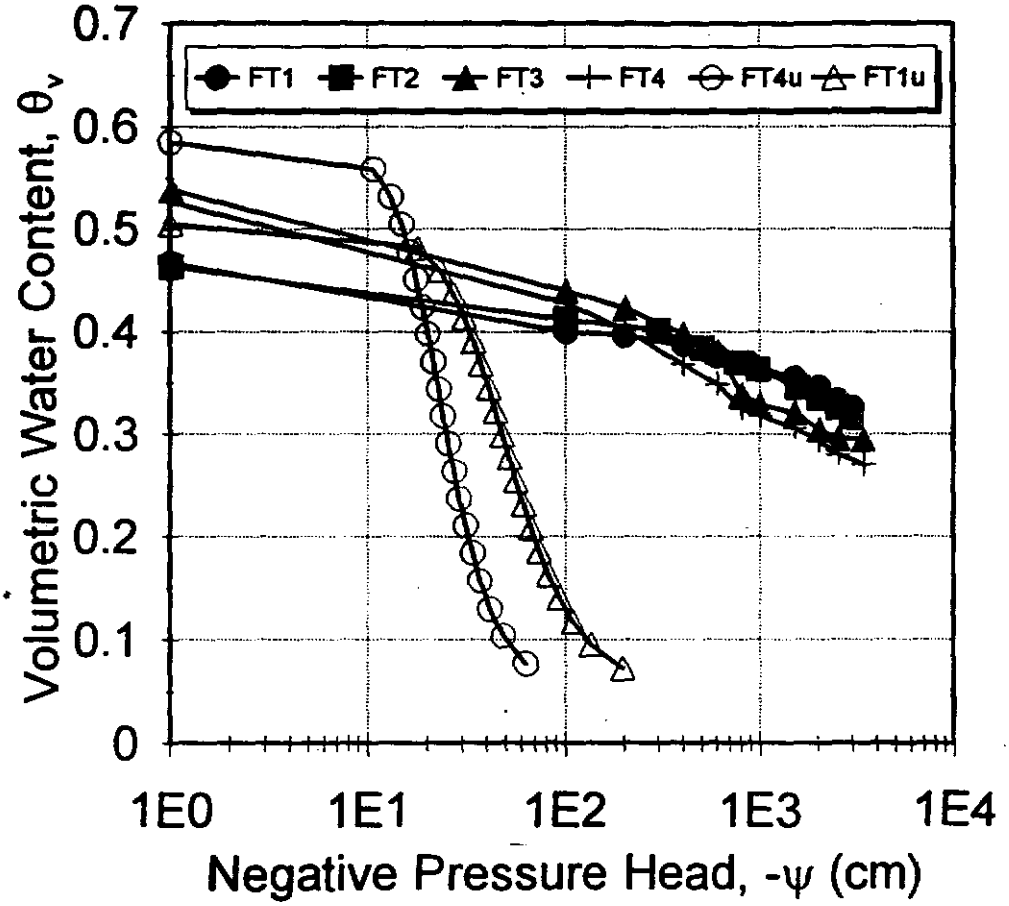

Figure III-10. Summary of soil water retention curves.

All water retention tests were run as conventional desorption tests using a pressure plate (Jury, Gardner, and Gardner, 1991). However, the laboratory experiments generated a rising hydrograph on the channel bank face which produces conditions similar to an adsorption water retention test. Due to hysteresis between the desorption and adsorption limbs of the water retention relationship, the desorption limb demonstrates greater negative pressure heads for a given water content than the adsorption limb (Jury, Gardner, and Gardner, 1991). Consequently, the desorption tests performed were not representative of soil conditions in the flume.

Given the relatively low bulk densities used in these tests and the hysteresis in the water retention relationship, water retention relationships more applicable to a sandy soil rather than a silt loam were used (Bear, 1972). The water retention relationships used in the model are displayed in Fig. III-10 and are designated as FT4u and FT1u. FT4u was used for FT-3 and FT-4 while FT1u was used for FT-1 and FT-2. The relatively small difference between the two retention curves FT1u and FT4u was estimated from the difference between the desorption curves displayed in Fig. III-10 and considering that FT-1 and FT-2 had higher bulk densities than FT-3 and FT-4. A Newton-Raphson iteration technique was used to determine the coefficients for the van Genuchten water retention relationships for FT4u and FT1u.

A summary of all model input parameters for FT-1 through FT-4 is presented in Table III-1.

Model Predictions

Because the time to failure for FT-1 and FT-2 was much longer than FT-3 and FT-4, FT-3 and FT-4 were easier to model. Consequently, the model results will be presented in reverse order of the laboratory tests.

The basic finite element mesh used to simulate FT-1 through FT-4 is displayed in Fig. III-11. Four node rectangular elements were used for all simulations. To accommodate a slight difference in channel bank height, the mesh had 209 elements for FT-4 and 180 elements for FT-1 through FT-3. Element size varied from 2 cm x 2 cm near the channel bank face to 2 cm x 4 cm away from the face.

Model predicted strain is presented for the x-direction since movement in the x-direction should be the best indicator of potential and actual channel bank failure. However, the model also determines z-strain and shear strain, and x, z, y, and shear stress.

Model results are presented in terms of (1) plots of water content contours, (2) plots of strain in the x-direction, and (3) plots of failure at Gauss integration points. Plots of water content show the movement of water into the channel bank. Since soil strength decreases with increasing water content (Eqs. II-62 through II-65), the soil water content distribution is useful in interpreting strain and failure information.

Table III-1

Model Input Parameters

Test	ρ_b (gm/cm^3)	γ_d (kd/cm^3)	n	K_s (cm/min)	θ_v
FT-1	1.326	1.301	.505	$1.2x10^{-4}$	.373
FT-2	1.261	1.237	.530	$1.2x10^{-3}$	.353
FT-3	1.012	.994	.622	10.	.237
FT-4	1.112	1.091	.585	8.	.279
Test	S_r^o	$-\psi$ (cm)	α ($cm^{1/N}$)	N	λ
FT-1	.739	37.2	$1.59x10^{-5}$	2.95	.080
FT-2	.666	42.6	$1.59x10^{-5}$	2.95	.103
FT-3	.381	30.4	$8.91x10^{-6}$	3.78	.280
FT-4	.477	26.6	$8.91x10^{-6}$	3.78	.191
Test	κ	E (kd/cm^2)	ν		
FT-1	.012	$1.x10^5$	.28		
FT-2	.013	$1.x10^5$	.28		
FT-3	.024	$1.x10^5$	.28		
FT-4	.018	$1.x10^5$	.28		

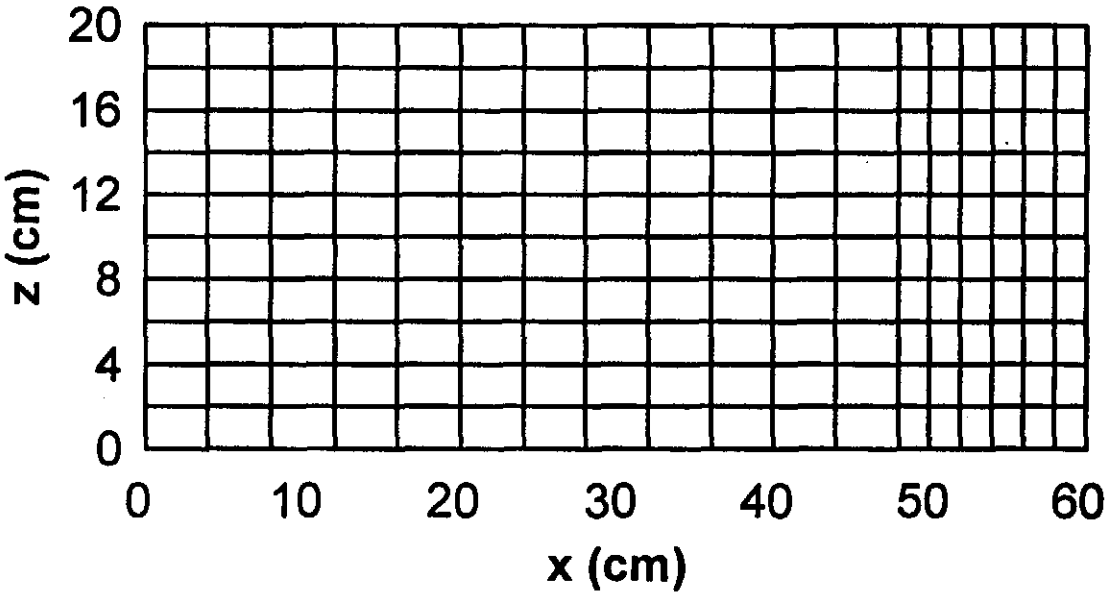

Figure III-11. Finite element mesh.

Contour plots of x-strain show the relative movement of material in the x-direction. Zones or regions with higher x-strain indicate movement in the x-direction and, consequently, the potential development of a failure surface. However, the existence of a zone or region of higher strain does not by itself indicate that failure will occur along a given path. Finite elements which have reached ultimate strength or failure must also be considered in defining failure zones. Elements which have reached ultimate strength can carry no additional load. Depending on the strength and loading condition of the surrounding soil mass, these elements will continue to strain under ultimate load. As additional elements reach ultimate strength, the amount and areal extent of strain increases.

Stress-strain modeling provides more information about the failure process than traditional limit equilibrium analysis, but the results are more difficult to interpret. Limit equilibrium modeling provides a failure surface and a factor of safety (the ratio of resisting to driving forces). However, limit equilibrium analysis uses a fixed failure surface (plane or semicircular), and trial and error must be used to locate the fixed failure surface. Thus, there is no way to be sure that the shape and location of the failure surface represent critical conditions.

Model predictions and comparison with laboratory experiments will now be presented for each test.

Laboratory test FT-4

The rising hydrograph for FT-4 was linear and produced a maximum stage of 14.0 cm in 3.4 minutes. A wetting front was visually observed advancing into the channel bank. Incremental failure which produced undercutting of the face of the channel bank below the water surface (popout failure) began at approximately 5 minutes into the run. A plane failure including material from both above and below the water surface occurred at 46 minutes. The plane failure occurred suddenly without noticeable increase in strain prior to collapse. Predictions of soil water content at 4 minutes of simulation is presented in Fig. III-12. The model predicted that the entire soil mass below the water surface was saturated at the end of 8 minutes of simulation.

Strain in the x-direction after removal of the retention wall (no hydrograph) is presented in Fig. III-13. Strain at 8 minutes of simulation, assuming that there is no reduction in the cohesive intercept, q_c, with increasing water content, is presented in Fig. III-14. Note that there is very little difference between the amount of strain in Fig. III-13 and III-14. Also, the analysis

indicated that there was no failure within any of the elements at 8 minutes of simulation. Since this failure condition did not match the observed, the cohesive intercept was allowed to decrease with degree of saturation as described by Eq. II-62. Reasonable agreement between the observed and predicted failure condition was achieved by decreasing the cohesive intercept to .45 of the original value (q_{cf} = .45, where q_{cf} is the maximum reduction factor for the cohesive intercept, q_c).

Strain predictions in the x-direction at 8 minutes of simulation with q_{cf} = .45 along with the actual plane failure surface is presented in Fig. III-15. A plot of failure at Gauss integration points at 8 minutes of simulation along with the actual failure surface is contained in Fig. III-16.

Comparison of moisture movement (Fig. III-12) with the increase in negative strain (expansion) (Fig. III-15) provides an explanation of the failure mechanism observed in FT-4. The increase in water content produced a reduction in cohesive pressure which resulted in expansion and eventual failure of the material along the channel bank face. The failure along the face of the channel bank appears similar to the alcove or "popout" failure observed by Bradford and Piest (1977).

The strain distribution (Fig. III-15) shows the development of two potential plane failure zones or surfaces, one very near the channel bank face and the other approximately 13 cm back from the face (measured at the top of the bank). The actual failure occurred at approximately 5 cm back from the face.

The plot of failure at Gauss integration points shows the area of "popout" failure below the water surface and tension failure along the top of the channel bank. Tension failure along the top of the channel bank is also due to the increase in water content and a reduction in cohesive pressure. It appears that plane failure occurred as the zone of popout failure extended upward toward the tension failure along the top of the channel bank.

The actual plane failure surface is not clearly indicated by the strain distribution or failure at Gauss integration points. However, the failure did occur within the zone of higher strain near the channel bank face. As noted previously, this failure occurred suddenly without development of an observable strain zone. It is possible that a much smaller finite element mesh would have provided a better indication of the actual failure surface for this type of brittle failure. Note that the failure mechanism for FT-4 differed considerably from that of the Ouse River (Chapter I), which generated large shear strains (50% maximum) prior to failure.

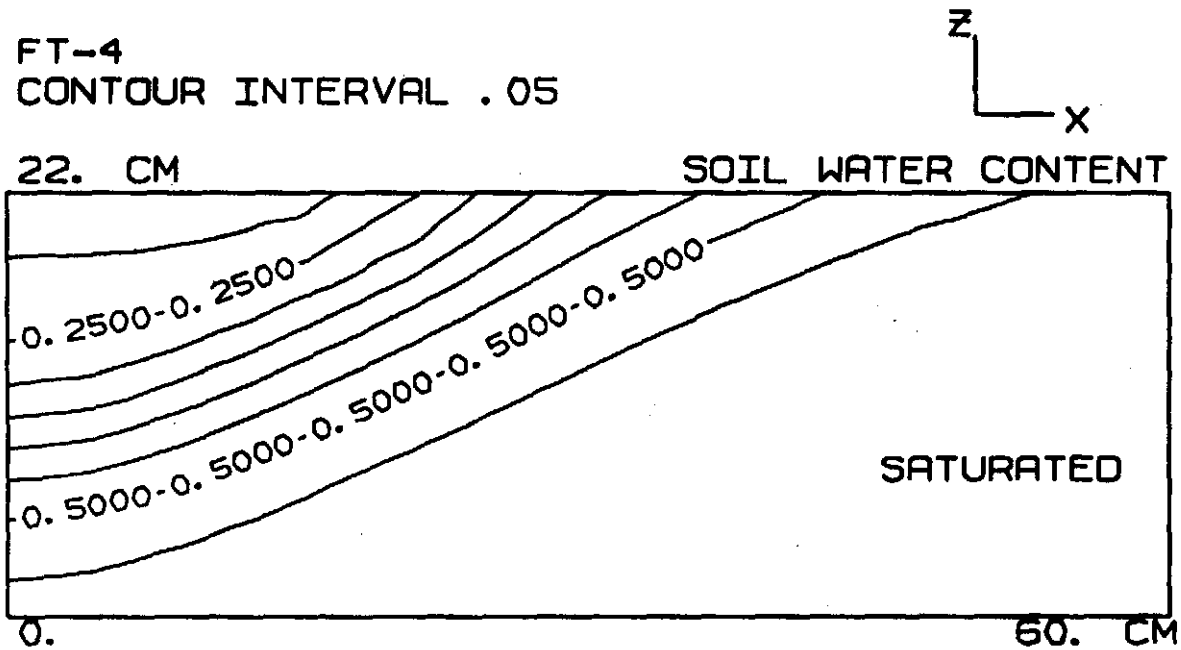

Figure III-12. FT-4 soil water content at 4 minutes of simulation.

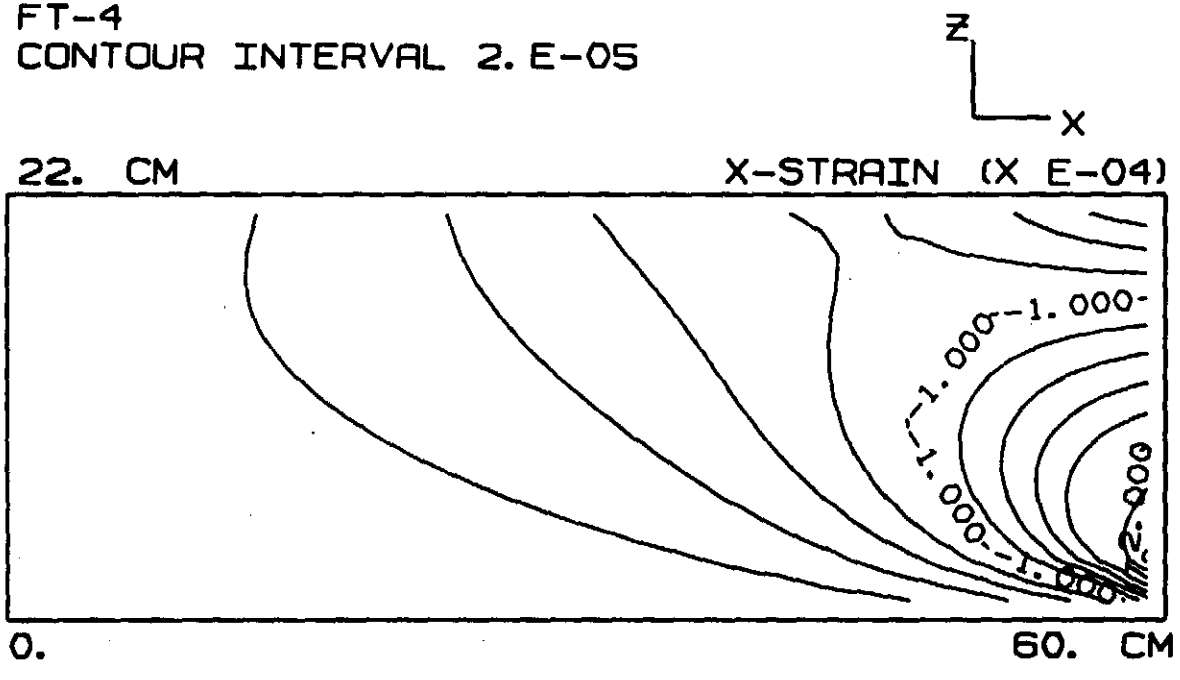

Figure III-13. FT-4 x-strain after removal of retaining wall.

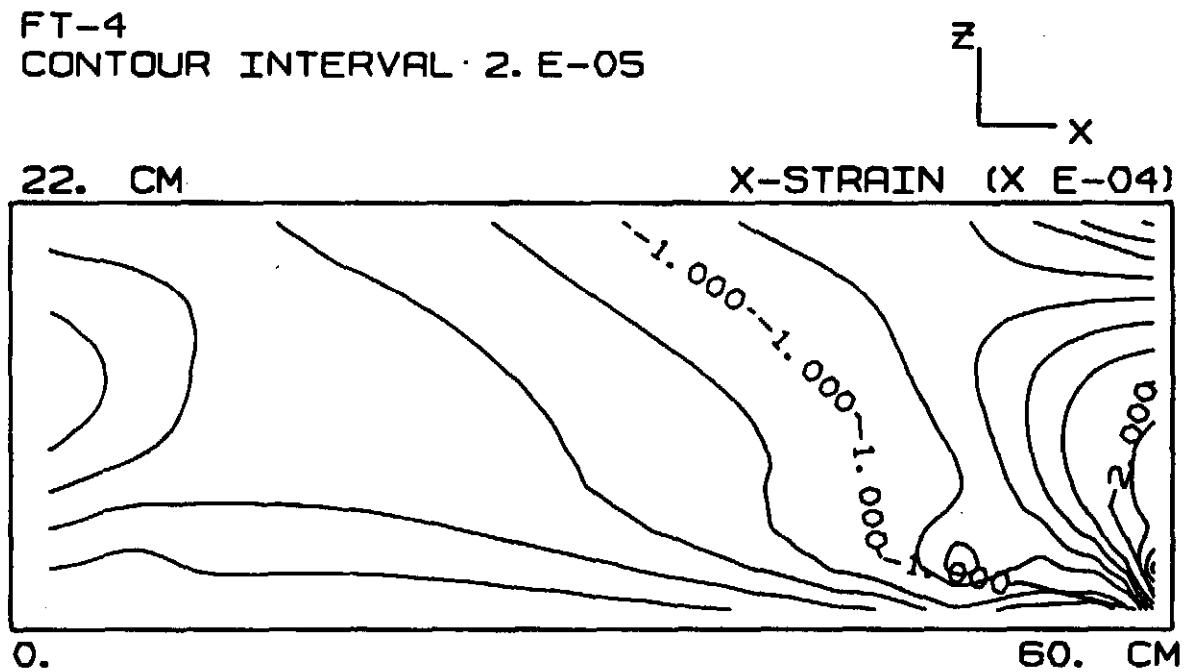

Figure III-14. FT-4 x-strain at 8 minutes of simulation

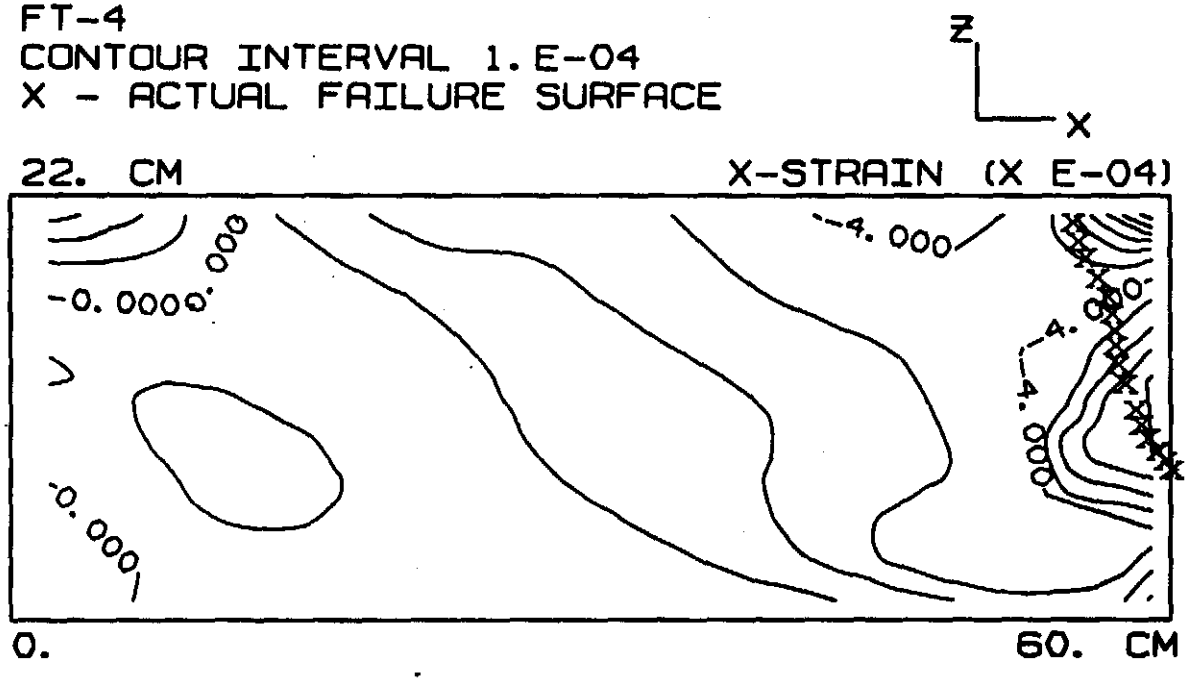

Figure III-15. FT-4 x-strain at 8 minutes of simulation with q_{cf} = .45.

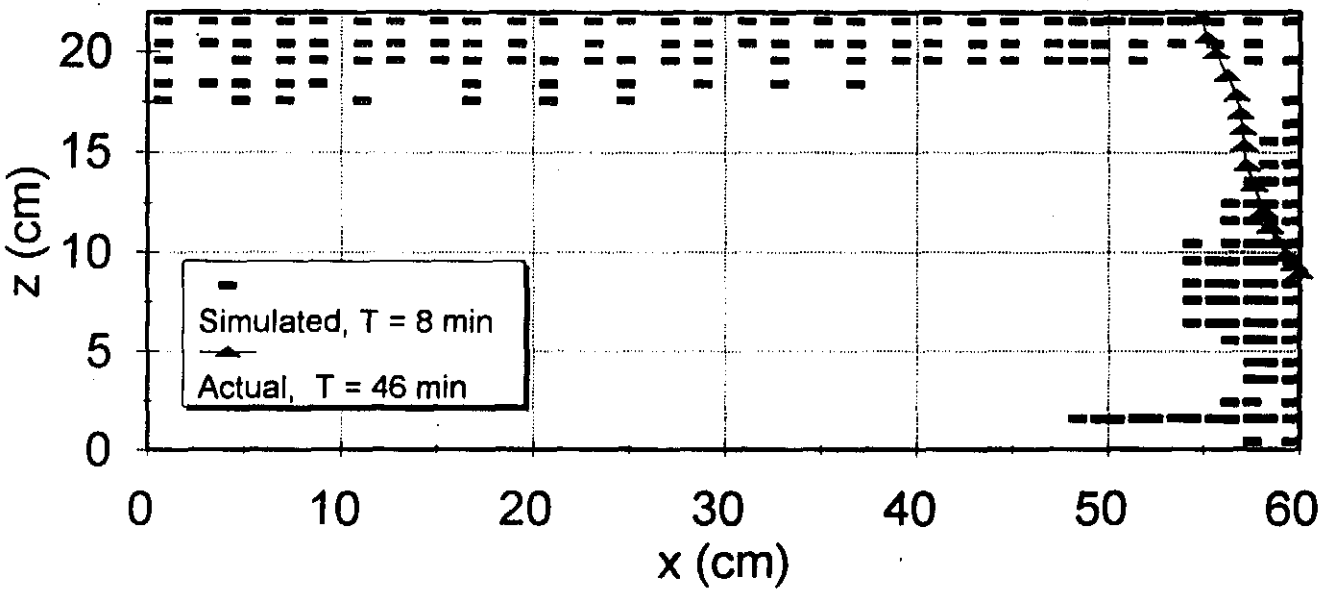

Figure III-16. FT-4 failure at Gauss integration points at 8 minutes of simulation with q_d = .45.

Laboratory test FT-3

The rising hydrograph for FT-3 was linear and produced a maximum stage of 14.5 cm in 1.5 minutes. A wetting front was visually observed advancing into the channel bank. Incremental failure which produced undercutting of the face of the channel bank below the water surface began at approximately 8 minutes into the run. Multiple plane failures including material from both above and below the water surface occurred at 14, 25, and 47 minutes. The popout failure for FT-3 did not develop to the extent of the popout failure for FT-4. This is likely due to the early plane failures which intersected and covered the popout failure zone. As with FT-4, the plane failures occurred suddenly without noticeable increase in strain prior to collapse.

Predictions of soil water content at 4 minutes of simulation is presented in Fig. III-17. The model predicted that the entire soil mass below the water surface was saturated at the end of 6 minutes of simulation.

Strain prediction in the x-direction at 6 minutes of simulation with q_d = .45 is presented in Fig. III-18 along with the actual failure surfaces. A plot of failure at Gauss integration points at 6 minutes of simulation along with the actual failure surfaces is contained in Fig. III-19.

The channel bank failure mechanism for FT-3 appears to be similar to FT-4, although plane failure occurred earlier for FT-3 than for FT-4, and FT-3 produced multiple failures whereas FT-4 had only a single failure. The multiple failures which occurred in FT-3 illustrate the progressive weakening of the channel bank face in response to increasing water content. As with FT-4, the distribution of Gauss failure points shows the popout failure zone extending upward to the tension failure along the top of the channel bank. Also, the strain distribution in Fig. III-18 does not clearly indicate the individual multiple failures but the failures pass through the zone of higher strain near the channel bank face.

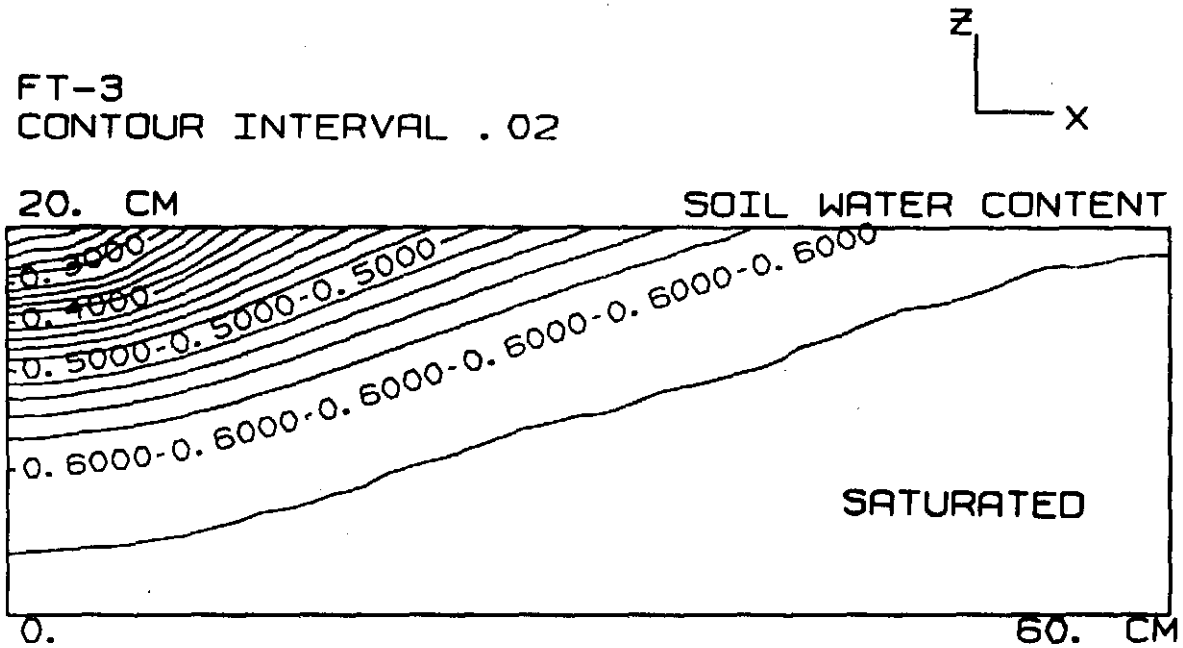

Figure III-17. FT-3 soil water content at 4 minutes of simulation.

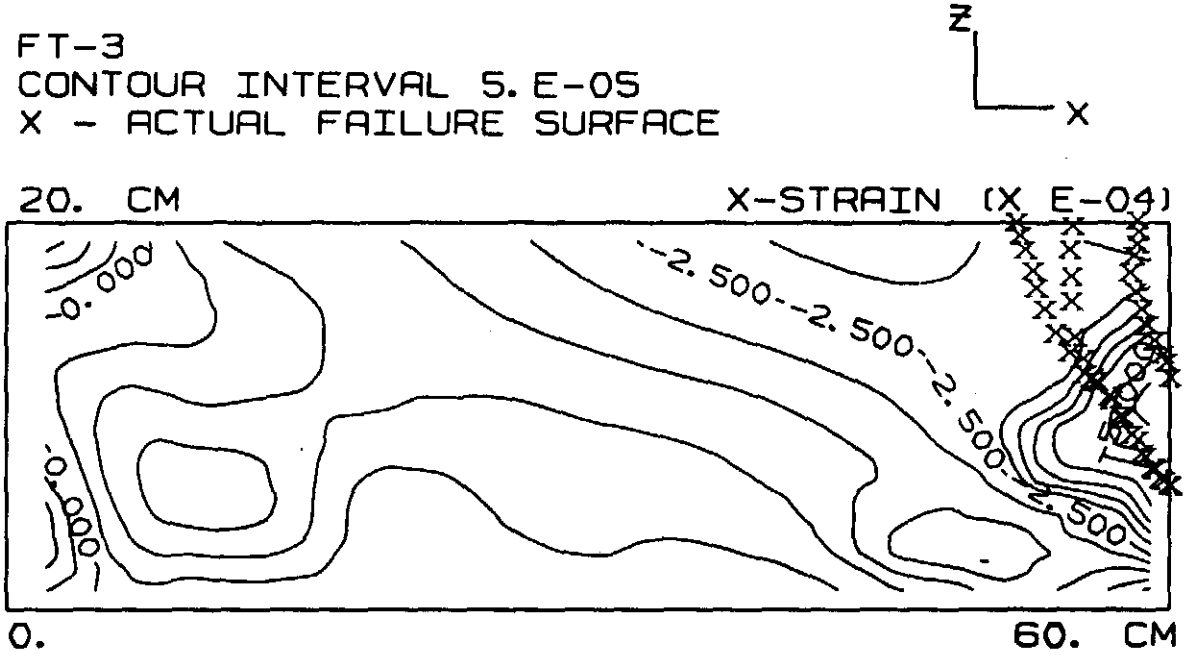

Figure III-18. FT-3 x-strain at 6 minutes of simulation with q_d = .45.

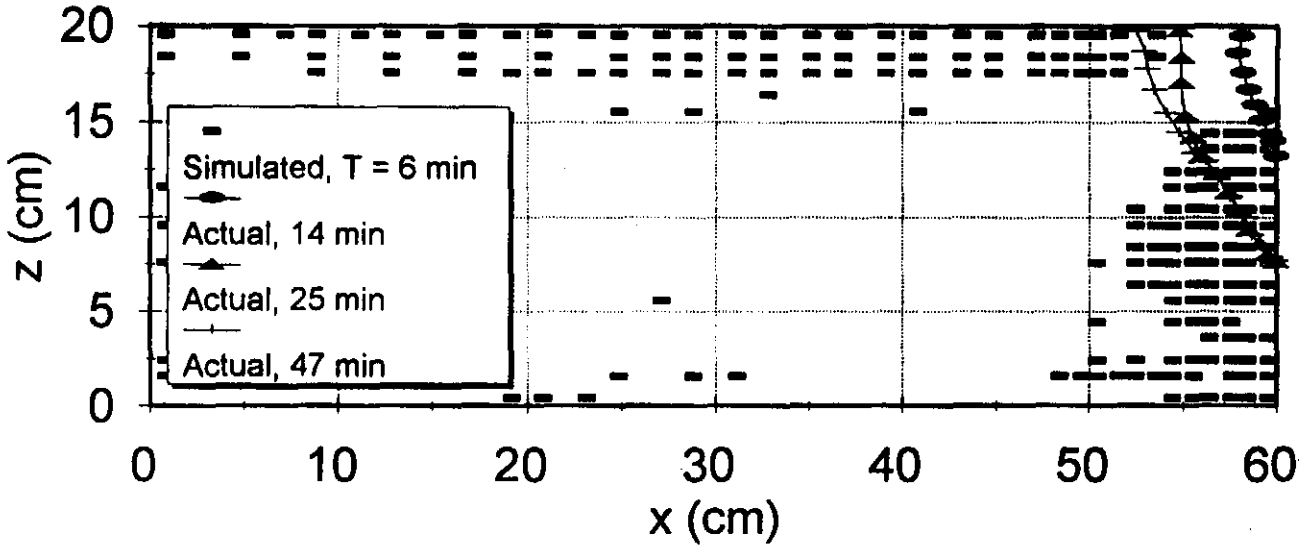

Figure III-19. FT-3 failure at Gauss integration points at 6 minutes of simulation with q_{cr} = .45.

Laboratory test FT-2

The hydrograph for FT-2 is presented in Fig. III-20. The water surface was initially raised to 10 cm and held constant for 385 minutes. The flume was then drained and allowed to remain empty until 1465 minutes when the water surface was increased to 17.8 cm and held constant until 1975 minutes. At 1975 minutes the flume was again drained. Essentially no popout or plane failure of the FT-2 channel bank occurred during the first 385 minute period with the water surface at 10 cm, or during the following period when the flume was drained. After the second increase in water level to 17.8 cm, popout failure occurred at the face of the channel bank below the water level leaving a small semicircular failure surface. Subsequent lowering of the water level at 1975 minutes produced no additional failure.

Predictions of soil water content and strain in the x-direction (q_{cf} = .45) after the second drop in the water surface at 1980 minutes of simulation are presented in Figs. III-21 and III-22, respectively. Again, a zone of negative strain (expansion) developed as the wetting front advanced into the channel bank. A plot of failure at Gauss integration points at 1980 minutes of simulation along with the actual failure surface is presented in Fig. III-23.

The simulated failure zone is larger than the actual failure zone. An examination of slides of the failure showed stress cracks at the bottom of the channel bank indicating that the failure zone may have extended somewhat beyond the area where material was actually removed from the bank. Also, a comparison of simulated and measured water content indicated that the penetration of the wetting front (Fig. III-21) may have been over predicted which would have contributed to an enlarged failure zone.

Strain contours in the x-direction (Fig. III-22) show the development of an elongated zone of high strain. This zone of high strain indicates the development of a potential circular failure surface. However, under water content and soil strength conditions which occurred in FT-2, failure along this surface did not fully develop.

In contrast to FT-4 and FT-3, which failed by formation of a popout with subsequent plane failure of the overhanging ledge, flume test FT-2 produced only a small popout failure. The difference in behavior can be explained by the lower bulk density (Table III-1) and resulting higher shear strength of FT-2 in comparison to FT-4 and FT-3, and the limited penetration of the wetting front.

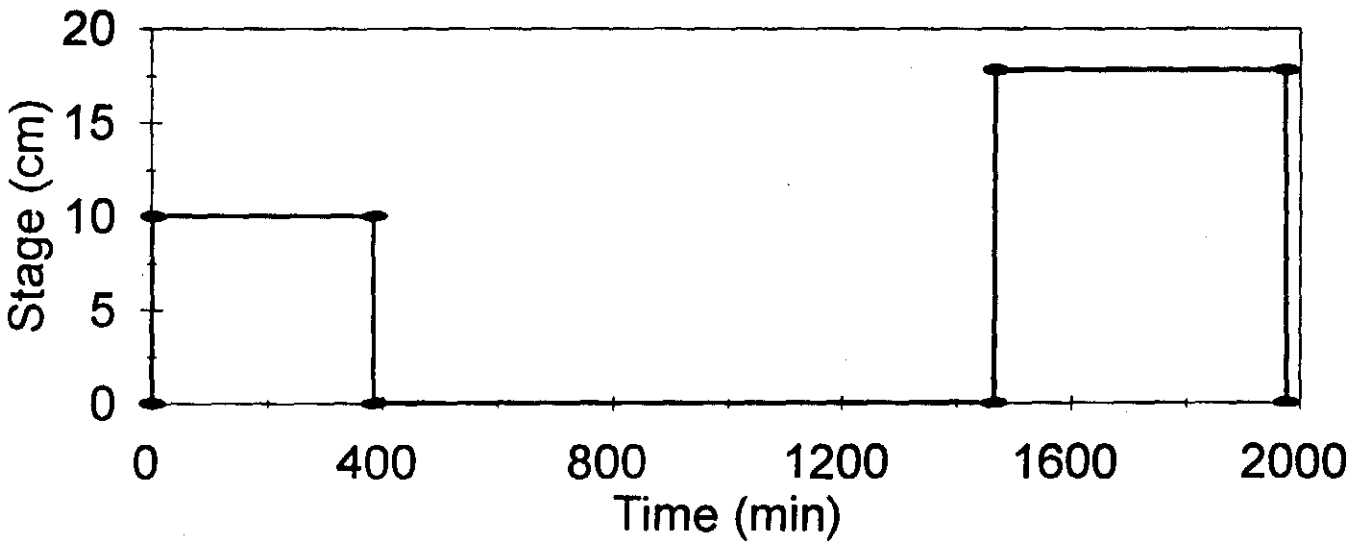

Figure III-20. Hydrograph for FT-2.

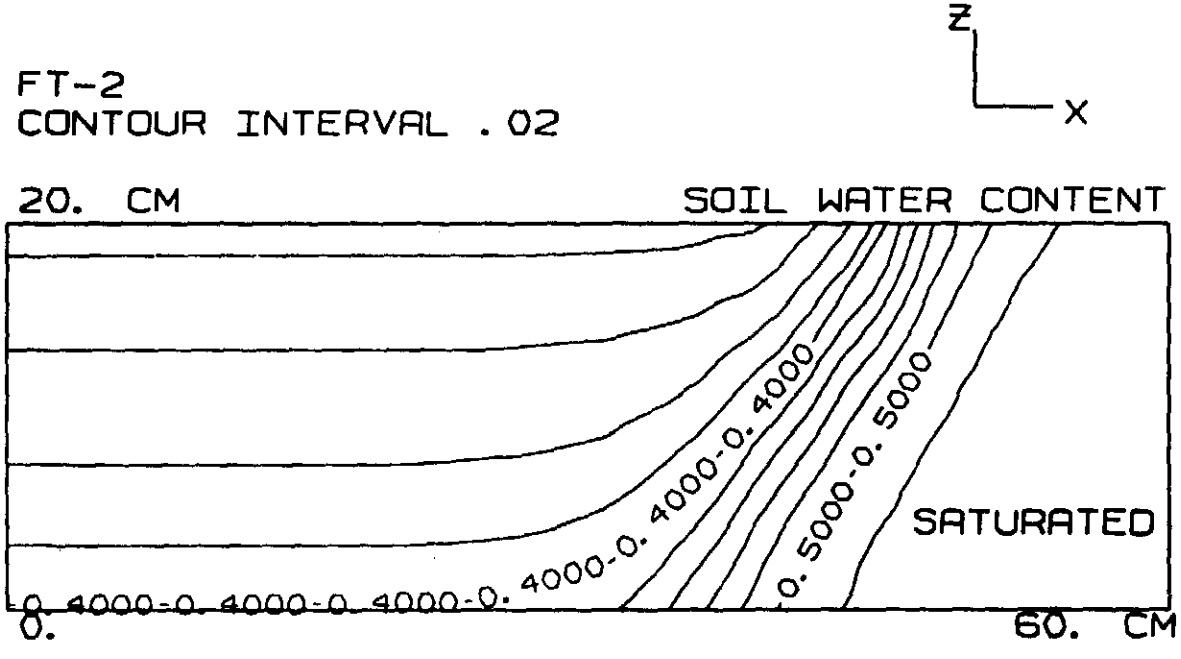

Figure III-21. FT-2 soil water content at 1980 minutes of simulation.

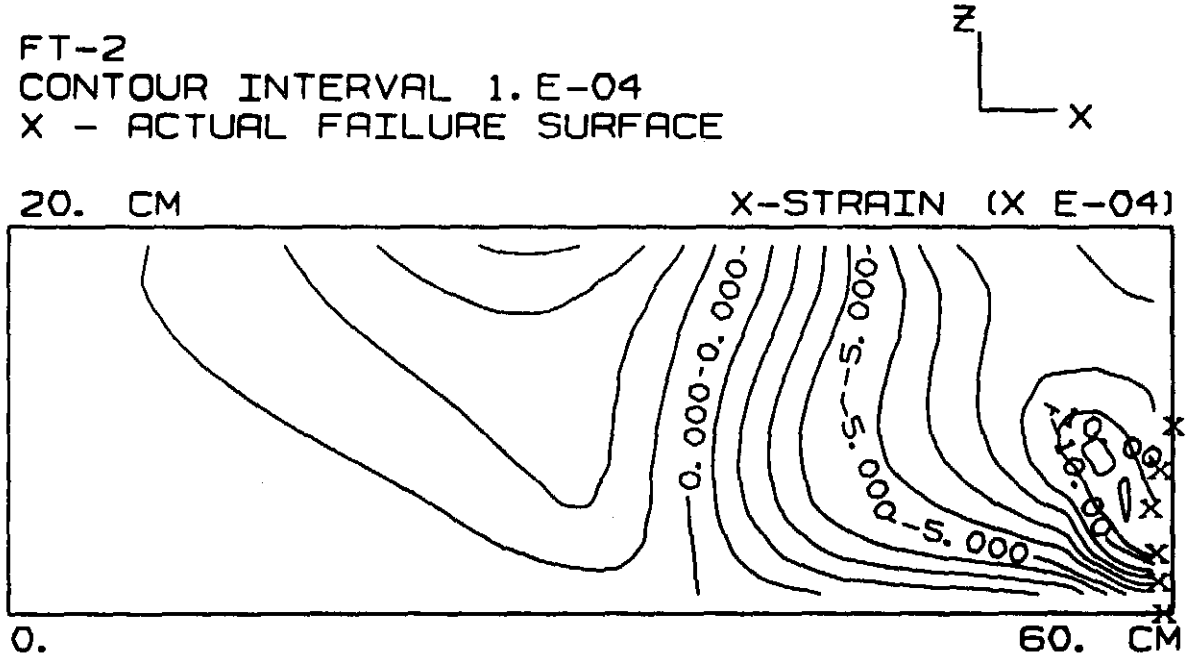

Figure III-22. FT-2 x-strain at 1980 minutes of simulation with q_{cr} = .45.

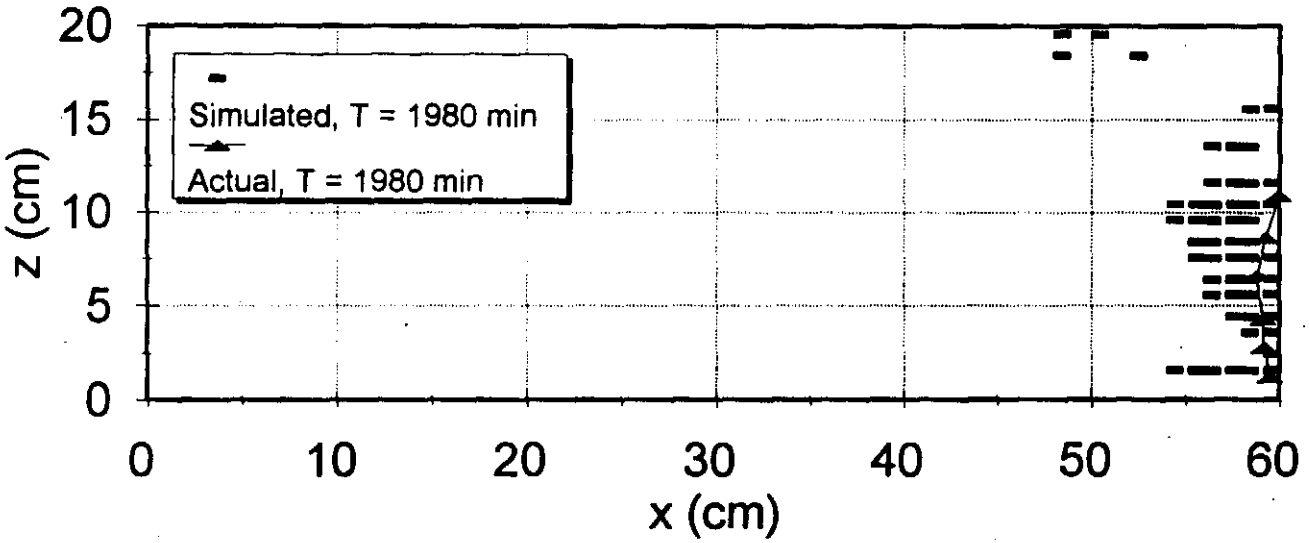

Figure III-23. FT-2 failure at Gauss integration points at 1980 minutes of simulation with q_{cr} = .45.

Laboratory test FT-1

The hydrograph for FT-1 is presented in Fig. III-24. The water level was initially increased to 11.4 cm and held constant for 750 minutes. The water compartment (Fig. III-5) had a small leak during FT-1 and it was necessary to provide a small inflow to maintain a constant water surface. During the night, when the laboratory test was unattended, the water surface increased from 11.4 cm to 23.9 cm at 1365 minutes flooding the soil in the flume to a depth of approximately 3 cm. The water surface was then lowered to 19.0 cm at 1380 minutes and held constant until 1440 minutes. At 1440 minutes, the flume was drained.

Failure of FT-1 consisted of an initial popout failure at the base of the channel bank with a subsequent slab failure which occurred as the flume was drained. The slab failure was approximately 3 to 4 cm wide and initiated at the top of the channel bank. As failure occurred, the slab rotated about a point near the top of the popout failure.

Prediction of soil water content at 1440 minutes of simulation is presented in Fig. III-25.

Strain in the x-direction (q_{cf} = .425) at 1442 minutes of simulation (2 minutes after draining the flume) is presented in Fig. III-26. This figure shows an elongated zone of high strain and development of a slab failure along the face of the channel bank. The elongated zone of high strain can be accounted for by the reduction in water pressure and increase in drag force as the water surface dropped.

A plot of failure at Gauss integration points at 1442 minutes of simulation along with the actual failure surface is presented in Fig. III-27. The agreement between the predicted and actual failure zones is very good.

The failure mechanism observed with FT-1 is similar to the channel bank failure process described by Bradford and Piest (1977) and Piest, Bradford, and Watt (1975) in which a popout or alcove failure near the base of the bank serves as a precursor to slab or plane failure of the overhanging ledge (refer to Fig. I-6). As noted by Bradford and Piest (1977), conventional limit equilibrium methods cannot predict this type of failure mechanism.

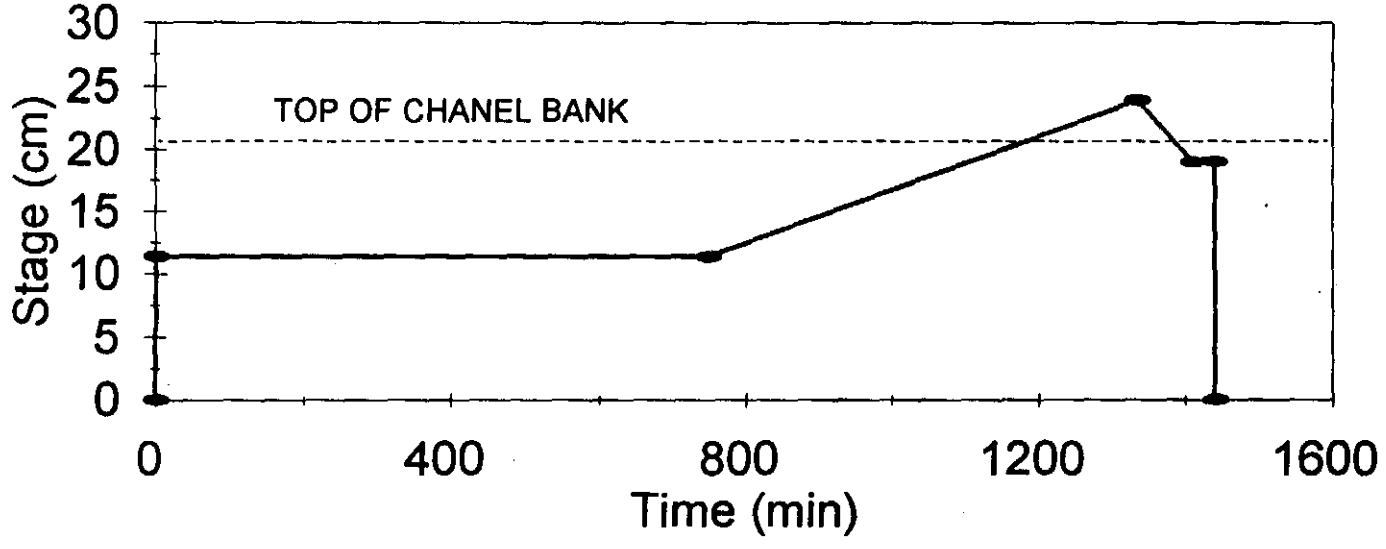

Figure III-24. Hydrograph for FT-1.

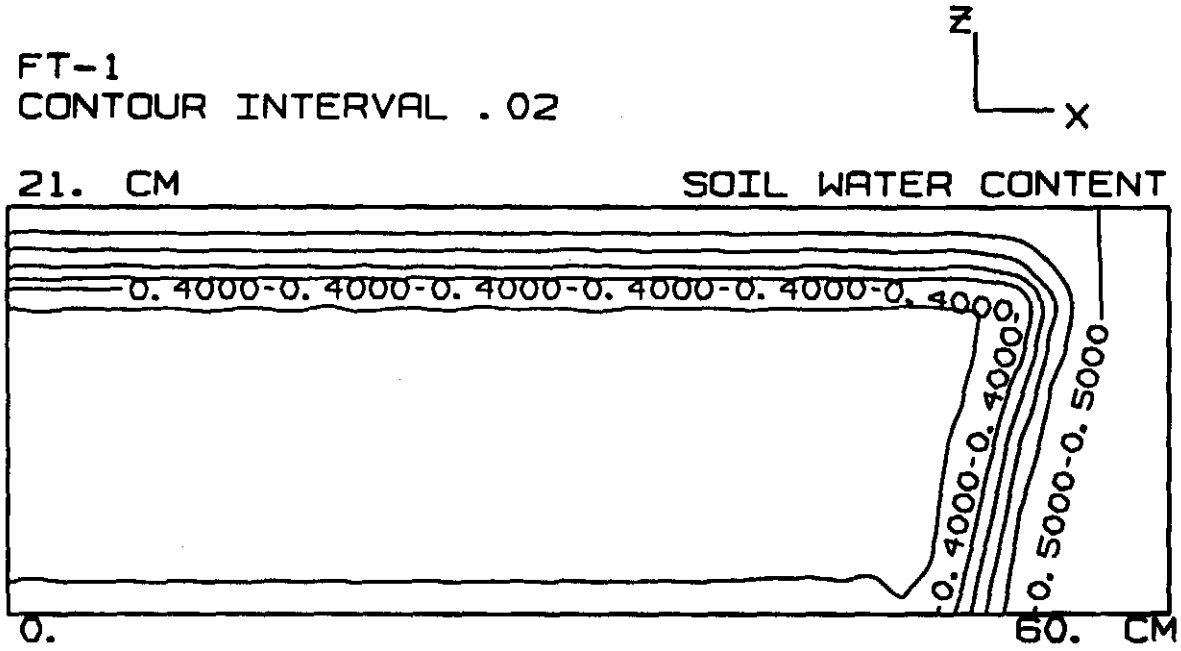

Figure III-25. FT-1 soil water content at 1440 minutes of simulation.

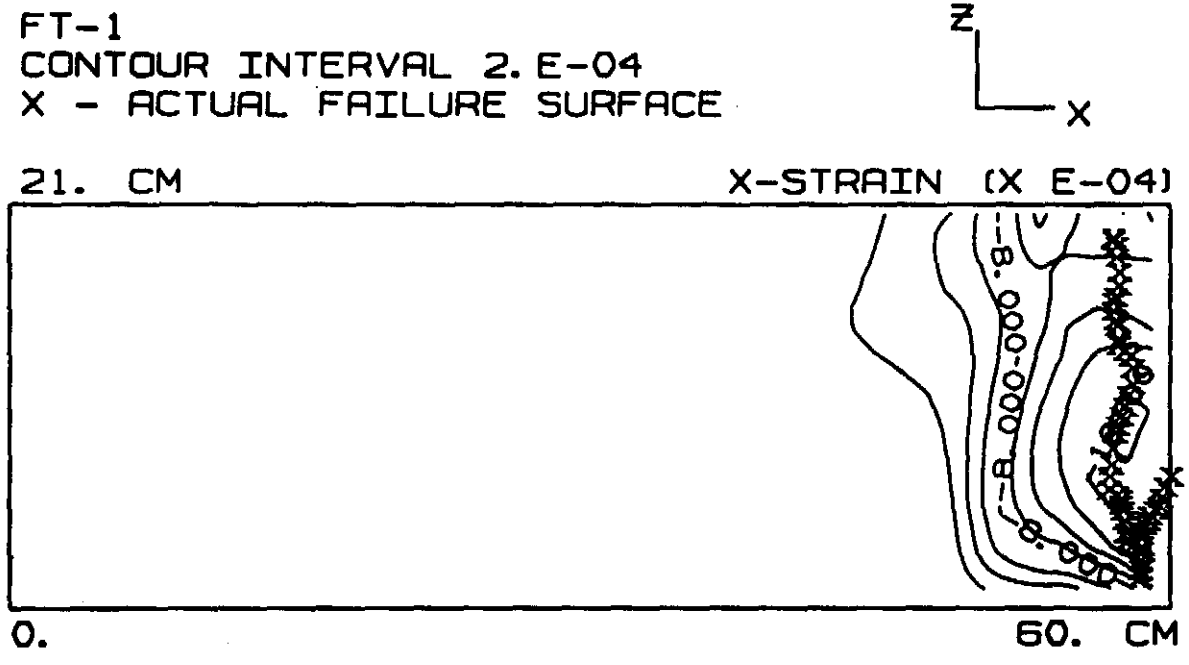

Figure III-26. FT-1 x-strain at 1442 minutes of simulation with q_d = .425.

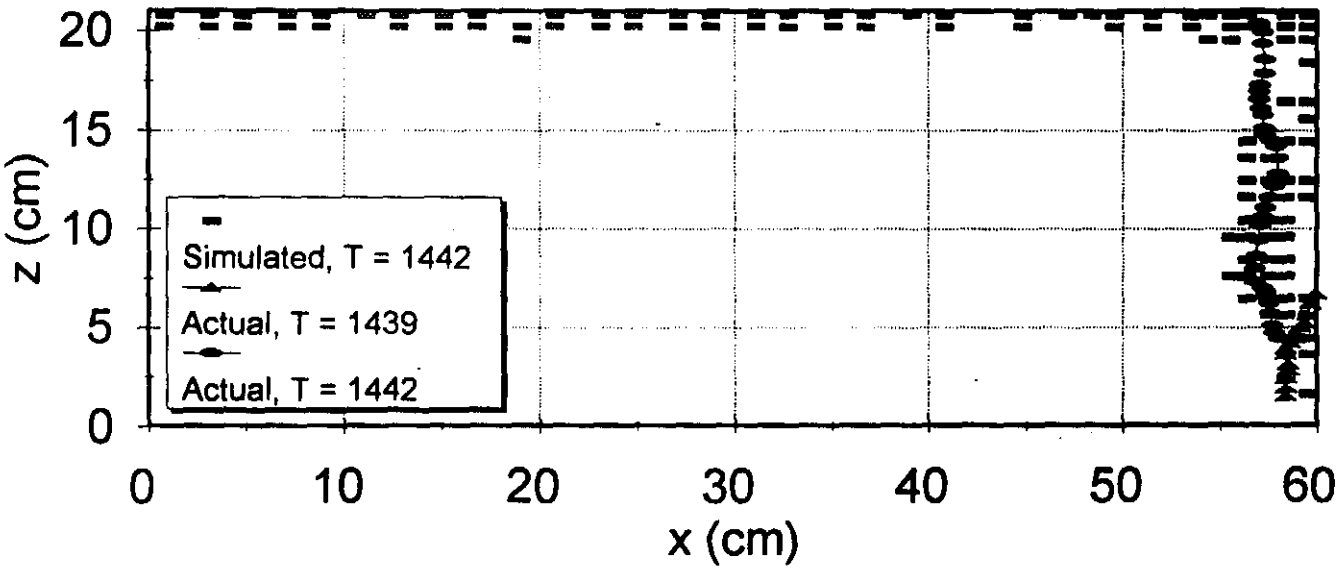

Figure III-27. FT-1 failure at Gauss integration points at 1442 minutes of simulation with q_{cr} = .425.

SUMMARY

The two-dimensional saturated-unsaturated groundwater flow and stress-strain finite element model was verified by comparison with one-dimensional analytic solutions, other numerical solutions for the modified Cam clay yield function, triaxial tests, and laboratory experiments.

Agreement between the analytic and model solutions was excellent and agreement between the model and numerical solutions was very good. The modified Cam clay constitutive relationship over predicted axial and volumetric strain in simulating triaxial tests.

The laboratory experiments included the formation of channel banks approximately 20 cm high and generation of a rising and falling hydrograph on the exposed channel bank face.

Model simulation included groundwater movement into the channel bank, strain in the x-direction, and the location of finite elements which reached ultimate strength. The model provided good insight into the failure mechanism for popout failure and a reasonable prediction of plane failure.

CHAPTER IV

SUMMARY AND CONCLUSIONS

A saturated-unsaturated groundwater flow and elastoplastic stress-strain finite element model was developed for simulating the mechanical behavior of rill and gully sized channel banks. The model coupled the two-dimensional saturated-unsaturated groundwater flow equation with a plane strain formulation of the virtual work equation. The constitutive relationship used the modified Cam clay yield function. The model included the effects of seepage force and variation in soil strength due to changes in water content and void ratio. The groundwater equation was solved first to determine seepage force and soil cohesive force, and then the stress-strain equation was solved. Upon reaching the failure point, the elastoplastic constitutive relationship was replaced with a weak elastic relationship.

The model was verified using (1) one-dimensional analytic solutions for unsaturated flow, saturated flow, and elastic strain; (2) other numerical solutions for the modified Cam clay constitutive relationship; and (3) laboratory experiments. The laboratory experiments employed a specially designed cyclic soil compactor and plexiglass flume to form and compact channel banks. The cyclic soil compactor was also used to prepare soil samples for triaxial testing. The channel banks were subjected to a rising and falling hydrograph.

The following general observations can be made regarding the laboratory experiments and model results:

(1) All laboratory channel bank failures included an initial popout failure located primarily below the water surface. The popout failure occurred under static water conditions without flow generated shear forces.

(2) After formation of a popout, plane failure of the overhanging material occurred without appreciable strain prior to failure for FT-1, FT-3, and FT-4. These failures were basically brittle.

(3) The groundwater flow and stress-strain model provided significant insight into the mechanical behavior of rill and gully sized channel banks. The model was able to predict strain, and the basic failure zone for popout failures. The failure surface for plane failures was well predicted for FT-1, but not well predicted for FT-3 and FT-4.

(4) Popout failures were primarily caused by an increase in soil water content and resulting decrease in soil cohesive strength.

(5) The finite element model included soil cohesion as a basic force similar to body force, fluid drag force, or fluid pressure force. This technique for modeling soil cohesion can be incorporated in any appropriate constitutive relationship, thus eliminating the need to develop special constitutive relationships for soils exhibiting cohesion.

(6) For low bulk density material (FT-3 and FT-4), the predicted time of failure preceded the actual time of failure. This may have been due to over estimating the rate of movement of the wetting front and, thus, due to over estimating the saturated and unsaturated hydraulic conductivities.

(7) Model verification has been conducted only for Maury silt loam and the range in water content under which the soil cohesive pressure relationship was developed. Due to the compaction technique used, the effects of void ratio and soil water content on cohesive force could not be separated.

FUTURE RESEARCH

The model in its present two-dimensional form has the potential to provide insight into a couple of significant channel erosion problems including (1) removal of material from a channel bottom and sides by shear forces; and (2) analysis of channel headwall failure.

A key element in the model is the cohesive pressure relationship. This relationship needs further development and verification. Also, the relationship needs to be extended to other soils to increase the usefulness of the model.

REFERENCES

Bear, J., 1972. Dynamics of Fluids in Porous Media, Dover, New York, NY.

Bishop, A. W., 1955. The Use of the Slip Circle in the Stability Analysis of Slopes, Geotechnique, 5:7-17.

Bishop, A. W., 1967. Progressive Failure - with Special Reference to the Mechanism Causing It, Proceedings of the Geotechnical Conference, Oslo, Norway, pp. 142-150.

Bradford, J. M., Farrell, D. A., and Larson, W. E., 1973. Mathematical Evaluation of Factors Affecting Gully Stability, Soil Sci. Soc. Amer. Proc., 37:103-107.

Bradford, J. H., and Piest, R. F., 1977. Gulley Wall Stability in Loess Derived Alluvium, Soil Science Society of America Journal, 41:115-122.

Bradford, J. M., and Piest, R. F., 1980. Erosional Development of Valley Bottom Gullies in the Upper Midwestern United States, In: Thresholds in Geomorphology, D. R. Coats and J. D. Vitak Eds., pp. 75-101.

Carson, M. A., Kirkby, M. J., 1972. Hillslope Form and Process, Cambridge University Press.

Das, B. M., 1983. Advanced Soil Mechanics, McGraw-Hill Book Co., New York.

Desai, C. S. and Li, G. C., 1983. A Residual Flow Procedure and Application for Free Surface Flow in Porous Media, Advances in Water Resources, 6:27-35.

Desai, C. S. and Siriwardane, H. J., 1984. Constitutive Laws for Engineering Materials with Emphasis on Geologic Materials. Prentice-Hall, Englewood Cliffs, NJ.

Eagleson, P. S., 1970. Dynamic Hydrology. McGraw-Hill, New York, NY.

Fredlund, D. G. and Rahardjo, H., 1993. Soil Mechanics for Unsaturated Soils. John Wiley, New York, NY.

Frydman, S., and Beasley, D. H., 1976., Centrifugal Modelling of River Bank Failure, Journal of the Geotechnical Engineering Division, American Society of Civil Engineers, 102:(GT5): Proc. Paper 12099:395-409.

Hvorslev, M. J., 1937. Uber die Festigkeitseigenschaften Gestorter Bindiger Boden, Kopenhaun.

Jury, W. A., Gardner, W. R., and Gardner, W. H., 1991. Soil Physics, Fifth Edition, John Wiley, New York, NY.

Little, W. C., Thorne, C. R., and Murphey, J. B., 1982, Mass Bank Failure Analysis of Selected Yazoo Basin Streams. Trans. ASAE 25(5):1321-1328.

Lohnes, R. A., and Handy, R. L., 1968. Slope Angles in Friable Loess, Journal of Geology, 76(3):247-258.

Morgenstern, N. R., 1963. Stability Charts for Earth Slopes During Rapid Drawdown, Geotechnique, 12(2):121-131.

Mualem, Y., 1976. A New Model for Predicting the Hydraulic Conductivity of Unsaturated Porous Media. Water Resources Research 12:513-522.

Neuman, S. P., 1973. Saturated-Unsaturated Seepage by Finite Elements, J. of the Hydraulics Division, Proceedings of the American Society of Civil Engineers, 99(HY12):2233-2251.

Owen, D. R. J. and Hinton, E., 1980. Finite Elements in Plasticity: Theory and Practice. Pineridge Press, Swansea, UK.

Phillip, J. R., 1957. Evaporation, and Moisture and Heat Fields in the Soil, J. Meteorol., 14(4): 354-366.

Piest, R. F., Bradford, J. M., and Wyatt, G. M., 1975. Soil Erosion and Sediment Transport from Gullies, J. of Hydraulics Div., ASCE, 101(HY1):65-80.

Ponce, V. M., 1978. Generalized Stability Analysis of Channel Banks, Journal of the Irrigation and Drainage Division, American Society of Civil Engineers, 104(IR4):Proc. Paper 14228:343-350.

Rohlf, R. A., 1993. Groundwater Flow and Elastoplastic Stress-Strain Modeling of Channel Bank Failure, Ph. D. dissertation, Dept. of Civil Engineering, Univ. of Kentucky, Lexington, KY.

Romkens, M. J. M., Phillips, R. E., Selim, J. M., and Whisler, F. D., 1985. Physical Characteristics of Soils in the Southern Region - Vicksburg, Memphis, Maury Series, Southern Cooperative Series Bulletin No. 266.

Roscoe, K. H. and Burland, J. H. 1968. On the Generalized Stress-Strain Behavior of 'Wet' Clay, in Engineering Plasticity, J. Heyman and F. A. Leckie Eds., Cambridge University Press, Cambridge, UK, pp. 535-609.

Satija, B. S., 1978. Shear Behavior of Partially Saturated Soils, Ph. D. dissertation, Indian Inst. of Technol., Delhi.

Schofield, A. N., and Wroth, C. P., 1968. Critical State Soil Mechanics. McGraw-Hill Book Company, London.

Shuttle, D. A. and Smith, I. M., 1988. Numerical Simulation of Shear Band Formation in Soils, International Journal for Numerical and Analytical Methods in Geomechanics, 12:611-626.

Siriwardane, H. J. and Desai, C. S., 1983. Computational Procedures for Non-Linear Three-Dimensional Analysis with Some Advanced Constitutive Laws, International J. for Numerical and Analytical Methods in Geomechanics, 7:143-171.

Skempton, A. W., 1964. The Longterm Stability of Clay Slopes (The Rankine Lecture), Geotechnique, 14:90-108.

Stasa, F. L. 1985. Applied Finite Element Analysis for Engineers. Holt, Rinehart and Winston, New York, NY.

Taylor, D. W., 1948. Fundamentals of Soil Mechanics, John Wiley and Sons, New York.

Terzaghi, K., 1943. Theoretical Soil Mechanics, John Wiley and Sons, New York.

Thorne, C. R., 1978. Processes of Bank Erosion in River Channels, Thesis submitted in complete fulfillment of the requirements of the degree of Doctor of Philosophy, University of East Anglia, Norwich, UK.

Thorne, C. R., 1982. Processes and Mechanisms of River Bank Erosion, In: Proc. of the International Workshop on Engineering Problems in the Management of Gravel-Bed Rivers, Greyynog, Wales, June 23-28, 1980, John Wiley and Sons, London, England.

Thorne, C. R., and Lewin, J., 1979. Bank Processes, Bed Material Movement and Planform Development in a Meandering River, In: Adjustments of the Fluvial System (D. D. Rhodes and G. P. Williams, Eds.), Kendall/Hunt Publishing Co., Dubuque, Iowa, pp. 117-137.

Thorne, C. R., Little, W. C., and Murphey, J. B., 1981. Bank Stability and Bank Material Properties in the Bluff Line Streams of Northwest Mississippi, Report to the U.S. Army Corps of Engineers, Vicksburg District Office, USDA-SEA Sedimentation Laboratory, Oxford, Miss.

Thorne, C. R. and Tovey, N. K., 1981, Stability of Composite River Banks, Earth Surface Processes and Landforms, 6:469-484.

Turnbull, W. J., Krinitizsky, M., and Weaver, F. J., 1966. Bank Erosion in Soils of the Lower Mississippi Valley, Journal of the Soil Mechanics and Engineering Division, American Society of Civil Engineers, 92:121-136.

Van Genuchten, M. T. 1980. A Closed Form Equation for Predicting the Hydraulic Conductivity of Unsaturated Soils. Soil Soc. Sci. Am. J., 44:892-898.

Zienkiewicz, O. C., Chang, C. T. and Bettess, P., 1980. Drained, Undrained, Consolidating and Dynamic Behavior Assumptions in Soils, Limits of Validity, Geotechnique, 30: 385-395.

Zienkiewicz, O. C. and Shiomi, T., 1984. Dynamic Behavior of Saturated Porous Media; the Generalized Boit Formulation and its Numerical Solution." Int. J. Numer. Anal. Methods Geomech., 8:71-96.

Zienkiewicz, O. C. and Taylor, R. L., 1989. The Finite Element Method. Fourth Edition, Volume 1, Basic Formulation and Linear Problems, McGraw-Hill, New York, NY.

Zienkiewicz, O. C. and Taylor, R. L., 1991. The Finite Element Method, Fourth edition, Volume 2, Solid and Fluid Mechanics Dynamics and Non-Linearity, McGraw-Hill, New York, NY.